Department of Chemistry

University College London

University of London

Surface Science of Ultrathin Metal Oxide Films

Jai Matharu

I, Jai Matharu confirm that the work presented in this thesis is my own. Where information has been derived from other sources, I confirm that this has been indicated in the thesis.

<div align="right">

....

Jai Matharu

November 27, 2011

</div>

Abstract

The properties of metal oxide surfaces are key to their diverse technological applications. However, the semiconducting nature of metal oxides presents a problem - many surface science techniques are electron based and thus require samples to be conducting. As such, bulk crystal studies of metal oxides by techniques such as photoemission spectroscopy (PES) and scanning tunneling microscopy (STM) are limited to reduced surfaces. Alternatively, thin films of a metal oxide can be synthesised on a suitable conducting substrate that mimic the bulk crystal surface whilst having sufficient conducting character to use these techniques. CeO_2 is an important material found in three-way catalysts that remove pollutants from the exhaust gas of modern automobiles. Key to this application is the ability of reduced ceria to store and release oxygen depending on the composition of the exhaust. The addition of noble metals such as Pd to the ceria surface greatly improves the efficiency of pollutant conversion evidenced by X-ray photoelectron spectroscopy (XPS) by reducing the ceria. Resonance photoemission spectroscopy (RESPES) has been used to investigate the effect of Pd on ceria $CeO_{2-x}(110)$ thin films grown on a Pt(111) substrate. RESPES is more surface specific than XPS and thus reveals more information on the surface layers of ceria films. $TiO_2(110)$ is the most studied metal oxide surface, and has a multitude of applications. Its chemistry with two of the most abundant chemical species - water (H_2O) and oxygen (O_2) - is thus very important. H_2O has been shown to dissociate on TiO_2 surfaces. TiO_2 thin films grown on W(100) were used as model system to study the chemistry of the reaction between TiO_2 and H_2O, and subsequently the reaction of hydrated surfaces with O_2 using XPS. STM was used to examine the morphology of $TiO_2(110)$ films grown on W(100)-(2×1)-O, changes with film thickness and methods of improving surface smoothness. The first detailed STM images showing row structure of $TiO_2(110)$ films grown on W are shown.

Acknowledgements

Firstly, I would like to thank my supervisor Geoff Thornton for offering me the chance to work in his research group and for his supervision and guidance.

I would also like to thank the Thornton group post-docs past - Greg Cabailh for his guidance and help with XPS analysis, not to mention reading countless drafts of papers and thesis chapters; Qiao Chen for teaching me about instrumentation and how to approach surface science problems; and Chi Pang.

Thanks also to all my fellow students past and present, in particular David Humphrey for his help with instrument maintenance and general chats; Oliver Yim for taking the time to help me getting to grips with STM operation and for discussion on TiO_2; David Grinter for discussion on CeO_2; and Tom Woolcot for his help with the STM.

Thanks also to other scientists who assisted me - Rob Lindsay; Tomas Skála at MSB, ELETTRA; John Purton at Daresbury Light Source; and Chris Muryn.

Thanks to UCL admin staff, particularly my secondary supervisor Wendy Brown, for her support as Graduate tutor. Also to Mary-Lou Jabore for her help when I broke my leg.

Thanks to the technicians who fixed various instruments for me - Len Parrish for his electrical wizardry and patience, maintaining good humour despite the near constant stream of broken power supply units; Crosby Medley, John Hill, Dave Knapp, Nick Palmer at PSP Vacuum, Jon Whitehead at Moorfield, Nick Hodge at SIP Analytical.

Thanks to the EPSRC for funding me, and to the UCL Graduate School and UCL Chemistry for additional money.

A huge thank you to all my friends, flatmates and family for their support and friendship. Thanks to my Mum for her love and support.

Lastly and most importantly, thank you to Helen for her love and patience, even when I was at my most fractious...

List of publications

- Matharu, J., Cabailh, G., Lindsay, R., Pang, C.L., Grinter, D.C., Skála, T., Thornton, G.; *Reduction of thin-film ceria on Pt(111) by supported Pd nanoparticles probed with resonant photoemission, Surf. Sci.*, **2011**, *605*, 1062

- Matharu, J., Cabailh, G., Thornton, G.; *Synthesis and Reactivity of ultrathin film TiO_2 grown on W(100)*, In submission.

Contents

List of Figures

List of Tables

Chapter 1

Introduction

1.1 Metal oxides

Metal oxides comprise a class of diverse and fascinating materials. Their importance to technology is huge, with a wide variety of applications. They cover the entire conductivity range (10^{-18}-10^8 S cm^{-2}) encompassing metals, semiconductors and insulators.

A major use of metal oxides is in catalysis. Most commercial catalysts consist of metal deposits on a high surface area metal oxide support. When the oxide support is non-reducible, metals are generally not modified with the presence of the support except for the influence on particle size. However, in some cases metal/support interaction or the existence of complementary reactions taking place on the metal or oxide may influence catalytic properties. Metals supported by reducible oxides can experience strong interactions that alter catalytic behaviour. In some cases, the metal oxides themselves can catalyse reactions, either in pure (for example, bismuth molybdate in acrylonitrile synthesis) or mixed forms (for example, V_2O_5 on TiO_2 in the selective oxidation of hydrocarbons and selective catalytic reduction of NO_x).

Metal oxide catalyst supports can play an active role in catalysis by storing and releasing oxygen [1], capturing adsorbates [2, 3], exchanging charge with an active component [4, 5] or by maintaining a high dispersion of metallic deposits [6, 7].

Metal oxides are also important as gas sensors, particularly ZnO and SnO_2. This application relies on the nature of electrical resistivity. Stoichiometric metal oxides can have very high bulk electrical resistivity, although after doping or due to the presence of defects they can behave as n-type semiconductors. Adsorption of certain molecules bends the bands at the surface, which can change the resistivity of the oxide. In this way, surface conductivity can be used to detect the presence of specific gas molecules. This is the basis for devices such as the electronic nose [8], and devices capable of detecting the MRSA bacterium [9]. Naturally forming oxides that spontaneously develop on many metal substrates can be exploited as cheap and effective protection layers against corrosion and environmental influences [10, 11]. Additionally, metal oxides are used in data storage devices [12], superconducting materials [13], photoactive materials [14] and solar cells [15].

Compared with most metals and semiconductors, the electronic structure of metal oxides is much more complicated [16]. Many metals - particularly transition metals and rare earth metals - display a range of different oxidation states, giving rise to different metal oxides. For example, in the case of vanadium the following oxides are known: VO (V^{2+}), V_2O_3 (V^{3+}), VO_2 (V^{4+}) and V_2O_5 (V^{5+}). In addition, there are a number of intermediate phases, some which are well defined (e.g. V_4O_9) and some that are essentially non-stoichiometric (VO_x, $0.8 \leq x \leq 1.3$). This chemical complexity has serious consequences for surface science. The reproducible preparation of metal oxide surfaces with known composition and properties may be difficult, with a wide range of chemical interactions possible with molecules chemisorbed differently on surfaces with varying properties.

Whilst the bulk properties of metal oxides are generally well understood [17], the

situation is less satisfactory for surface properties [16]. Complexity arises due to the absence of free electrons, especially in wide band-gap materials. This reduces the ability of the oxide to screen structural defects, thus affecting the electronic and chemical properties of the surface. Structural defects are a range of non-stoichiometric atomic arrangements such as point defects, interstitial atoms, step edges, kinks and corner sites. Each defect type is accompanied by a disruption of the local electronic structure, the most common type in metal oxides being oxygen vacancies [18].

A further complication is the large variety of possible surface configurations and terminations that can develop on one and the same bulk structure. Only in very few cases do actual surfaces correspond to a slice through the unperturbed crystal lattice. In most cases atoms rearrange themselves to minimise the Gibbs free energy [19]. Conditions during surface formation, such as oxygen partial pressure or presence of residual gases can also affect surface structure.

A practical difficulty is that many of the most interesting metal oxides are very good insulators, but many surface science techniques rely on the emission or absorption of charged particles. This means that samples with negligible conductivity often cannot be studied due to surface charging effects. Metal oxides are also poor thermal conductors, meaning heating is often inhomogeneous. Preparation of well-defined surfaces is also difficult - metals are usually prepared by sputtering and annealing, however both of these treatments cause a change in metal oxide stoichiometry. Cleavage is the preferred method of metal oxide surface preparation, but this too has its limitations.

1.2 Thin Films

Rather than studying bulk metal oxide crystals, thin films of up to 100 Å thickness can be grown on suitable metal substrates and are adequate to simulate the surfaces of bulk terminated crystals [20]. Using thin films has the following advantages over studies of the bulk surface [21]:

- The growth conditions can be controlled to give the desired stoichiometry.

- Films can be relatively easily renewed.

- The geometry of films is determined by the substrate.

- Similarly, the lattice match between substrate and film can be used to control defect concentration - the better the lattice match, the lower the defect concentration.

- It is possible to grow polar surfaces.

- Films have sufficient conductivity to be probed using charged particles.

Oxide films can be grown on native metal surfaces, on a foreign metal surface or on an alloy. The simplicity of growing a metal oxide film on a native metal surface is an advantage over other approaches. However, typically there are large mismatches in metal and metal oxide crystal lattices leading to a large concentration of defects in films. Furthermore, the native metal may not be able to withstand the treatments required to produce an ordered film. A metal can be deposited on a foreign metal surface, either in an oxygen background or in vacuum and subsequently annealed in oxygen to produce metal oxide films. Whilst this is more complicated, the choice of substrate provides a degree of control over the lattice mismatch, and thus some control over defect density. Similarly, there is control over the lattice mismatch when growing oxide films on an alloy. Additionally, alloys can have higher melting

points than the pure native metal (such as in the case of NiAl [22]) and so allow higher temperatures for surface preparation.

For films to sufficiently replicate bulk oxide chemistry, they require the same atomic structure and similar electronic structure. Due to the absence of surface charging, oxide thin films can be examined by spatially averaging surface science techniques such as low energy electron diffraction (LEED), diffraction techniques (such as XPD) - which provide information on structure - ultraviolet and X-ray photoelectron spectroscopy (UPS, XPS), electron energy loss spectroscopy (EELS) - which provide information on electronic properties - infrared absorption spectroscopy (IRAS), high resolution electron energy loss spectroscopy (HREELS) and temperature programmed desorption (TPD) - which provide information on adsorption behaviour. Whilst information provided from these techniques can reveal much about surface properties, most metal oxide surfaces exhibit non-equivalent sites that often only produce weak or undetectable signatures in spatially averaging techniques. This limitation is even greater when considering adsorption from the gas phase or deposition of metal clusters. Spatially resolving techniques such as atomic force microscopy (AFM) and scanning tunnelling microscopy (STM) can be used to provide real space information at an atomic scale. Whilst AFM probes the force between a tip and the surface, STM probes the local density of states (LDOS) and thus is limited to conductive samples. Thin films are electron transparent and thus an attractive sample for use with STM.

1.3   Thesis Overview

This thesis investigates the surface properties of two metal oxides, cerium dioxide (CeO_2) and titanium dioxide (TiO_2), using ultrathin films grown on suitable metal substrates.

CeO_2 is a key component in three-way converters (TWCs) that reduce the toxicity of automobile exhausts. This exploits the ability of CeO_2 to store and release oxygen, which accompanies a change in stoichiometry. The addition of precious metals such as Pd, Pt and Rh can promote catalytic activity, although this process is not fully elucidated.

TiO_2 is one of the most widely studied metal oxides. Since it has a multitude of uses, the nature its reactivity with two of the most abundant chemical species, water (H_2O) and oxygen (O_2) is an important consideration. The reactivity of TiO_2 surfaces is dominated by defects such as oxygen vacancies.

The experiments described in this thesis aim to expand current knowledge of both oxides using the surface science techniques of photoemission spectroscopy (PES) to provide information on electronic and chemical properties, and scanning tunnelling microscopy (STM) to examine surfaces and defects locally at the atomic scale.

The thesis is arranged as follows. In chapter 2, the techniques used in experiments are described, and the theory behind them discussed. Chapter 3 presents the vacuum systems used in the collection of data, and describes the instruments used. The effect of dosing Pd on ceria thin films grown on Pt(111) is examined in chapter 4 by comparing measurements of the stoichiometry using two complementary techniques, XPS and RESPES. In chapter 5, the growth of TiO_2 ultrathin films on W(100) is investigated with XPS, as is the reactivity of the TiO_2 surface with H_2O and O_2. Chapter 6 examines the surface morphology of TiO_2 ultrathin films grown on W(100) using STM and the effect of varying film thickness. Finally, chapter 7 summarises findings and places them in a wider context. Suggestions for extending the work are outlined.

References

[1] Trovarelli, A.; *Catal. Rev. Sci. Eng.*, **1996**, *38*, 439

[2] Connor, W.C., Falconer, J.L.; *Chem. Rev.*, **1995**, *95*, 759

[3] Iglesia, E.; *Appl. Catal. A*, **1997**, *161*, 59

[4] Yoon, B., Hakkinen, H., Landman, U., Worz, A.S., Antonietti, J.M., Abbet, S., Judai, K., Heiz, U.; *Science*, **2005**, *307*, 403

[5] Chen, M.S., Goodman, D.W.; *Science*, **2004**, *306*, 252

[6] Khodakov, A., Olthof, B., Bell, A.T., Iglesia, E.; *J. Catal.*, **1999**, *181*, 205

[7] Min, B.L., Wallace, W.T., Goodman, D.W.; *J. Phys. Chem. B*, **2004**, *108*, 14609

[8] Persaud, K., Dodd, G.; *Nature*, **1982**, *299*, 352

[9] Dutta, R., Dutta, R.; *BioMedical Eng. OnLine*, **2006**, *5*, 26

[10] Schweitzer, P.A.; *Fundamentals of Metallic Corrosion: Atmospheric and Media Corrosion of Metals, 2nd Ed.*, **2007**, Taylor & Francis, Boca Raton

[11] Jones, D.A.; *Principles and Prevention of Corrosion*, **1995**, Prentice Hall, Upper Saddle River

[12] Vollertsen, R.P.; *Microelectron. Reliab.*, **2003**, *43*, 865

[13] Imada, M., Fujimori A., Tokura, Y.; *Rev. Modern Phys.*, **1998**, *70*, 1039

[14] Ollis, D.E., Al-Ekabi, H., Eds.; *Photo-catalytic Treatment of Water and Air*, **1993**, Elsevier, Amsterdam

[15] O'Regan, B., Grätzel, M.; *Nature*, **1991**, *353*, 737

[16] Henrich, V.E., Cox, P.A.; *The Surface Science of Metal Oxides*, **1994**, Cambridge University Press

[17] Cox, P.A.; *Transition Metal Oxides*, **1992**, Clarendon Press, Oxford

[18] Pacchioni, G.; *Solid State Sci.*, **2000**, *2*, 161

[19] Nilius, N.; *Surf. Sci. Rep.*, **2009**, *64*, 595

[20] Street, S.C., Xu, C., Goodman, D.W.; *Ann. Rev. Phys. Chem.*, **1997**, *48*, 43

[21] Buschow, K.H.J., Cahn, R.W.; Flemings, M.C.; Ilschner, B.; Kramer, E.J.; Mahajan, S., eds.; *Encyclopedia of materials: science and technology*, **2001**, Elsevier Amsterdam

[22] Freund, H.J., Kulenbeck, H., Staemmler, V.; *Rep. Prog. Phys.*, **1996**, *59*, 283

Chapter 2

Theoretical Considerations

2.1 Introduction

In this chapter, the theoretical basis behind the techniques used in this thesis will be discussed. Surface science techniques have been employed to determine information about chemical composition - using X-ray photoelectron spectroscopy (XPS), resonance photoelectron spectroscopy (RESPES) and Auger electron spectroscopy (AES) - and physical structure - using scanning tunnelling microscopy (STM) and low-energy electron diffraction (LEED).

2.2 Photoelectron Spectroscopy, PES

2.2.1 Overview

Photoelectron spectroscopy (PES) is a widely used surface science technique, capable of chemical identification and nanostructure quantification. A photon source is used to irradiate a sample and incident photons cause the ejection of electrons from

atomic orbitals. The kinetic energy of ejected photoelectrons can be recorded across an energy range to build up a spectrum, from which chemical and physical data can be derived. The technique can be used to perform element specific analysis and quantitative analysis based on relative intensity of spectral peaks. Chemical information is also accessible, relating to the chemical environment and oxidation state of surface species. Due to the surface sensitivity of the technique, it is particularly useful for analysing adsorbates or thin-film overlayers. It is common for PES to be used in conjunction with other techniques where accurate surface characterisation is required. PES techniques are usually named according to the photon source used; in this thesis X-ray sources are used (XPS), as well as a variable energy synchrotron source for resonance photoemission spectroscopy (RESPES).

2.2.2 Historical development

The first description of the photoelectric effect was given by Hertz in 1887 [1]. However, this was a controversial discovery as it revealed that the theory of radiation at that time was incomplete. It took until 1905 for Einstein to explain (using Planck's concept of quantised energy) how low intensity, high frequency radiation could eject electrons from metal foils [2]. Although Einstein received the 1921 Nobel Prize for his work on the photoelectric effect, quantum theory remained controversial until further work in the 1920s, particularly de Broglie's proposed wave-particle duality theory [3].

The potential to use the photoelectric effect for spectroscopy had been recognised earlier, particularly through experiments by Moseley, Rawlinson and Robinson in Rutherford's laboratory, Manchester in the 1910s [4–8]. In early experiments, hard X-rays ($h\nu$=1.5-15 keV) were considered more useful than soft X-rays ($h\nu$=50-1500 eV) which had weaker penetrating power. In 1925 Robinson verified that elemental spectra could be realised [9], although experiments faced many inhibitive difficulties

- lack of availability of continuous high vacuum, inability to control and exclude stray interfering fields and the unrealised requirement for stable, integrated electronics.

It took until 1950s for these problems to be overcome. Siegbahn and co-workers at Uppsala, Sweden had spent the 1940s developing the field of β-ray spectroscopy, and realised the potential for electron spectroscopy using X-rays. In 1954 the group produced the first X-ray photoelectron spectrum, of a cleaved NaCl sample [10]. As the group used the new technique to examine other materials, it was not long after that the binding energy of C $1s$ lines in spectra from different carbon-containing compounds was observed to vary, thus providing the first evidence of chemical shift [11, 12]. Photoelectrons emitted from more electropositive atoms have less kinetic energy (and therefore greater binding energy). It was due to this phenomenon that Siegbahn - who shared the 1981 Nobel Prize for Physics for his work - dubbed the new technique electron spectroscopy for chemical analysis (ESCA). The technique, when using X-ray sources, is more commonly referred to as X-ray photoelectron spectroscopy (XPS).

2.2.3   Theory

In a standard PES experiment, a photon source is used to direct photons of a known energy, $h\nu$ at a sample. For XPS, X-ray guns are commercially available and the most commonly used fixed sources are the MgK_α (1253.6 eV) or AlK_α (1486.6 eV) lines, or sometimes a combination of both. Different photon sources can be used, for example ultraviolet lamps in ultraviolet photoelectron spectroscopy (UPS), or synchrotron sources. Incident photons can cause the ejection of electrons from atomic orbitals, and ejected photoelectrons leave the sample surface with a kinetic energy, E_K (figure 2.1). Photoelectrons can be detected by an energy analyser, which scans across a range of energy values to record a spectrum. Thus these quantities are related:
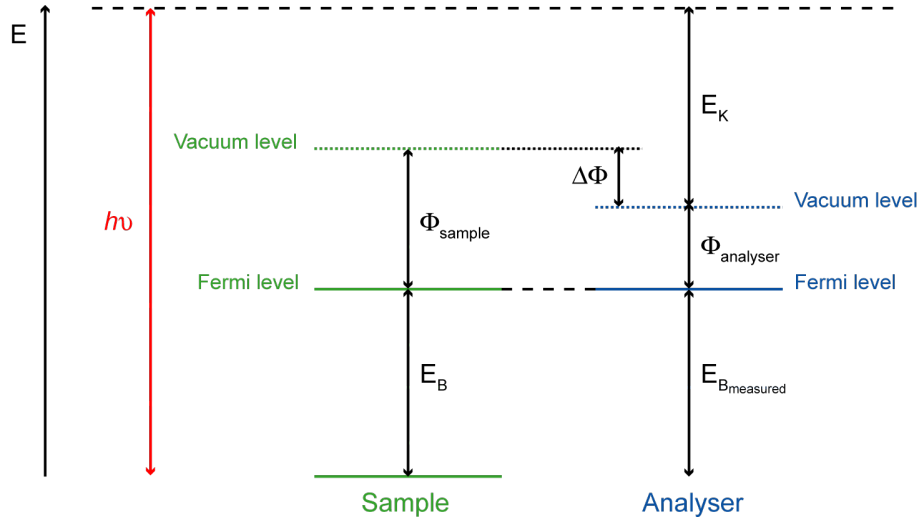
Figure 2.1: Energy level scheme showing the relationship between photon energy, $h\nu$, binding energy, E_B, kinetic energy, E_K and workfunctions, ϕ in XPS.

$$E_{B_{measured}} = h\nu - \phi_{sample} - \Delta\phi - E_K \tag{2.1}$$

where ϕ_{sample} is the workfunction of the sample, and $\Delta\phi = \phi_{analyser} - \phi_{sample}$, where $\phi_{analyser}$ is the workfunction of the energy analyser. This simplifies to:

$$E_{B_{measured}} = h\nu - \phi_{analyser} - E_K \tag{2.2}$$

2.2.4 Photoemission Process

The photoemission process describes how photons interact with electrons in the sample to produce photoelectrons, and can be separated into three stages.

Firstly, photons interact with electrons in the atoms of the sample, which can result in the emission of a photoelectron. The probability of a photoelectron being emitted on collision is determined by the photoionisation constant, σ, which is an energy dependent value. Values for σ have been calculated by several authors for each element at typical photon energies, and where used in calculations in this thesis have

been obtained from the comprehensive database compiled by Yeh and Lindau [13].

The second stage concerns the transfer of the photoelectron through the solid. When the photoelectron leaves the atom it may interact inelastically. The probability of this happening is quantified by the inelastic mean free path (IMFP), λ, which is the mean distance travelled by an electron. The IMFP is a function of the electron energy. Various formulae have been devised to calculate IMFP values, and where used in this thesis, IMFP values have been calculated using Tanuma and Powell's TPP-2 formula [15].

In this stage, the photoelectron could:

1. reach the surface without further interaction, contributing to the photoelectron current. If the photoelectron is detected by an energy analyser, an XPS peak will appear in the spectrum.

2. interact inelastically once, losing part of its energy. If detected by an energy analyser the photoelectron will contribute to intensity at a lower kinetic energy.

3. interact inelastically several times, losing sufficient energy to contribute to the secondary electron background on which all XPS peaks are superimposed.

4. remain absorbed in the solid, unable to escape from the surface and be detected.

Finally the photoelectron must overcome the surface barrier. This is represented quantitatively by the workfunction of the sample, ϕ_{sample}, which is the difference between the Fermi level (the highest filled state), E_F and the vacuum level (the energy level beyond which the electron is no longer bound to the atom). This is shown in energy terms in figure 2.2.
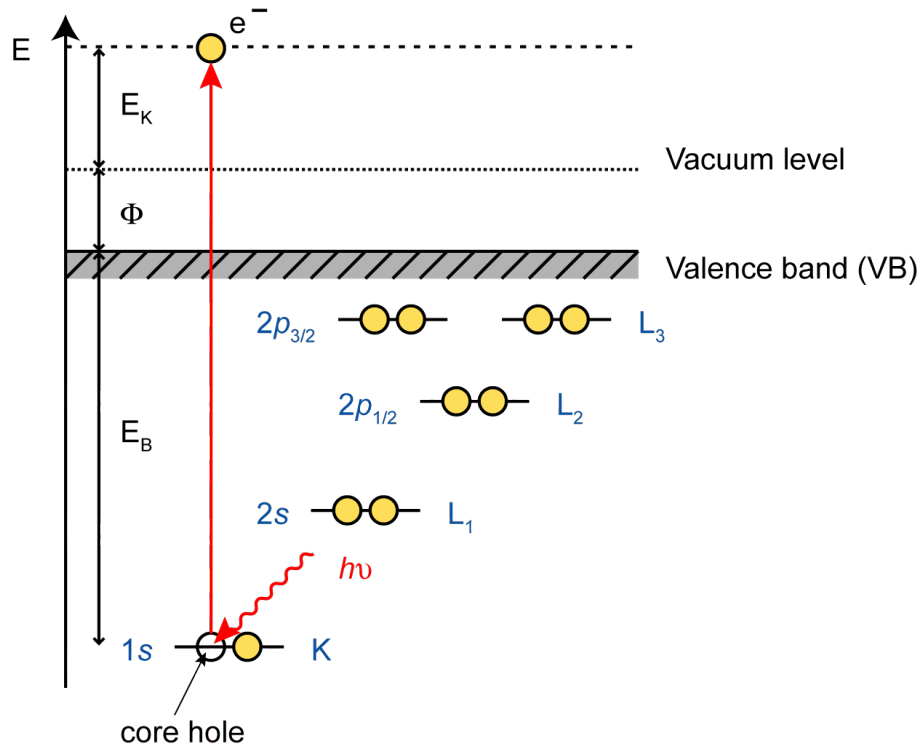
Figure 2.2: Energy level diagram of the photoemission process, in this case of a $1s$ electron.

2.2.5 Nomenclature of Peaks

In spectroscopy, labelling of atomic levels differs slightly to that of X-ray lines, taking the form:

$$nl_j \tag{2.3}$$

where n is the principal quantum number (the shell number), l is the orbital quantum number (describing the sub-shell shape, e.g. $s,p,d,f...$) and j is the total angular momentum:

$$j = |l + s| \tag{2.4}$$

where s is the spin quantum number. For an electron, $s = \pm\frac{1}{2}$. In the nomenclature shown in 2.3, the j term is required to describe the spin of remaining unpaired
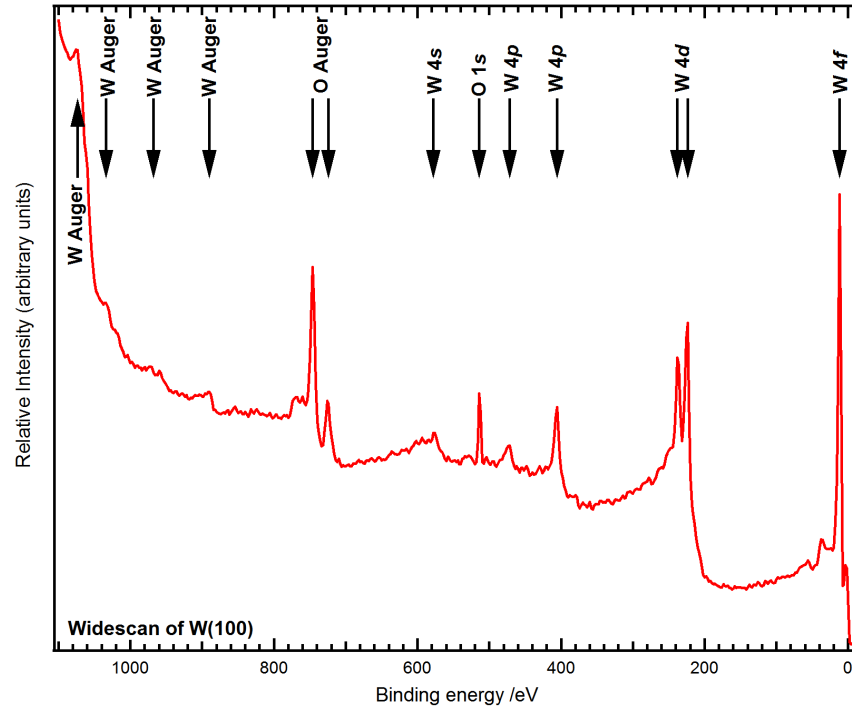
Figure 2.3: XPS widescan of a W(100) sample, with XPS and Auger peaks labelled. $h\nu = 1253.6$ eV.

electrons in an atom after the ejection of a photoelectron leaving a hole in the n,l level. Thus, s peaks ($l = 0$) appear in spectra as singlets since the only possible value for the total angular momentum is $j = \frac{1}{2}$. Peaks with $l \geq 1$ ($p,d,f...$) appear as doublets in spectra as in each case there are two possible values for j.

2.2.6 Spectral Features

Figure 2.3 shows a typical XPS spectrum across binding energies of 0-1100 eV of a W(100) sample (with a small amount of oxygen contamination) recorded using an Mg K_α source. A number of peaks appear superimposed on a background which decreases to lower binding energy (higher kinetic energy), and also shows stepped decreases after each significant peak. The features appearing in the spectrum can be classified in the following sections.

Core Level

Core level photoemission peaks appear as narrow, intense peaks in spectra. In figure 2.3, the core-level structure is a direct reflection of the electronic structure of W. The levels appearing in the spectrum are limited by the photon source energy, $h\nu$ which in the case of Mg K_α is 1253.6 eV. The W $4s$ level appears as a singlet peak at a binding energy of 595 eV, and the W $4p$ (E_B=492, 426 eV), $4d$ (E_B=259, 246 eV) and $4f$ (E_B=37, 34 eV) levels appear as doublets due to spin-orbit coupling.

Peak widths are defined by the full width at half-maximum (FWHM), ΔE, which is the convolution of contributions:

$$\Delta E = (\Delta E_n^2 + \Delta E_p^2 + \Delta E_a^2)^{1/2} \tag{2.5}$$

where ΔE_n is the natural or inherent line width of the core level, ΔE_p the width of the photon source and ΔE_a the resolution of the energy analyser, all expressed by the FWHM.

The uncertainty in the lifetime of the ion state resulting from photoemission defines the inherent line width of a core-level peak, ΔE_n, which can be obtained in units of eV from Heisenberg's uncertainty principle:

$$\Delta E_n = \frac{h}{\tau} = \frac{4.1 \times 10^{-15}}{\tau} \quad \text{eV} \tag{2.6}$$

where Planck's constant, h is expressed in eV·s and the lifetime, τ in s.

The shape of core level peaks depends on the nature of the material. For metallic elements, peaks have the Doniach-Šunjić [16] shape, that is, they are Lorentzian with an asymmetric tail. Non-metallic core level peaks are a convolution of Lorentzian (accounting for the inherent peak lifetime) and Gaussian (which accounts for the width of the photon source, the analyser resolution and thermal broadening) curves.

Gaussian-Lorentzian curves are known as Voigt curves and the FWHM of a Voigt curve is defined as [19]:

$$w(V) \approx \frac{w(L)}{2} + \sqrt{\frac{w(L)^2}{4} + w(G)^2} \tag{2.7}$$

where w is the FWHM of the Voigt (V), Lorentzian (L) and Gaussian (G) curves.

These peaks are superimposed on a background contribution. In a peak fitting calculation, the background is subtracted and peaks are fitted with appropriate line-shapes according to whether the sample is metallic or not. Applying a linear background - i.e. a straight line between the first and last set of points in a spectrum - provides a rough estimate but major errors can result from this approach [17]. An alternative approach is a Shirley background where an S-shape is applied to the background underneath peaks [18]. Whilst there are some errors involved in this approach, in many cases useful results have been obtained through its use. Peak fitting processes presented in this thesis incorporate Shirley backgrounds.

Valence Band

The valence band consists of low binding energy levels $(E_B \simeq$ 0-20 eV) involved in delocalised or bonding orbitals. This region contains many levels spaced closely together in energy, and this gives rise to band structure. The band structure differs according to whether the material is a conductor (metal) or an insulator. The filled valence band overlaps with the unfilled conduction band in a conductor, whereas in an insulator they are separated by a band gap. In the case of a conductor, the highest occupied energy level is termed the Fermi level, E_F. In XPS E_B values are generally referenced to E_F, which is easily measured.

If ejected photoelectrons from filled levels have E_K values that lie within the conduction band, intensity will be observed which is a convolution of both filled and

unfilled states together with the matrix of transition probabilities [17]. In XPS, the E_K of valence photoelectrons is such that the final states are without much structure, and observed density of states closely corresponds to the initial filled density of states.

At typical XPS photon energies, the photoionisation cross sections of valence level electrons are low, resulting in low intensity in general. Lower energy photon sources, such as those used in ultraviolet photoelectron spectroscopy (UPS), or variable energy synchrotron sources are more appropriate for studying the valence band.

Auger Peaks and Auger Electron Spectroscopy (AES)

When an atom is photoionised, the result is the creation of a core hole. The resulting ion can lose energy by filling this hole with an electron from a higher energy level. The energy produced by this process can be released by the ejection of a photon or a so-called Auger electron (illustrated in energy level terms in figure 2.4):

$$E_K = E_a - E_b - E_c \qquad (2.8)$$

where E_a is the core level, E_b the initial energy of the decaying electron level and E_c the initial energy level of the liberated Auger electron. Discovered independently by Meitner [20] in 1922 and Auger [21] in 1925, and named after the latter, Auger electrons are ejected at discrete values of E_K depending on the two energy levels involved in the transition. Auger peaks appear in spectra at the same kinetic energy regardless of the photon source used. Auger peaks for both W and O appear in the XPS spectrum shown in figure 2.3.

Instead of a photon source, a beam of electrons can be used to excite Auger electrons from a surface. Scanning across a range of ejected electron energies builds up a spectrum of Auger states. Auger electron spectroscopy (AES) allows composition-depth
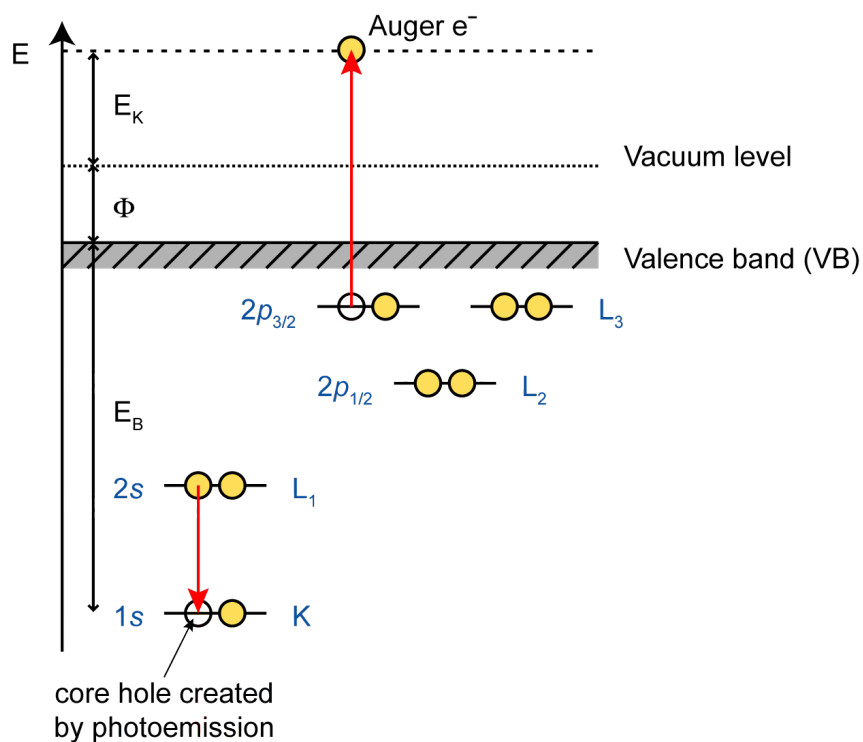
Figure 2.4: Energy level diagram showing the emission of an Auger electron, in this case from the $2p_{3/2}$ level.

profiling and elemental identification. AES is commonly combined with low-energy electron diffraction (LEED) units on systems where other spectroscopic methods are not available (see chapter 3).

Secondary Electrons

Ejected photoelectrons can interact inelastically with other atoms in the sample, causing the emission of secondary electrons which can contribute to the spectrum as secondary electron peaks.

2.2.7 Initial and Final State Effects

The measured binding energy of an ejected photoelectron is simply the difference between the initial n electron system prior to photoemission, $E_i(n)$ and the $(n-1)$-electron final state energy after photoemission, $E_f(n-1)$:

$$E_B^m = E_f(n-1) - E_i(n) \tag{2.9}$$

This implies that the observed binding energy, E_B^m is equal to the negative orbital energy, $-\varepsilon_K$ for the emitted photoelectron:

$$E_B^m \simeq -\varepsilon_K \tag{2.10}$$

which is an approximation of Koopmans' theorem [22]. Values of ε_K can be calculated using the Hartree-Fock method. These values provide a good approximation for core levels and typically are within 10-30 eV of actual E_B values for valence levels. This discrepancy arises as Koopmans' theorem and the Hartree-Fock calculation method do not account fully for all factors contributing to E_B. The assumption that other electrons remain static during the photoemission process in particular is invalid. During the emission of a photoelectron, a core hole is created and other electrons react to shield - or minimise - the energy of the ionised atom. The accompanying energy reduction is termed the relaxation energy, E_r. This term accounts for both atomic relaxations in the photoionised atom and atomic relaxations occurring in surrounding atoms. Taking this into account, a more complete expression for E_B is given by:

$$E_B = -\varepsilon_K - E_r - E_{corr} - E_{relat} \tag{2.11}$$

where $E_r = E_{inter-atom} + E_{extra-atom}$ is the relaxation energy, and E_{corr} and E_{relat} are correction factors accounting for the electron correlation and relativistic energy,

respectively [17, 23].

Equation 2.9 indicates that both initial (n) and final $(n-1)$ states contribute to the observed E_B. This can occur in a number of ways which are discussed in the following sections.

2.2.8 Initial State Spectral Features

The initial state is simply the ground state of the atom, prior to photoemission.

Chemical Shift

The E_B of core-level peaks of the same element in different chemical environments is observed to shift, and this was a defining part of the early development of XPS. Non-equivalence can arise from variations in oxidation state of the atom, the molecular environment or lattice site. Due to increasing effective nuclear charge, atoms of higher oxidation state will have core-level peaks shifted to slightly higher E_B.

Spin-Orbit Splitting

As mentioned in section 2.2.6, spin-orbit splitting gives rise to doublet peaks for p, d and f orbitals (but not s orbitals). For any electron, coupling of magnetic fields of spin, s and angular momentum, l occurs, since the total angular momentum, $j = |l+s|$. Since $s = \pm\frac{1}{2}$ for an electron, there are two possible situations ($j = |l\pm\frac{1}{2}|$), (figure 2.5).

The lower j value of the doublet is at higher E_B (e.g. $E_B(2p_{1/2}) > E_B(2p_{3/2})$). The magnitude of spin-orbit splitting increases with the effective nuclear charge, Z, and decreases with distance from the nucleus. The intensity ratio of doublet peaks is given by their respective degeneracies $(2j + 1)$, which are summarised in table 2.1.
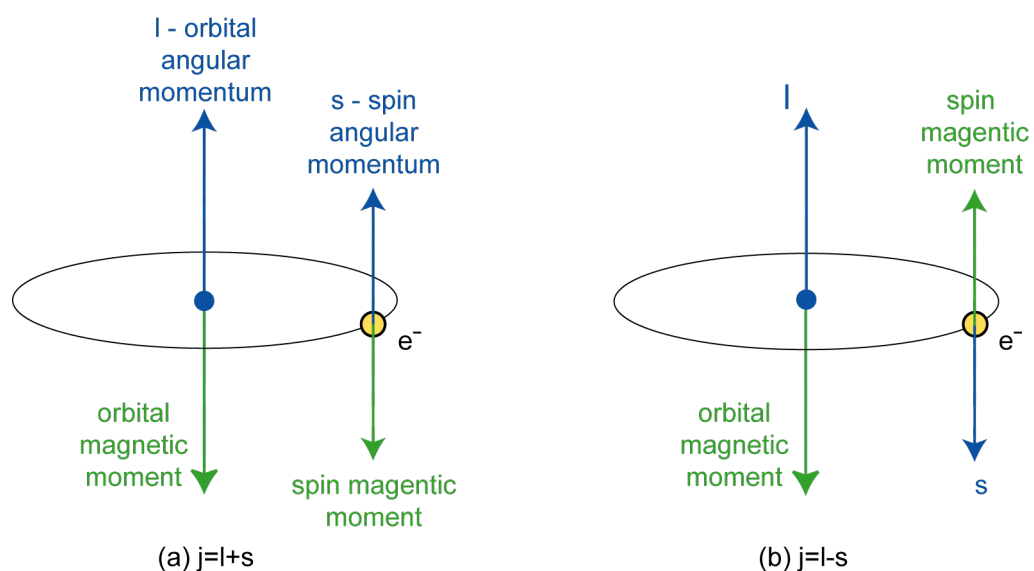
Figure 2.5: The two conditions which lead to spin-orbit coupling and the appearance of doublet peaks for electrons from energy levels where $l \geq 1$ (p,d,f... etc.).

Subshell	j values	Area ratio
s	$\frac{1}{2}$	-
p	$\frac{1}{2}$, $\frac{3}{2}$	1 : 2
d	$\frac{3}{2}$, $\frac{5}{2}$	2 : 3
f	$\frac{5}{2}$, $\frac{7}{2}$	3 : 4

Table 2.1: Intensity ratios for doublet peaks [17].

2.2.9 Final State Spectral Features

Final state effects arise due to the reorganisation - or relaxation - of the remaining $(n-1)$ electrons in response to the suddenly created increase in effective nuclear charge, Z following photoemission.

Shake-up/Shake-off Satellites

When relaxation involves the excitation of a valence electron to a higher, unfilled energy level, a shake-up satellite will be observed in the spectrum. The required relaxation energy is not available to the primary photoelectron and so this two electron process results in discrete structure on the lower E_K side of the primary photoemission peak. Typically the intensity of shake-up satellites is low ($< 10\%$ of the primary peak). However, very strong satellites are observed for certain transition metal and rare earth compounds which have unpaired electrons in $3d$ or $4f$ shells respectively. In the final state, there is significant ligand-metal charge transfer such that an extra electron is present in the $3d$ or $4f$ levels compared with the initial state. This phenomenon is only observed in open shell systems (e.g. Cu^{2+}, $3d^9$), and not in closed shell systems (e.g. Cu^+, $3d^{10}$). In this instance a better description than "shake-up" would be that a strong configuration interaction occurs in the final state due to relaxation [14]. It is this phenomenon that leads to the complex structure observed for Ce $3d$ spectra of mixed-valence cerium compounds (figure 2.6). This is discussed in further detail in chapter 4.

Rather than excitation to a higher unfilled valence level, a valence electron could be excited to the unbound vacuum level, completely ionising the atom and resulting in a shake-off satellite. The resulting ion then has vacancies in both core and valence levels. However, discrete shake-off peaks are rarely observed in the solid state.
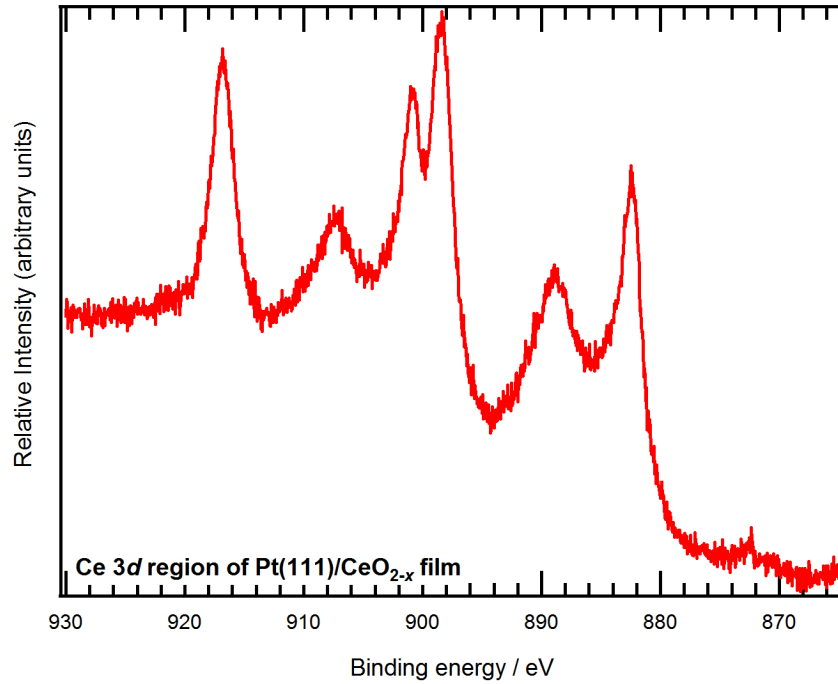
Figure 2.6: XPS spectrum of the Ce $3d$ region of $Pt/CeO_{2\text{-}x}$ that shows the complex shake-up satellite structure. $h\nu = 1486.6$ eV.

2.2.10 Analysis Depth

The intensity observed in an XPS spectrum arises from emission of photoelectrons detected from the sample. The depth from which detected photoelectrons originate from in a solid is determined by the inelastic mean free path (IMFP), λ. Only those photoelectrons that have minimal energy loss are likely to be detected and thus contribute to a spectrum. The IMFP is a function of the kinetic energy, E_K of the electron and hence of the photon source, $h\nu$ [15]. In XPS, where photoelectrons have kinetic energies in the range of 15-1000 eV, IMFPs are relatively short - typically between ~10-20 Å. Thus XPS is highly sensitive to the top layers of a solid and to any adsorbates or overlayers that may be on the surface. A universal escape depth curve shows the IMFP value across an energy range (figure 2.7) [24].
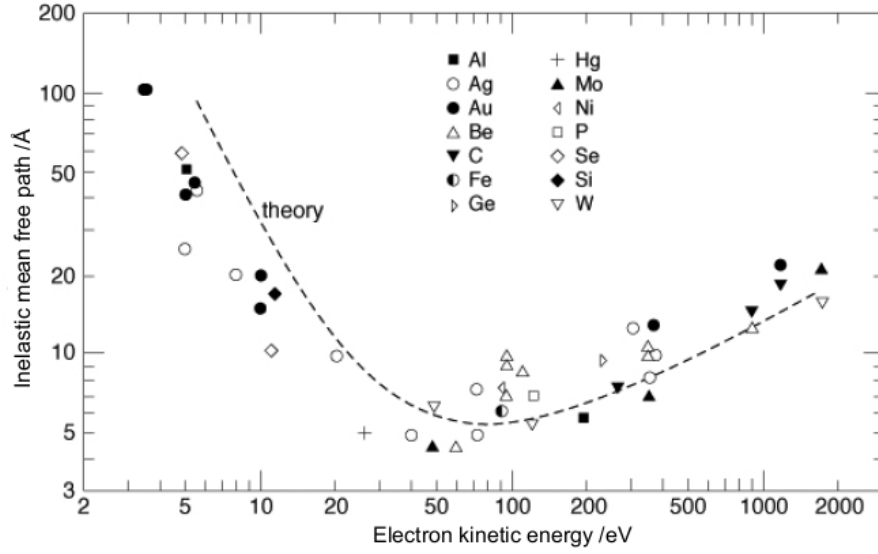
Figure 2.7: Inelastic mean free path variation with energy. From [24].

2.2.11 Resonance photoemission spectroscopy (RESPES)

Giant resonance occurs when essentially all the oscillator strength of some X-ray absorption edge appears in a series of relatively narrow lines. This phenomenon can be used in a spectroscopic capacity in resonant photoemission spectroscopy (RESPES). The angular momentum selection rule for an electronic transition is $l \rightarrow (l+1)$. Typically, when the final state $(l+1)$ is associated with a partially filled inner atomic shell, resonance can occur. For example, giant resonances are observed for the $3p \rightarrow 3d$ transition in transition metals, the $4d \rightarrow 4f$ transition in rare earth metals and the $5d \rightarrow 5f$ transition in actinides. These final states can then decay through various channels.

RESPES exploits a decay channel that proceeds in an Auger-like manner. The core hole (created by photoemission) is refilled by an electron from the final state shell, and another electron is ejected beyond the vacuum level. This ejected electron can be detected by an energy analyser.

Photoemission of a $4f$ electron from a rare earth metal can be described by the

process:

$$4d^{10}4f^n \xrightarrow{h\nu} 4d^{10}4f^{n-1}\epsilon_K + \mathrm{e}^- \tag{2.12}$$

Additionally, a resonance contribution can take place:

$$4d^{10}4f^n \xrightarrow{h\nu} 4d^9 4f^{n+1} \longrightarrow 4d^{10}4f^{n-1}\epsilon_K + \mathrm{e}^- \tag{2.13}$$

where ϵ_K is the outgoing photoelectron state. Since the initial and final states in equations 2.12 and 2.13 are the same, constructive interference (Fano resonance) occurs appearing as an enhancement of photoemission peaks in spectra.

Resonant peaks have Fano line-shapes as defined by:

$$f(\epsilon) = \frac{(q+\epsilon)^2}{1+\epsilon^2} = 1 + \frac{q^2 - 1 + 2q\epsilon}{1+\epsilon^2} \tag{2.14}$$

where q is the Fano parameter (a function of transition probability) and the reduced energy variable ϵ is:

$$\epsilon = \frac{E - E_\phi - F(E)}{\pi |V_E|^2} \tag{2.15}$$

where ϕ represents the intermediate state of process 2.13 with a core hole, $F(E)$ is a self-energy arising from the interaction with the continuum and V_E the Auger matrix element for the second step of process 2.13. Thus the resonant energy of state ϕ is shifted $F(E)$ from E_ϕ. This shift can be defined:

$$F(E) = P \int dE' \frac{|V_E|^2}{E - E'} \tag{2.16}$$

where P is the principal value. The asymmetric Fano line-shape is shown in figure 2.8 for several values of q.

RESPES measurement can be done in two modes. In constant initial state (CIS) mode, $h\nu$ and electron analyser energy are simultaneously varied such that the
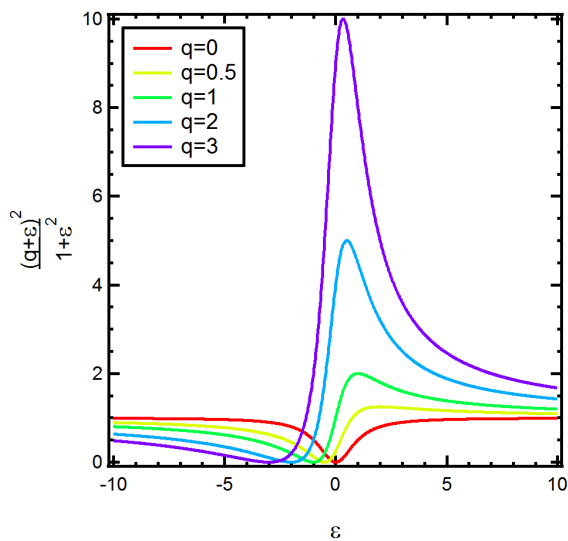
Figure 2.8: Fano line-shapes for various values of the Fano parameter, q.

ionisation energy $E_I = h\nu - E_K$ is held constant. Alternatively, using constant final state (CFS) mode involves varying only $h\nu$ while the detected E_K is held at a constant value on the inelastic tail of the E_K distribution [25].

RESPES of Rare-Earth Metals

In 1978, four papers [26–29] reported resonance associated with the $4d$-$4f$ transition in rare-earth solids. Because the technique is atom-specific, and sometimes orbital- and valence-specific, RESPES has evolved as a useful spectroscopic tool for identifying particular components in a PES spectrum. This is particularly useful in mixed valence compounds as different valence states can be identified and quantified.

2.3 Scanning Tunnelling Microscopy (STM)

2.3.1 Overview

Scanning tunnelling microscopy (STM) is an extremely powerful surface science technique that facilitates the imaging of surface topography by the use of electron tunnelling. Since its development in the early 1980s, STM has become a useful tool and its use is not limited to surface science, having been applied to the fields of geology, biology and metrology [30]. The key advantages of STM are the ability to produce real space images of atomic resolution, and - unlike other surface science techniques - STM has no requisite long or short range surface order meaning that non-periodic features such as defects, growth centres and reaction sites can be imaged. However, the technique is limited by a lack of chemical specificity, meaning an exact interpretation of STM images can be difficult without theoretical analysis.

2.3.2 Historical development

In his famous 1959 lecture *There's Plenty of Room at the Bottom*, the American physicist Richard P. Feynman declared:

> The problems of chemistry and biology can be greatly helped if our ability to see what we are doing, and to do things on an atomic level, is ultimately developed - a development which I think cannot be avoided. [31]

It took just a couple of decades for Feynman's prescience to be realised. In 1971, Young described the development of a "topografeiner" at the National Bureau of Standards (now the National Institute of Standards and Technology, NIST), a device which was capable of producing 2-dimensional contour maps [32, 33]. The
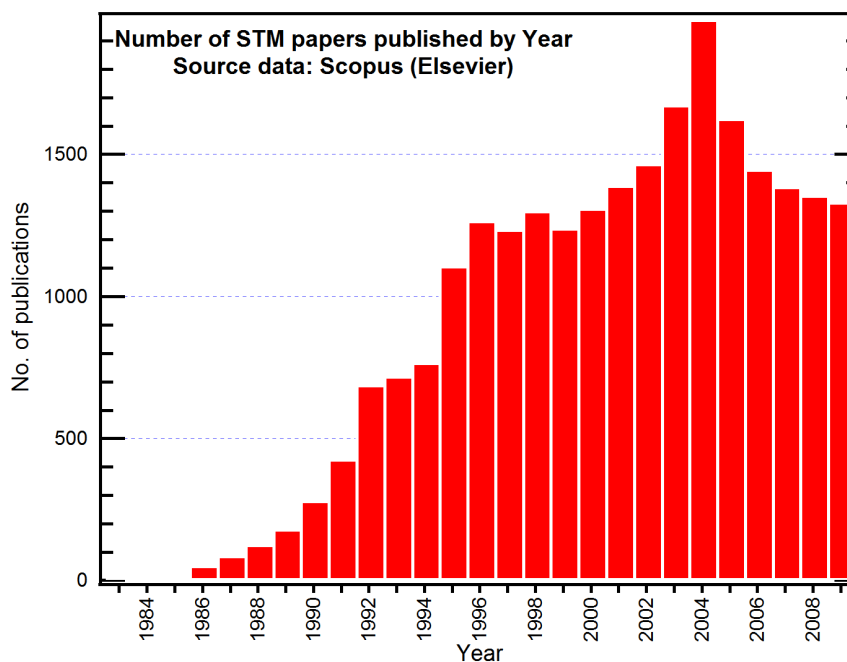
Figure 2.9: Number of STM papers published by year. Source: Scopus.com.

topografeiner used emission field current between a sharp tungsten probe and the sample surface. It was later realised that better resolution should be obtained by using an electron tunnelling current instead. In the early 1980s, Binnig and Rohrer described their invention of the scanning tunnelling microscope (STM) [34], an event that led to them sharing the 1986 Nobel Prize for Physics. Initially however, STM was treated with scepticism by the surface science community but when Binnig and Rohrer used the technique to solve a well-known outstanding problem in the field - the structure of Si(111)(7 ×7) [35] - the technique gained credibility.

In 1990, Eigler and Schweizer - workers at IBM - published the famous image of the initials of their company's name written out using 35 Xe atoms, demonstrating the ability of STM to manipulate single atoms [36]. The popularity of the technique grew and the number of STM papers published each year rose throughout the 1980s and 1990s and in the last ten years has averaged around 1500 papers a year (figure 2.9).
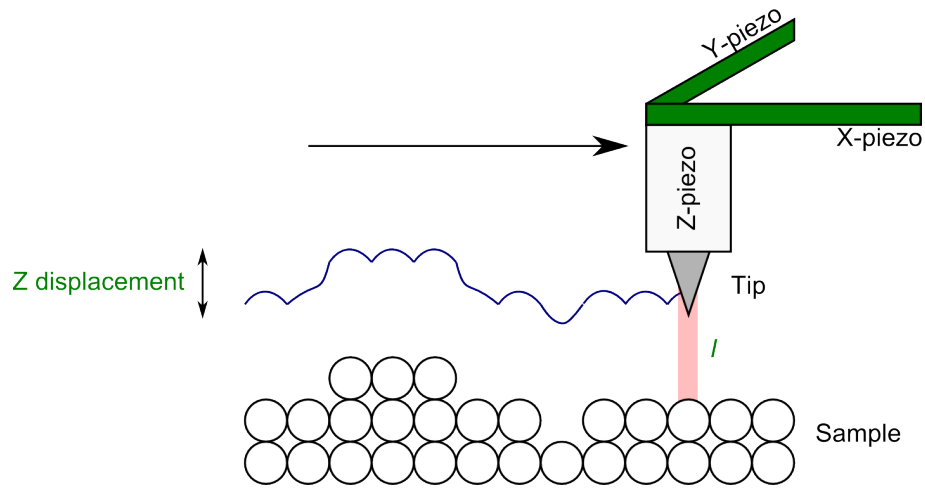
Figure 2.10: Schematic diagram of an STM experiment. An atomically sharp tip is brought close to a sample surface. When a potential bias is applied, a tunnelling current I is passed between the tip and the surface. If this is held constant and the tip is rastered over the surface by varying the X- and Y-piezos, a map of the Z-displacement is built up.
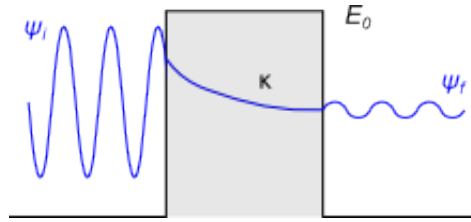
Figure 2.11: Schematic diagram of a particle tunnelling through a one-dimensional potential barrier of E_0. ψ_i and ψ_f are the incident and transmitted wavefunctions, respectively; κ is the decay constant inside the barrier.

2.3.3 Theory

The basis for STM lies in the effect of quantum mechanical tunnelling (figure 2.10). The sample surface is probed using an atomically sharp, conducting tip, typically of W or PtIr. A bias is applied between the tip and the sample, and when the tip is manipulated to sufficiently close proximity of the surface (but not into mechanical contact), the wavefunctions of the tip and the sample can overlap, allowing quantum tunnelling of electrons between them. This can be illustrated by considering a particle impinging upon a one-dimensional potential energy barrier, of energy E_0
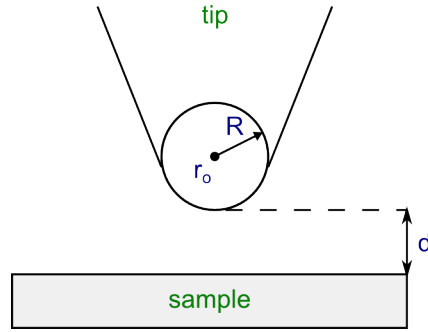
Figure 2.12: The tip model used in the Tersoff-Hamann approximation [38].

(figure 2.11). According to classical physics, the particle cannot traverse the barrier if it has an energy $E < E_0$. In the quantum realm however, the particle is considered as a wavefunction, ψ that describes it in terms of the probability of finding the particle at a particular point in space. The phenomenon of quantum tunnelling dictates that the particle has a finite probability of being found beyond the potential barrier. The early analysis of the tunnelling current between an STM tip and sample surface was based on a one-dimensional tunnelling problem [37]. In the low tip bias and low temperature regime, the tunnelling current, I is given by [34]:

$$I \propto \exp(-2\kappa d) \tag{2.17}$$

where κ is the decay constant for wavefunctions in the barrier and d is the sample-tip separation distance. For vacuum tunnelling, κ is related to the local workfunction, ϕ:

$$\kappa = \sqrt{\frac{2m\phi}{\hbar^2}} \tag{2.18}$$

Typically, metals have workfunctions of a few eV, giving κ values of around 1 Å^{-1}. Substituting this value into equation 2.17 results in an order of magnitude change in I as d changes 1 Å. It is this exponential dependence of I on d that allows STM such sensitivity in measuring surface topography.

However, for detailed information, a more complex formalism is required. Tersoff

and Hamann [38] made the first attempts at such a formalism. Since the dominant factor in determining the STM image is the relative change over the surface rather than the absolute value of the tunneling current, Bardeen's perturbation theory was used to evaluate the tunnelling current. However, this treatment neglects a detailed description of the wavefunction tail in the gap region.

Bardeen's equation for the tunnelling current is:

$$I = \frac{2\pi e}{\hbar} \sum_{\mu\nu} f(E_\mu)[1 - f(E_\nu + eU)] \cdot |M_{\mu\nu}|^2 \delta(E_\mu - E_\nu) \qquad (2.19)$$

where $f(E)$ is the Fermi distribution, U is the applied bias, $M_{\mu\nu}$ is the tunnelling matrix element between the states ψ_μ of the tip and ψ_ν of the surface and E_μ and E_ν are the eigenvalues of the ψ_μ and ψ_ν respectively. $\delta(E_\mu - E_\nu)$ gives the conservation of energy in elastic tunnelling. The problem is then reduced to evaluating the matrix element, which is given by [39]:

$$M_{\mu\nu} = -\frac{\hbar^2}{2m} \int (\psi_\mu^* \nabla \psi_\nu - \psi_\mu \nabla \psi_\nu^*) d\mathbf{S} \qquad (2.20)$$

where $\mathbf{S}$ is the surface of the area lying under vacuum. Tersoff and Hamann approximated the STM tip as a locally spherical potential well with radius of curvature R about the centre r_O and a distance d away from the surface (figure 2.12). The tunnelling current in the Tersoff-Hamann formalism is thus:

$$I \propto U n_t(E_F) \cdot e^{2\kappa' R} \cdot \sum_\nu |\psi_\nu(\mathbf{r}_O)|^2 \delta(E_\nu - E_F) \qquad (2.21)$$

where $\kappa' = \frac{2m\phi}{\hbar}$, ϕ is the effective local potential barrier height, $n_t(E_F)$ is the density of states (DOS) of the tip at the Fermi level, R is the effective tip radius, and $\mathbf{r}_O$ is the centre of curvature of the tip. Therefore, in the Tersoff-Hamann approximation, STM images are interpreted as contour maps of constant surface
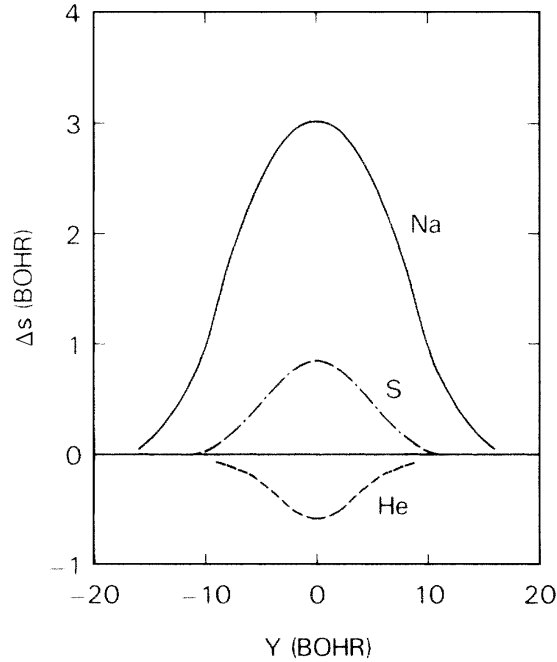
Figure 2.13: Calculated height displacement of a model Na-topped jellium tip when scanned across a jellium surface with adsorbates Na, S and He. 1 Bohr = 0.53Å. Figure from [40].

local density of states (LDOS) at E_F,$\mathbf{r}_O$. It is important to note that wavefunctions decay exponentially with tip-surface separation, s, as does the tunnelling current, I.

Lang [40] used *ab initio* calculations within the Tersoff-Hamann formalism to demonstrate that STM indeed images the LDOS at the Fermi level rather than the true surface topography. In these calculations, the STM tip is modelled as a flat jellium electrode with a single Na atom adsorbed at its apex. Three adsorbates were modelled as a Na atom, a S atom and a He atom on a second jellium electrode. In the calculations, the tip was scanned over each of the adsorbates at a constant I. The results are shown in figure 2.13. Scanning over the Na and S atoms caused a positive tip displacement, greater for the Na atom than the S. The Na atom sits higher on the surface and also has a greater DOS at the Fermi level than S. Scanning over the He atom resulted in a depression, or negative tip displacement. Clearly the true height of a He atom is positive, however He has a closed valence level around 20
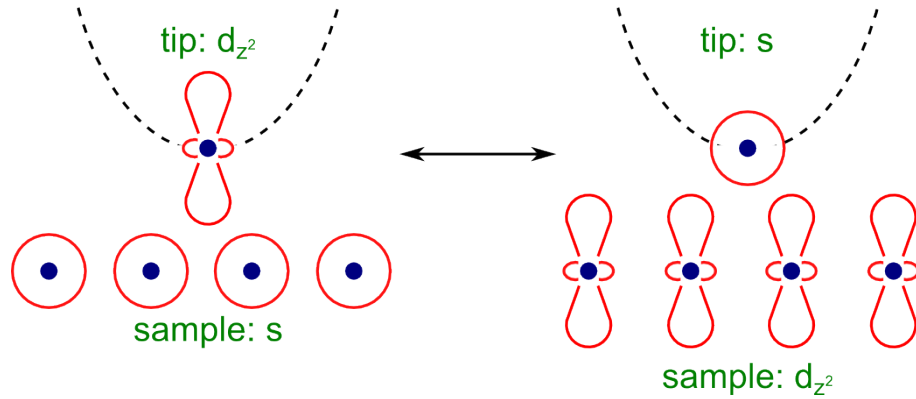
Figure 2.14: Illustration of Chen's reciprocity principle [41].

eV below the Fermi level, and the adsorbate screens the metallic electrons from E_F. Therefore, the DOS at the Fermi level is less than for the clean surface and the tip has to move closer to the surface to maintain constant current.

Based on the approximations above, the evaluated spatial resolution of STM is inconsistent with experimental evidence that shows atomic resolution can be achieved. Chen [41] introduced the reciprocity principle, which stated that if the tip and surface states were interchanged, the resulting STM image should remain the same (figure 2.14). Commonly used tip materials, such as W and PtIr are d-band metals, and in the instance of W around 85% of the DOS at the Fermi level is a contribution from d states. There is also a tendency for d states in W to form highly localised d_{z^2} dangling bonds [42] which are likely to play an important role in tunnelling. Chen simulated an atomically resolved corrugation by scanning an s-wave tip over a d_{z^2}-wave surface, which accounts for the observed atomic resolution in experimental STM images. Chen also noted the importance of knowing the nature of the tip apex atom when estimating the maximum corrugation of an STM image.

The Tsukada formalism [43] clearly shows the importance of the nature of the tip in STM. The tunnelling current was calculated using the Bardeen equation (2.19), but unlike the Tersoff-Hamann formalism the electronic structures of the tip and the surface are calculated self-consistently using a linear combination of atomic

orbitals (LCAO). This model was used to calculate STM images of a graphite-like structure, using various tip configurations. These configurations included variations in size, structure and chemical composition. It was found that removing the apex atom from a 9-atom large W(111) tip shifts the current contour map. The chemical composition of the tip was varied by introducing embedded C atoms. One C atom had little effect, however 3 C atoms caused an inversion in current maxima and minima.

It should be noted that despite various approaches to establishing formalisms, the corrugation of STM images is still not fully understood.

STM of metal oxides is reviewed by Bonnell [44]. Metal oxides are usually materials with a band gap in which the Fermi level is located. Additionally, it must be considered that the bias between the tip and the surface is dropped across the sample in a space charge region directly below the tip. This region can be evaluated at 0 V bias by:

$$d = \sqrt{\frac{2\epsilon kT}{q^2 N}} \tag{2.22}$$

where ϵ is the sample permittivity, k the Boltzmann constant, T the temperature, q the charge of an electron and N the density of charge carriers. Hence, the spatial resolution may be limited by radius of space charge region.

2.4 Low-Energy Electron Diffraction (LEED)

LEED provides information on the long-range order of crystal surfaces from the diffraction patterns of low-energy electrons directed at the sample. Whilst LEED can provide complex information about surface structure, in experiments presented in this thesis it is only used to check that surfaces are ordered and to derive some information about overlayer and adsorbate structures. Thus only a brief description

of the technique will be given here.

2.4.1   Historical development

The angular dependence of elastically back scattered electrons in a diffraction pattern from a Ni target was first observed by experiments by Davisson and Germer [45], and provided the first experimental evidence of de Broglie's earlier postulation of electronic wave-like properties [3].

Although one of the oldest surface science techniques, it was not until ultra-high vacuum conditions became more accessible in the 1960s that LEED became a popular tool for surface analysis.

2.4.2   Theory

As postulated by de Broglie [3], electrons have an associated wavelength, λ which can be estimated from the modified de Broglie equation:

$$\lambda(\text{Å}) = \left(\frac{150.6}{E(\text{eV})} \right)^{\frac{1}{2}} \tag{2.23}$$

This wave-like property of electrons allows them to be diffracted. The basis for diffraction lies in Bragg's law:

$$n\lambda = 2d \cdot \sin\theta \tag{2.24}$$

where n is the number of wavelengths difference between planes, d is the lattice spacing and θ is the angle between the incident radiation and scattering planes. Figure 2.15 shows conditions for constructive and destructive interference. When n is a whole integer, diffracted electrons are completely in phase and constructive interference occurs. Conversely, diffracted electrons are completely out of phase when n is a half integer value, and destructive interference occurs. The result is
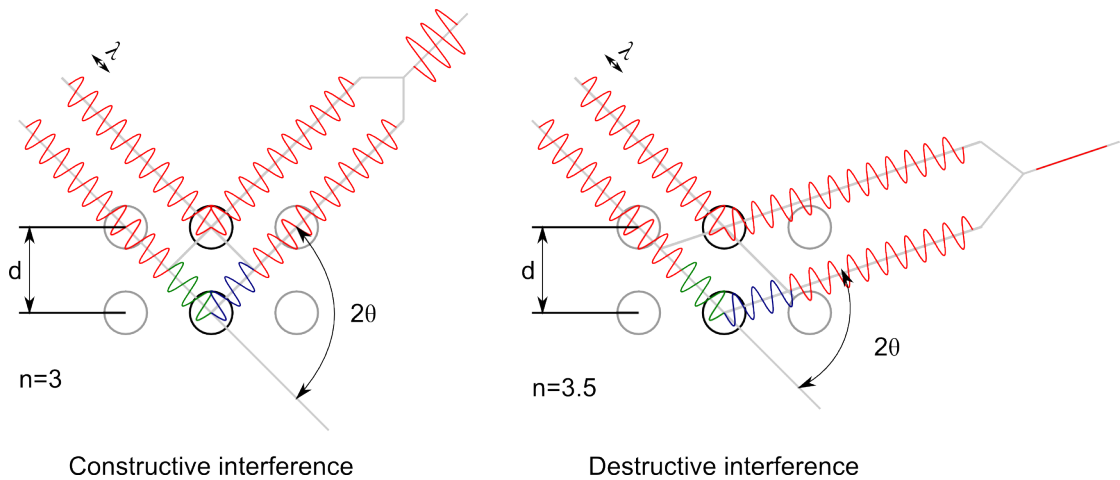
Figure 2.15: Bragg's law conditions for constructive and destructive interference.

that at specific angles, a discrete beam of diffracted electrons will cause a diffraction pattern on a suitable detector.

2.4.3 LEED measurement

An electron gun is used to direct an electron beam in the energy range 0-1000 eV at a sample. If the sample is well ordered, electrons are backscattered and can be detected to show a two-dimensional diffraction pattern. The resulting diffraction pattern is a two-dimensional reciprocal space representation of the surface unit cell periodicity. In reciprocal space, a reciprocal vector $\underline{\mathbf{a}}$ is related to its real space vector, $\mathbf{a}$ by:

$$\underline{\mathbf{a}} = \frac{2\pi}{\mathbf{a}} \tag{2.25}$$

The technique is highly surface sensitive (probe depth is around 10 Å) and so can provide information about surface structure and adsorbates or overlayers.

References

[1] Hertz, H.; *Wiedemannsche Ann. Phys.*, **1887**, *31*, 982

[2] Einstein, A.; *Ann. Phys.*, **1905**, *17*, 132

[3] De Broglie, L.; *Recherches sur la theorie des quanta*, Thesis, Paris, **1924**

[4] Moseley, H.G.J.; *Phil. Mag.*, **1913**, *26*, 1024

[5] Moseley, H.G.J.; *Phil. Mag.*, **1914**, *28*, 703

[6] Robinson, H., Rawlinson, W.F.; *Phil. Mag.*, **1914**, *28*, 277

[7] Rutherford, E., Robinson, H., Rawlinson, W.F.; *Phil. Mag.*, **1914**, *28*, 281

[8] Rawlinson, W.F.; *Phil. Mag.*, **1914**, *28*, 274

[9] Robinson, H.; *Philos. Mag.*, **1925**, *50*, 241

[10] Jenkin, J.G., Leckey, R.C.G., Liesegang, J.; *J. Electron Spectrosc. Rel. Phenom*, **1977**, *12*, 1

[11] Nordling, C., Sokolowski, E., Siegbahn, K.; *Phys. Rev.*, **1957**, *105(5)*, 1676

[12] Sokolowski, E., Nordling, C., Siegbahn, K.; *Arkiv for Fysik*, **1957**, *12(4)*, 301

[13] Yeh, J.J., Lindau, I.; *Atomic and Nuclear Data Tables*, **1985**, *32*, 1

[14] Brundle, C.R., Baker, A.D.; *Electron Spectroscopy: Theory, Techniques and Applications Vol.2*, **1978**, Academic Press, London

[15] Tanuma, S., Powell, C.J., Penn, D.R.; *Surf. Interf. Anal.*, **1991**, *17*, 911

[16] Doniach, S., Šunjić, M.; *J. Phys. C: Solid State Phys.*, **1970**, *3*, 285

[17] Briggs, D., Seah, M.P., Eds.; *Practical Surface Analysis by Auger and X-ray Photoelectron Spectroscopy*, **1983**, John Wiley & Sons Ltd.

[18] Shirley, D.A.; *Phys. Rev. B*, **1972**, *5*, 4709

[19] Whiting, E.E.; *J. Quant. Spectrosc. Radiat. Transfer*, **1968**, *8*, 1379

[20] Meitner, L.; *Z. Physik.*, **1922**, *9*, 131

[21] Auger, P.; *J. Phys. Radium*, **1925**, *6*, 205

[22] Koopmans, T.; *Phisica*, **1933**, *1*, 104

[23] Barr, T.L.; *Modern ESCA: the principles and practice of X-ray photoelectron spectroscopy*, **1994**, CRC Press, Inc.

[24] Zangwill, A.; *Physics at surfaces*, **1998**, Cambridge University Press

[25] Bachrach, R.Z., Ed.; *Synchrotron Radiation Research: Advances in Surface and Interface Science, Vol. 1: Techniques*, **1992**, Plenum Press, New York

[26] Lenth, W., Lutz, F., Barth, J., Kalkoffen, G., Kunz, C.; *Phys. Rev. Lett.*, **1978**, *41*, 1185

[27] Allen, J.W., Johansson, L.I., Bauer, R.S., Lindau, I., Hagström. S.B.M.; *Phys. Rev. Lett.*, **1978**, *41*, 1499

[28] Johansson, L.I., Allen, J.W., Gustafsson, T., Lindau, I., Hagström, S.B.M.; *Solid State Commun.*, **1978**, *28*, 53

[29] Gudat, W., Alvarado, S.F., Campagna, M.; *Solid State Commun.*, **1978**, *28*, 943

[30] Wiesendanger, R.; *Scanning probe microscopy and spectroscopy: methods and applications*, **1994**, Cambridge University Press

[31] Feynman, R.P.; *"Plenty of Room at the Bottom"*, Lecture at An American Physical Society Meeting, Caltech, CA. December 29, **1959**

[32] Young, R.D.; *Phys. Today*, **1971**, *24*, 42

[33] Young, R.D., Ward, J., Scire, F.; *Rev. Sci. Instrum.*, **1972**, *43*, 999

[34] Binnig, G., Rohrer, H., Gerber, C., Weibel, E.; *Phys. Rev. Lett.*, **1982**, *49*, 57

[35] Binnig, G., Rohrer, H., Gerber, C., Weibel, E.; *Phys. Rev. Lett.*, **1983**, *50*, 120

[36] Eigler, D.M., Schweizer, E.K.; *Nature*, **1990**, *344*, 524

[37] Seitz, F., Turnbull, D. (eds.); *Tunneling in Solids. Solid State Physics*, **1969**, Academic, New York

[38] Tersoff, J., Hamann, D.R.; *Phys. Rev. B*, **1985**, *31*, 805

[39] Bardeen, J.,; *Phys. Rev. Lett.*, **1961**, *6*, 57

[40] Lang, N.D.; *Phys. Rev. Lett.*, **1986**, *56*, 1164

[41] Chen, C.J.; *Phys. Rev. Lett.*, **1990**, *65*, 448

[42] Weng, S.L., Plummer, E.W., Gustafsson, T.; *Phys. Rev. B*, **1978**, *18*, 1718

[43] Tsukada, M., Kobayashi, N., Isshiki, N., Kageshima, H.; *Surf. Sci. Rep.*, **1991**, *13*, 265

[44] Bonnell, D.A.; *Prog. Surf. Sci.*, **1998**, *57*, 187

[45] Davisson, C., Germer, H.C.; *Phys. Rev.*, **1927**, *30*, 705

Chapter 3

Instrumentation

3.1 Introduction

In this chapter, a summary of the instrumentation used in this thesis will be presented. Most of the XPS experiments and all the STM work presented in this thesis were conducted at the Christopher Ingold Laboratories, Chemistry Department, University College London (UCL). Photoemission experiments were carried out at ELETTRA Synchrotron Light Source.

As with the vast majority of modern surface science techniques in use, experiments were conducted under ultra-high vacuum (UHV) conditions corresponding to pressures of $\leq 10^{-8}$ mbar. UHV conditions are necessary to maintain clean sample surfaces. For example, considering simple kinetic theory [1] for CO (a common gaseous contaminant) at 300 K, at a pressure of 1×10^{-10} mbar monolayer saturation will occur after 7.3 hours (assuming unity sticking probability, i.e. every gas-phase/solid-surface collision results in adsorption [2]). Hence to maintain clean surfaces over typical time periods for surface science measurement, the base pressure needs to be as low as possible.

This chapter is split into two sections. In the first, the vacuum systems and workstations used are described and in the second the vacuum instruments used are discussed in further detail.

3.2 Vacuum Systems

3.2.1 XPS system

The XPS system located at Christopher Ingold Laboratories, UCL is shown in figures 3.1 and 3.2. Initially pumping down using a rotary vane pump (*Edwards*, RV3) achieves pressures of around 1×10^{-3} mbar. The main experimental chamber can then be pumped down using a water cooled diffusion pump (*Edwards*, E04) and a titanium sublimation pump (TSP, *VG Microtech*). The system base pressure is 1×10^{-10} after a 12 hr bake-out to 180°C and thorough degassing of ion gauges and filaments.

A gas line system, evacuated by a turbomolecular pump (*Pfeiffer-Balzers*, TVP170) backed by a rotary pump (*Edwards*, RV3) admits gas to the main chamber through two high precision leak valves. One valve is reserved for admitting Ar to the ion gun for sputtering, while the other is linked to five separate gas lines, meaning several gases can be admitted in quick succession.

H_2O is prepared for dosage by freeze-thaw-pump (FPT) cycles. Liquid N_2 is used to flash freeze H_2O in a flask connected to the gas line. A valve is opened and the atmosphere is pumped off. The valve is then closed and the H_2O is thawed using a warm water bath. Initially gas bubbles are seen to evolve within the liquid, and cycles are repeated until no further gas evolves.

The experimental chamber is made from non-magnetic stainless steel, 38 cm in diameter and with three levels. A pumping inlet connects the pumps to the exper-

Front view

1 Manipulator
2 Mass spectrometer
3 Gas line leak valve
4 Ion sputtering gun
5 View port
6 View port (with lamp)
7 LEED optics
8 Electron analyser
9 X-ray source
10 Gas lines
11 Ti source
12 Ion gauge
13 Titanium sublimation pump
14 Rack
15 XPS computer

Side view
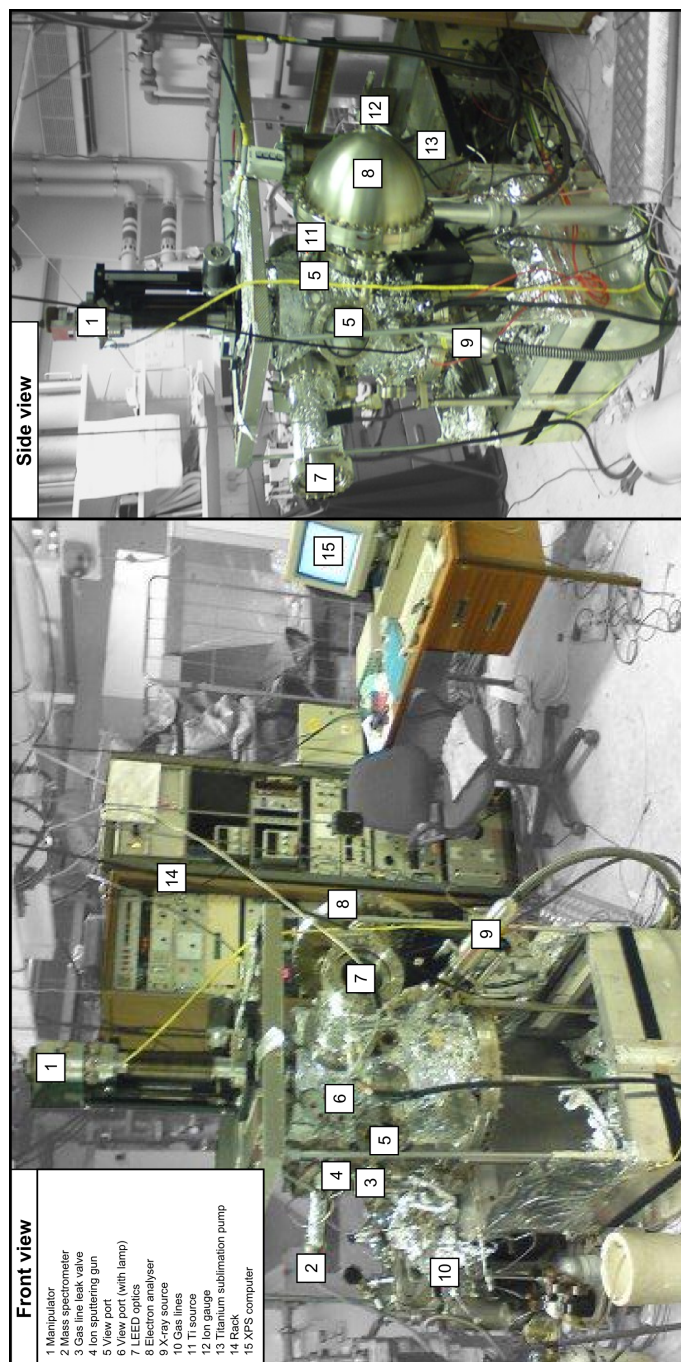
Figure 3.1: Annotated photographs of the XPS system at UCL.
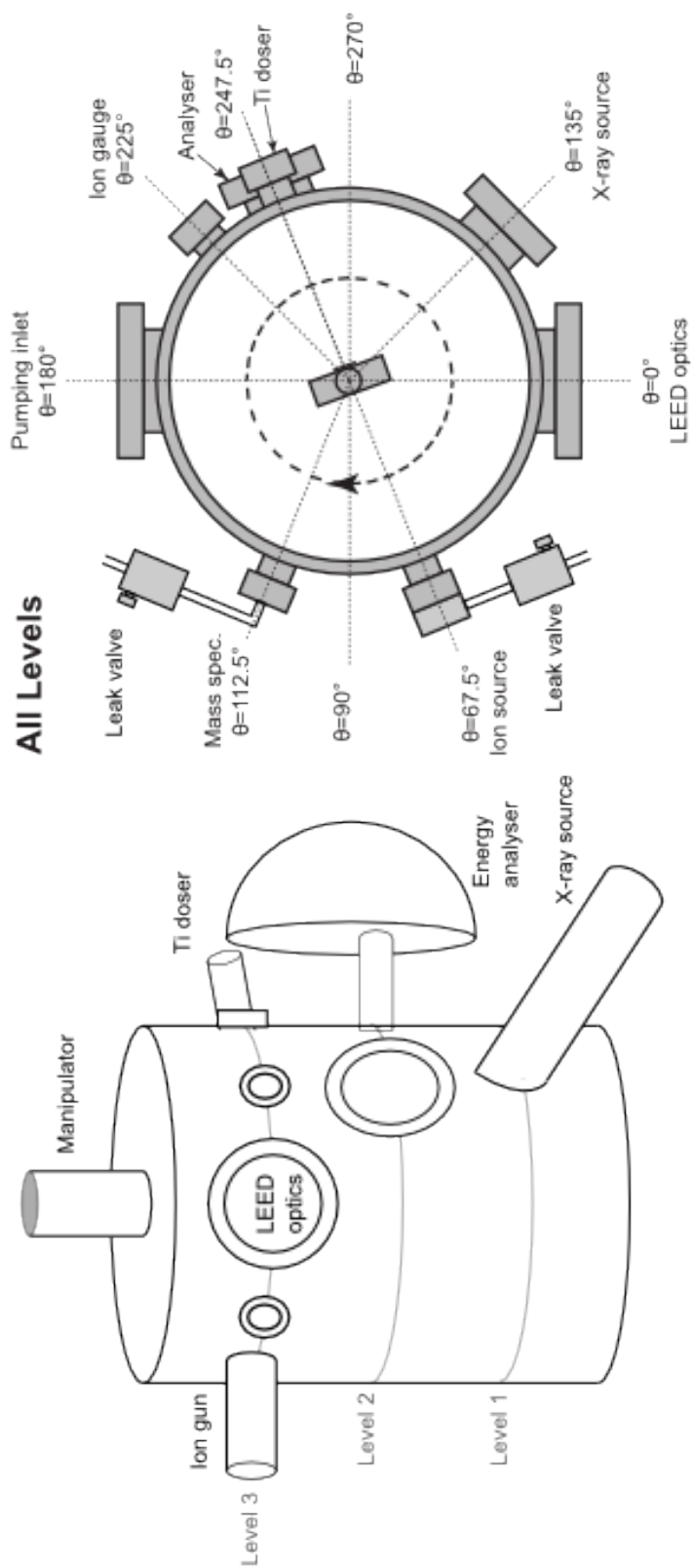
Figure 3.2: Schematic diagram and plan view showing location of instruments on the XPS system at UCL.

imental chamber at the bottom level. A valve is situated between the two and can isolate the main chamber from the pumps. Also at this level a water cooled Mg K_α ($h\nu = 1253.6$ eV) X-ray source (*VG Microtech*, XR3, see section 3.3.2 for more information) is fitted. The X-ray source is attached at a 45° angle out of plane and towards the centre of the chamber and is mounted using a linear drive mechanism, allowing the distance between X-ray source and sample surface to be optimised.

The middle level is used for XPS data acquisition. A hemispherical energy analyser is fitted (*VSW/Omicron*, EA125, see section 3.3.1 for more information). For data acquisition, samples are positioned at the centre of the level, at grazing incidence and normal emission to the analyser.

The top level of the chamber is used for sample preparation and characterisation. LEED optics (*VG Microtech*, RVL300) lie in the horizontal plane and can be used to check surface order and sample cleanliness. The LEED screen is mounted on a linear drive mechanism and so can be positioned close to the sample surface. Also on this level are an ion source (*Perkin-Elmer*, PHI 04-161, see section 3.3.4) for surface sputtering, a homebuilt metal evaporator for Ti dosing (see section 3.3.5), a quadrupole mass spectrometer (QMS, *VG*) for checking gas line purity, an ion gauge to monitor chamber pressure and several view ports.

The whole experimental setup, minus view ports, is shown in figure 3.2.

Sample Manipulation

A high precision manipulator, on which a single crystal sample is mounted, allows the sample to be moved in X, Y and Z directions and rotated through 360°. This enables the sample to be accurately and precisely positioned for XPS data acquisition. The sample crystal is mounted using a homebuilt construction (figure 3.3), to allow for the high temperatures (1500-2000 K) required to anneal W and remove its
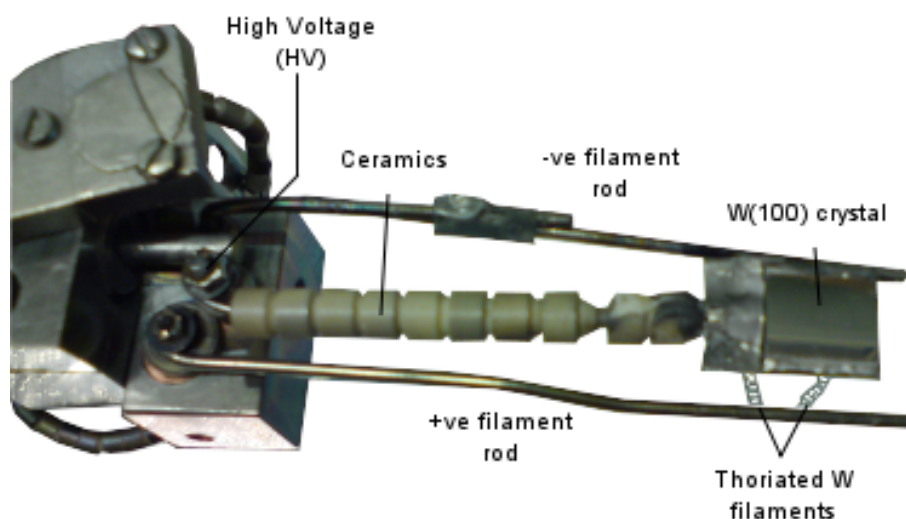
Figure 3.3: Photograph of the sample mounting in the XPS system.

contaminants (principally O and C [3]). The sample is positioned at the end of a tantalum rod sheathed by ceramics and attached using spot-welded tantalum foil. Behind the crystal, two thoriated W filaments (*Goodfellow*, 99%W/1%Th, $\phi =0.125$ mm) are suspended. For electron beam heating of the sample, a current of 0-4.2 A is applied to the filaments and a positive potential of 0.5-1.5 kV is applied to the mounted crystal. The temperature of the sample is monitored using an optical pyrometer.

3.2.2   VT-STM

The variable-temperature STM (VT-STM) is a commercial unit manufactured by *Omicron Vakuumphysik GmbH*, located at Christopher Ingold Laboratories, UCL and is shown in figure 3.4. The system is divided into three chambers, a preparation chamber, an analytical chamber and the STM chamber. The analytical and STM chambers are directly connected together, while all other sections are separated by gate valves. Samples and STM tips can be introduced into the preparation chamber via a fast entry load lock. A schematic diagram is shown in figure 3.5.

STM side view

1 LEED camera
2 LEED/AES optics
3 STM camera
4 TSP
5 Manipulator
6 Electron gun
7 STM chamber
8 Wobble stick
9 Leak valve
10 Cryostat
11 Mass spec
12 Ion gun
13 Ti doser
14 Magnetic transfer line
15 Fast-entry load lock
16 View port
17 Gas line
18 Rack
19 Vibration dampeners

Preparation chamber side view
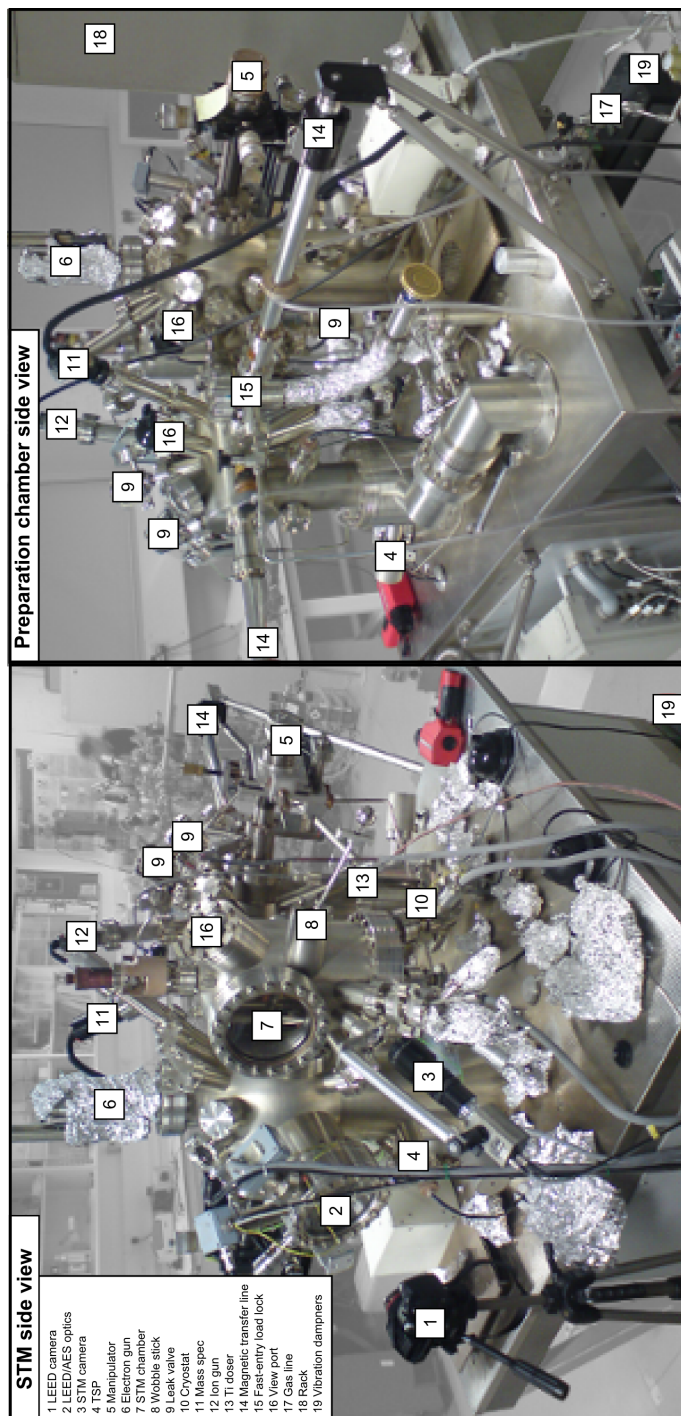
Figure 3.4: Annotated photographs of the VT–STM at UCL.
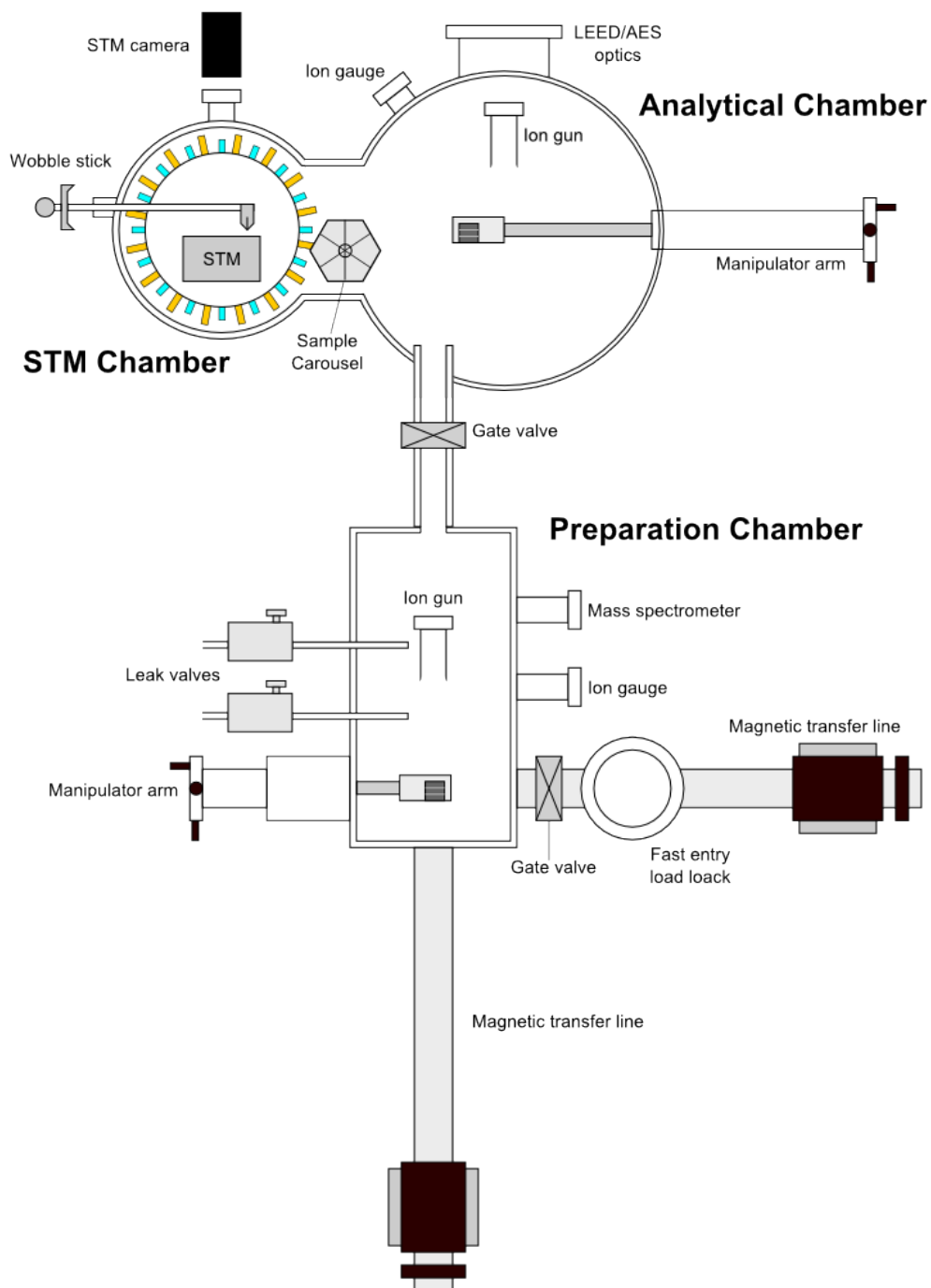
Figure 3.5: Schematic diagram of the VT-STM at UCL.

From atmospheric pressure the system is pumped down using a turbomolecular pump to a pressure of about 10^{-5} mbar. The system is then baked at around 145°C for 12-20 hours to desorb any water or hydrocarbons adsorbed to the internal surface of the chamber. Following the bake, the system pressure is around 10^{-7} mbar and ion getter pumps are switched on. These pumps are more efficient than the turbomolecular pumps and can achieve pressures below the maximum sensitivity of ion gauges (10^{-11} mbar). When the pressure reaches 1×10^{-9} mbar, the turbomolecular pump is valved off as it limits further pressure improvement. TSPs (*Omicron*) are fitted to both chambers to improve pressure following a bake, and these are activated periodically according to the chamber pressure. Using this pumping approach, base pressures are typically 10^{-10} mbar or better.

A gas line - also pumped by the turbomolecular pump - is connected to the chambers by leak valves, allowing admission of Ar and O_2 gases.

Preparation chamber

The preparation chamber is used to prepare the sample for analysis and includes instruments for ion sputtering and sample heating. Samples can be introduced to this chamber from the fast entry load lock using a magnetic transfer line. Samples are mounted using spot-welded Ta clips onto Ta plates which can be inserted into a manipulator arm. This allows X, Y, Z translational and 360° rotational positioning for ion sputtering and metal dosing, and also contains two thoriated-W filaments for e-beam heating (figure 3.6). Sample temperature is monitored using an optical pyrometer. Also attached to the preparation chamber are an ion gun (*Perkin-Elmer*, PHI 04-161, see section 3.3.4), a homebuilt Ti doser (see section 3.3.5), an ion gauge, a QMS (*VG*) and leak valves allowing the admission of Ar (*SIP Analytical*) and O_2 (*SIP Analytical*) from the gas line.
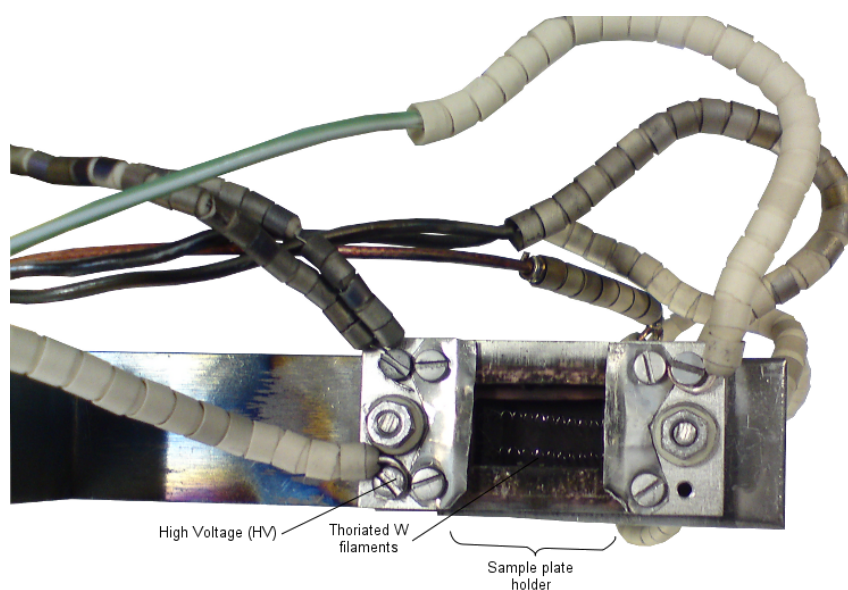
Figure 3.6: Photograph of the manipulator head used for sample heating in the VT-STM.

Analytical chamber

The analytical chamber provides facilities for sample characterisation. Samples can be introduced from the preparation chamber via a magnetic transfer line and placed in a second manipulator head (as in the preparation chamber). An electron gun (not used in these experiments), a second ion gun (*Perkin-Elmer*, PHI 04-161), a retarding field analyser (RFA) for LEED and Auger electron spectroscopy (AES) (*Omicron*, see section 3.3.3) and a leak valve to the gas line are also attached.

STM chamber

The STM chamber is directly connected to the analytical chamber, and samples can be transferred from the manipulator head to the STM stage using a wobble stick. A sample carousel is located between the STM and analytical chambers, allowing up to 6 samples and/or STM tips to be parked. The STM is a commercial unit manu-
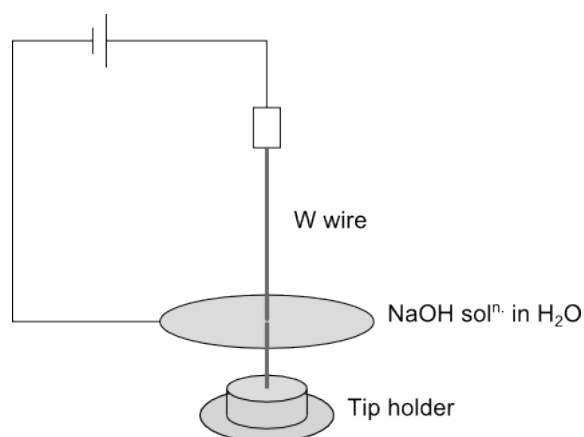
Figure 3.7: Schematic diagram of tip fabrication by electrochemical etching.

factured by *Omicron Vakuumphysik GmbH*. A cooling system allows measurement temperatures of 25-1200 K (hence variable temperature), however all measurements presented in this thesis were recorded at room temperature. The STM stage is suspended on springs and positioned at the centre of eddy-current damping systems to minimise vibrational interference. To further reduce the effects of vibrations, the chamber is mounted on Viton® stacks.

Tip preparation

The ideal STM tip should be terminated by a single known atom. In reality, no such method exists to characterise such a tip. However, tips judged to be macroscopically sharp and symmetric by optical microscopes are known to be suitable for STM imaging. In experiments presented here, tungsten wire (*Goodfellow*, 99.9%, ϕ=0.38 mm) is used as the tip material. Tungsten is widely used for STM tips owing to its hardness.

Tips are prepared by electrochemical etching (figure 3.7). A length of W wire is mounted onto a tip holder by spot welding. The wire is clamped such that it passes through a stainless steel O-ring which forms part of a circuit. When a solution of aqueous NaOH is suspended in the O-ring by surface tension, it acts as a cathode,

and the W wire acts as the anode. As such, the W wire is etched at the electrolyte-air interface. During etching, gravity pulls the tip holder down which elongates the neck formation, resulting in sharper tips. When etching is complete and the tip drops off, it is washed thoroughly in distilled water. On introduction to UHV, it is further cleaned and degassed overnight at ∼400 K.

3.2.3 Materials Science Beamline at Elettra

The Materials Science beamline (MSB) at ELETTRA Sincrotrone, Trieste was used in RESPES measurements.

ELETTRA Light Source

Synchrotron radiation is light emitted when electrons moving at relativistic velocities are accelerated [5]. At ELETTRA, most radiation is obtained when electrons are constrained to a near-circular trajectory with bending magnets. Its storage ring consists of 12 identical groups of magnets forming a ring roughly 260 m in circumference (figure 3.8). Electrons are generated in a linear particle accelerator (LINAC) by heating a ceramic disc to a very high temperature and then injected into the ring. Electrons are drawn out using an electric field and then accelerated through various
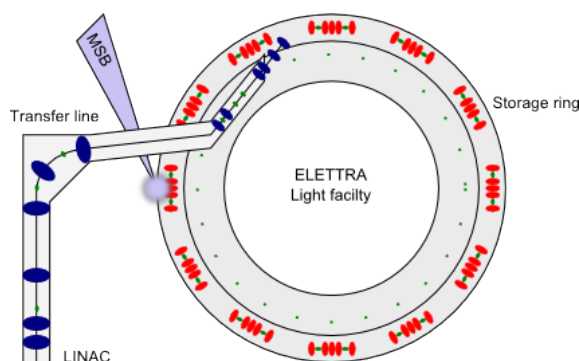
Figure 3.8: Schematic diagram of the ELETTRA storage ring.
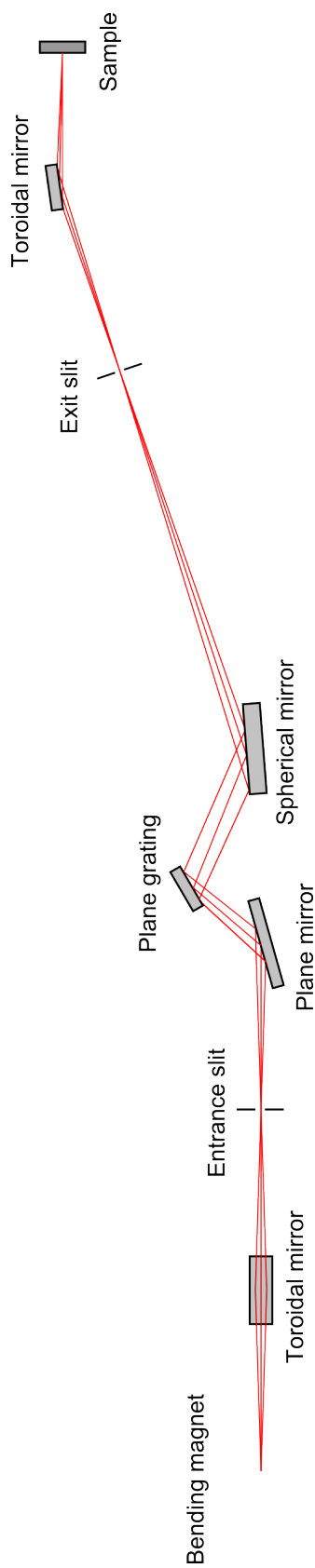
Figure 3.9: Schematic diagram of the optical layout of the Materials Science Beamline at ELETTRA. Not to scale.

radio-frequency structures that make up the LINAC. Pulses of electron bunches are generated and accelerated to a final energy of up to 1.2 GeV. The LINAC is at vacuum to minimise electron loss through collision with gas molecules. Electrons are transferred to the storage ring via the transfer line.

Beamline

The MSB is attached to bending magnet 6.1 at ELETTRA with a photon energy range of 20-800 eV [6]. Given that HeI lamps used for ultra-violet spectroscopy (UPS) have a photon energy of $h\nu = 21.1$ eV and standard XPS photon sources are typically $h\nu = 1253.6$ eV ($\mathrm{Mg}K_\alpha$) and $h\nu = 1486.6$ eV ($\mathrm{Al}K_\alpha$), the beamline provides a tunable synchrotron light source that bridges the gap between the two techniques. The photon flux at the sample varies, from 3×10^8 photons/s at 500 eV to 3×10^{10} at 1000 eV at a resolving power of 2000, and ring current of 100 mA [6,7]. The optical layout of the beamline is shown schematically in figure 3.9 [8]. The first optical element is a toroidal mirror which focuses light onto the entrance slit. Light then reaches the monochromator, which consists of three optical elements: a plane mirror, plane grating and spherical mirror. The plane mirror can be rotated and the plane grating rotated and translated to focus light onto the exit slit. Finally, another toroidal mirror reflects the light onto the sample in the experimental chamber.

Experimental Chamber

A plan view of the experimental chamber showing the relative positions of equipment and the beam is shown in figure 3.10. The chamber is equipped with a high luminosity energy analyser (*Specs PHOIBOS*, 150 mm radius, 9 channels), a fast entry lock, LEED, an ion gun, He lamp for UPS (not used in these experiments), a dual $\mathrm{Al}K_\alpha/\mathrm{Mg}K_\alpha$ source X-ray source, a gas inlet, a mass spectrometer, metal evaporators (Pd and Ce) and sample heating and cooling.
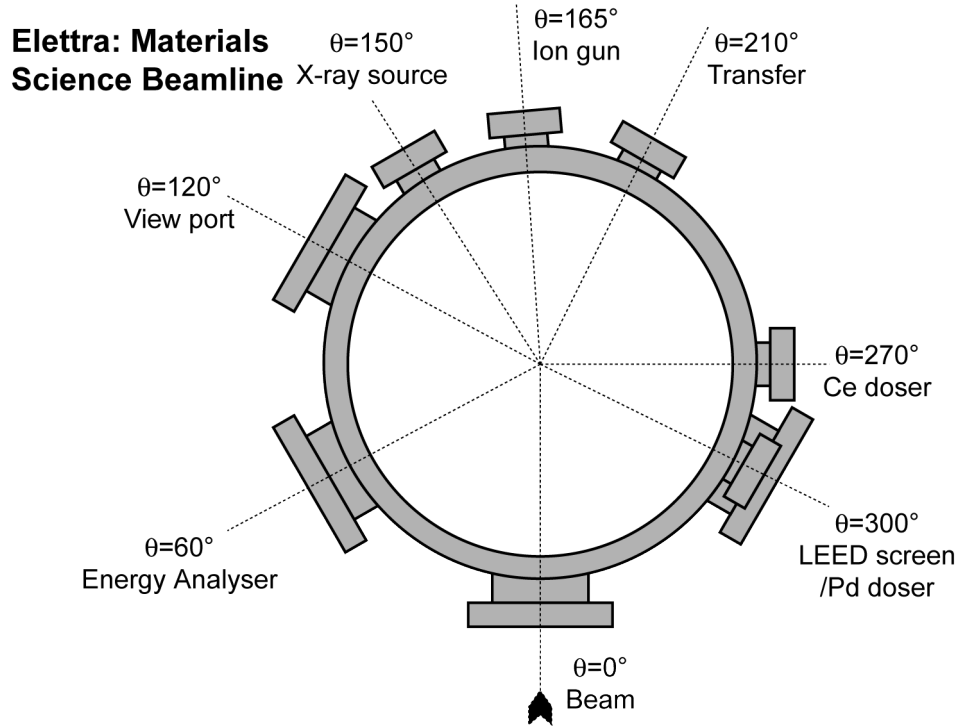
Figure 3.10: Diagram of the top view of the MSB experimental chamber and location of equipment.

3.3 Instruments

3.3.1 Energy Analyser

As discussed in chapter 2, incident radiation of wavelength $h\nu$ can eject electrons from a bound state of energy E_B with a true kinetic energy of E_K':

$$E_K' = h\nu - E_B - \phi_s \qquad (3.1)$$

where ϕ_s is the workfunction of the sample. The real energy distribution has a low energy cut-off of $E_K' = \phi_s$. Below this energy, electrons have insufficient energy to overcome the workfunction. The high energy cut-off occurs when electrons are ejected from the Fermi level, where E_B is defined as zero (i.e. $E_K' = h\nu - \phi_s$). The true kinetic energy scale cannot be directly measured because ϕ_s is not known. Only
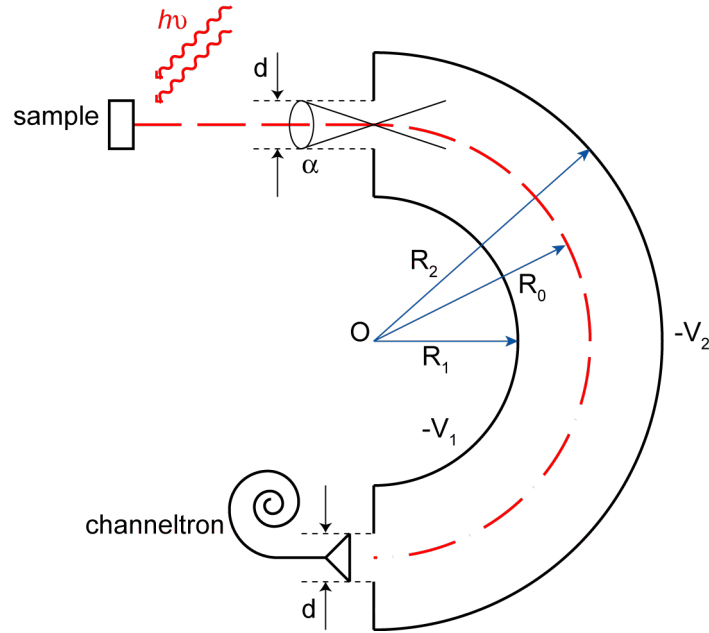
Figure 3.11: Schematic diagram of a hemispherical energy analyser. d is the entrance and exit slit width, α the half angle of acceptance, and R_1 and R_2 are the inner and outer radii with R_0 as the mean radius, all with a common origin, O.

by calibration can $(E'_K + \phi_s)$ be determined.

However, the offset of the spectrum by ϕ_s is not as significant as might be expected. Ejected electrons are focused by a lens element and retarded by an amount $\mathbf{R}$ (as determined by lens voltages) before entering the analyser. The analyser is a band pass filter only transmitting electrons with energies at or close to the pass energy, E_P. Transmitted electrons are stopped by a detector. The measured kinetic energy of the electrons is therefore $\mathbf{R}+E_P$. However, the analyser also has a workfunction, ϕ_a meaning the kinetic energy of detected electrons becomes:

$$E_K = \mathbf{R} + E_P + \phi_a = h\nu - E_B \tag{3.2}$$

Equation 3.2 is independent of ϕ_s.

Hemispherical energy analysers consist of two concentric hemispheres of radius R_1 and R_2, and R_0 is the mean radius between the two, all with a common centre,

O (figure 3.11). A potential is applied to both hemispheres, such that the outer sphere, $-V_2$ is negative and the inner sphere, $-V_1$ is positive with respect to $-V_0$, the median potential surface of radius R_0. Entry and exit slits to the analyser are centred on R_0 at either end of the hemisphere.

If the pass energy, E_P, is the energy of an electron travelling in the mean orbit of radius R_0, then the relationship between E_P and V_0 is given by:

$$eV_0 = V_2 - V_1 = E_P \cdot \left(\frac{R_2}{R_1} - \frac{R_1}{R_2} \right) \tag{3.3}$$

The potentials of the inner, V_1 and outer, V_2 hemispheres are given by:

$$V_1 = E_P \cdot \left(2\frac{R_0}{R_1} - 1 \right) \tag{3.4}$$

$$V_2 = E_P \cdot \left(2\frac{R_0}{R_2} - 1 \right) \tag{3.5}$$

Energy analysers can be operated in two modes, fixed analyser transmission (FAT) or fixed retarding ratio (FRR) - alternatively called constant analyser energy (CAE) and constant retard ratio (CRR), respectively. In FAT mode the pass energy, E_P is held constant and the entrance lens applies a variable retarding voltage on detected electrons, such that only those electrons matching E_P will be deflected through the hemisphere and be detected. By ramping the retard voltage of the entrance lens, a full spectrum of kinetic energies can be recorded. In FRR mode, electrons entering the analyser are retarded by a constant proportion of their kinetic energy so that the ratio of electron E_K to analyser E_P is kept constant. All measurements presented in this thesis were taken in FAT mode since it provides fixed resolution at all E_K in the range 150-2000 eV, whereas FRR mode is more commonly used for investigating

lower E_K, below 150 eV (e.g. for AES).

The relative energy resolution, R is given by a relation between the absolute resolution, ΔE - usually measured as the full width at half-maximum height (FWHM) of an observed peak - and E_P:

$$R = \Delta E / E_P \tag{3.6}$$

Hence, at lower pass energies the spectral resolution will be higher. However, since signal intensity is proportional to pass energy, measurements taken at low pass energy will be less intense. In experiments presented here, high pass energies (typically 60-100 eV) are used for recording wide scans (E_k=100-1260 eV), and lower pass energies (≤ 40eV) for narrow bands of E_k values around peaks of interest [4, 9–11].

3.3.2 X-ray source

X-ray sources are required as a source of photons for XPS experiments. The most common sources use Mg or Al anodes, or a combination of both. The photon energy is characteristic of the material used with $h\nu = 1253.6$ eV for Mg K_α and $h\nu = 1486.6$ eV for Al K_α.

X-ray sources comprise a central anode with a filament mounted concentrically around it, protected by an outer shield. A potential of 11 kV is applied to the anode (which is water cooled to prevent overheating), and when a current - typically 4.5 A in these experiments - passes through the filament, electrons are emitted and accelerated towards the anode. These highly energetic electrons cause the emission of X-ray lines of characteristic energy from the anode source. An aluminium foil window mounted in the outer shield filters out unwanted X-ray lines and stray electrons. The range of photon energies from the anode is dominated by core level

transitions such as the $2p \to 1s$ transition, termed K_{α}. However, the source is not monochromatic, also consisting of so-called Bremmsstrahlung background radiation and a series of lower intensity lines, known as X-ray satellites. The $2p_{3/2} \to 1s$ and $2p_{1/2} \to 1s$ are denoted $K_{\alpha 1}$ and $K_{\alpha 2}$ respectively. Satellites are caused by less common transitions such as valence band$\to 1s$ (K_{β}) or transitions from multiply ionised atoms ($K_{\alpha 3,4}$).

3.3.3 LEED/AES Optics

In experiments presented here, both LEED and AES were used qualitatively for checking surface long-range order and contamination, respectively. On the XPS system, the LEED unit (*VG Microtech*) was used exclusively for LEED whilst on the VT-STM, the optics and electron gun (*Omicron*) were used for both LEED and AES. The optics are shown in figure 3.12 operating in (a) LEED and (b) AES modes.

In LEED mode, an electron gun is used to direct a beam of electrons in the energy range 20-200 eV at the sample surface. The energy spread of these electrons is of the order of 0.5 eV resulting in finite dimensions of diffracted spots. The optics consist of 3 (*VG Microtech*) or 4 (*Omicron*) meshes and a phosphor coated screen. The first and last grids are earthed, as is the sample. A bias roughly equal to the potential of the electron source is applied to the middle mesh/es to retard any inelastically scattered electrons. Elastically scattered electrons are directed to the screen, which is held at positive bias (+5-7 kV) and illuminate spots of a diffraction pattern if the surface is ordered.

In AES mode, the electron gun is used to produce an electron beam of higher energy (3 keV). The LEED optics are used as a retarding field analyser (RFA), which employs a modulating voltage of 5 V. The phase sensitive signal is detected using a lock-in amplifier. This also enables spectra to be recorded in derivative mode, which enhances peaks.
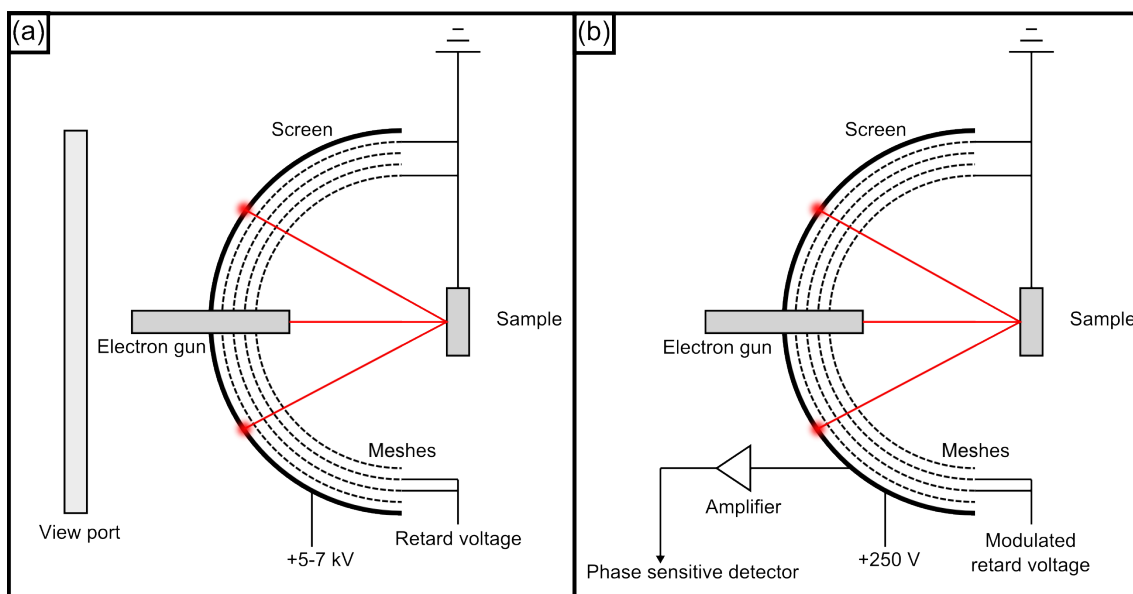
Figure 3.12: Schematic diagram showing the LEED/AES optics in (a) LEED mode and (b) RFA AES mode.

3.3.4 Ion Source

The ion source is used to clean the sample surface. Argon (*SIP Analytical*) is admitted to the chamber to a pressure of 5×10^{-5} mbar. A hot filament in the ion source is used to ionise the gas. Ar^+ ions are accelerated with a potential of 1500 V, focused using electrostatic lenses into a beam and directed onto the sample (typical spot size of 10 mm). To ensure the beam is directed at the surface, the drain current can be measured by placing a multimeter between the sample and ground (typical drain currents of $10\mu A$). Accelerated Ar^+ ions strike the surface and knock out atoms, and so remove surface contaminants. Bombardment results in a disordered, "pitted" surface and can also cause embedding of Ar into the substrate. For this reason samples are annealed following periods of sputtering.
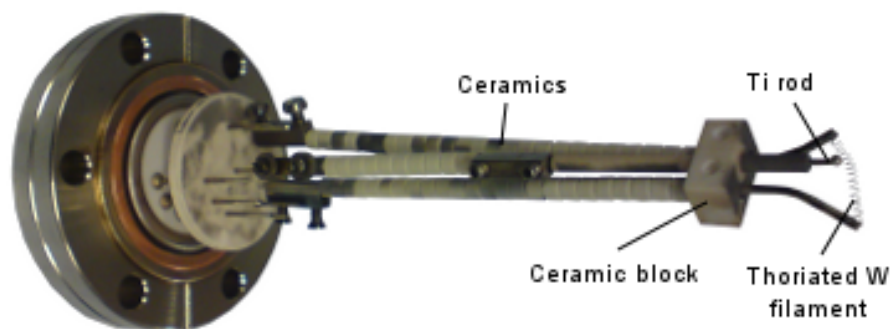
Figure 3.13: Photograph of a homebuilt Ti doser.

3.3.5 Metal Evaporators

Metal deposition is achieved using homebuilt e-beam metal evaporators. Ti and Pd dosers were constructed in an identical manner. On an electrical feedthrough, a Ti rod (*Goodfellow*, 99.99+%, ϕ =1.0 mm) or Pd rod (*Goodfellow*, 99.99+%, ϕ =1.0 mm) is mounted in front of a thoriated-W filament (*Goodfellow*, 99%W/1%Th, ϕ =0.125 mm). The distance between the metal rod and the filament is small (~ 5 mm). A high voltage, V is applied to the metal and a current, I_{fil} passed through the filament. Typical settings are $V = 0.6 - 1$ kV and $I_{fil} = 1.8 - 2.1$ A, resulting in an emission current, I_{em}, typically $I_{em} = 5 - 20$ mA. Electrons emitted from the filament strike the metal rod, heating it and causing it to sublime. Sublimated metal atoms leave the tip of the rod and travel through the vacuum. The substrate must be angled such that it is facing the metal rod for evaporated metal to reach its surface.

A cerium doser was constructed in a similar fashion except that a tantalum crucible was used to house a piece of cerium foil. The crucible was biased in the same way and passing a current through the filament caused Ce to be heated and sublime in the same way as for Ti and Pd.

References

[1] Atkins, P.W., de Paula, J.; *Atkins' Physical Chemistry, 7th Ed.*, **2002**, Oxford University Press

[2] Chambers, A., Fitch, R.K, Halliday, B.S.; *Basic Vacuum Technology*, **1998**, Taylor & Francis

[3] Grunze, M., Ruppender, H, Elshazly, O.; *J. Vac. Sci. Technol. A*, **1988**, *6(3)*, 1266

[4] Briggs, D., Seah, M.P., Eds.; *Practical Surface Analysis by Auger and X-ray Photoelectron Spectroscopy*, **1983**, John Wiley & Sons Ltd.

[5] Bachrach, R.Z. (Ed.); *Synchrotron Radiation Research: Advances in Surface and Interface Science, Vol. 1: Techniques*, **1992**, Plenum Press, New York

[6] Vašina, R., Kolaříka, V., Doležel, P., Mynář, M., Vondráček, Cháb, V., Slezák, J., Comicioli, C., Prince, K.C.; *Nucl. Instrum. Meth. A*, **2001**, *467-8*, 561

[7] ELETTRA - BL 6.1 - Materials Science Beamline, `http://www.elettra.trieste.it/experiments/beamlines/ms/index.html`

[8] Vondráček, M., Cháb, V., Matolín, V., Prince, K.C.; *Czech and Slovak Crystallographic Association and Regional Committee of the IUCr*, **2008**, `http://www.xray.cz/xray/csca/kol2008/abst/vondracek.htm`

[9] Kuyatt, C.E., Simpson, J.A.; *Rev. Sci. Instr.*, **1967**, *38*, 103

[10] Walls, J.M., Ed.; *Methods of Surface Analysis*, **1989**, University Press, Cambridge, UK

[11] Watts, J.F.; *An Introduction to Surface Analysis by Electron Spectroscopy*, **1990**, Oxford University Press

Chapter 4

Reduction of thin-film ceria on Pt(111) by supported Pd nanoparticles probed with resonant photoemission

4.1 Introduction

4.1.1 Ceria in Technology

Cerium dioxide is a technologically important material that is used in catalytic, mechanical, electronic, optical, thermal and chemical applications. Nearly all applications of cerium-based materials are related to the potential redox chemistry involving $Ce^{3+} \leftrightarrow Ce^{4+} + e^-$ which has a relatively low activation energy, as well as the high affinity of Ce for oxygen and sulphur. One of the most important applications of ceria is in three-way catalysts (TWCs) found on modern automobile

exhausts [1]. TWCs are designed to simultaneously convert CO, NO$_x$ and unburnt hydrocarbons to CO$_2$, N$_2$ and H$_2$O [2]. This is possible since ceria can release and absorb oxygen in a reversible reaction:

$$CeO_2 \rightleftharpoons CeO_{2-x} + (x/2)O_2 \qquad\qquad (i)$$
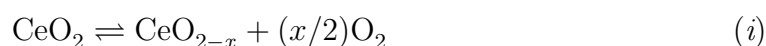
This oxygen storage capacity (OSC) is useful in controlling the air/fuel ratio and attaining a high conversion efficiency of pollutants such as CO, NO$_x$ and unburnt hydrocarbons. In order to maintain overall efficiency of the TWC, support materials must be able to store oxygen under conditions of excess O$_2$ and release it under conditions of excess fuel in the exhaust gas [3, 4]. TWCs are efficient even under oscillatory conditions found in the course of normal driving, due to the reversible reaction:

$$CeO_2 + xCO \rightleftharpoons CeO_{2-x} + xCO_2 \qquad\qquad (ii)$$

The addition of noble metals activates redox sites of ceria and allows very high oxygen storage even at low temperature [5–9].

4.1.2   Structure and non-stoichiometry of ceria

Ce with the outer electronic configuration [Xe] $4f^2 5d^0 6s^2$ can take both +3 and +4 oxidation states. This means mixed valence cerium oxides in the composition range Ce$_2$O$_3$-CeO$_2$ can form. Cerium metal is unstable in the presence of O$_2$ and readily forms both Ce$_2$O$_3$ and CeO$_2$. However, the final stoichiometry is temperature and O$_2$ pressure dependent resulting in mixed valency ceria CeO$_{2-x}$.

Ceria can be reduced by the removal of O^{2-} ions from the crystal lattice, which

creates an anion vacancy site [10]:

$$4\text{Ce}^{4+} + \text{O}^{2-} \rightarrow 4\text{Ce}^{4+} + 2e^-/\square + \frac{1}{2}\text{O}_2 \rightarrow 2\text{Ce}^{4+} + 2\text{Ce}^{3+} + \square + \frac{1}{2}\text{O}_2 \qquad (iii)$$
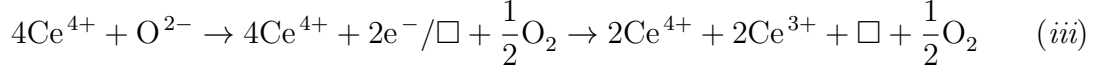
where $\square$ represents an anion vacancy site. The reduction of Ce^{4+} to Ce^{3+} enables overall electrostatic balance to be maintained. By the elevating temperature and/or lowering $p(\text{O}_2)$ a seemingly continuum of oxygen-deficient CeO$_{2\text{-}x}$ can be formed.

Intrinsic defects may arise in the ceria surface due to thermal disorder or reaction between the solid and the surrounding atmosphere. There are three possible pathways for the generation of intrinsic disorder in ceria that do not involve gas-phase exchange:

$$\text{Ce}_{\text{Ce}} + 2\text{O}_{\text{O}} \leftrightarrow V_{\text{Ce}}'''' + 2V_{\ddot{\text{O}}} + \text{CeO}_2 \qquad \Delta E = 3.53\text{eV} \qquad (iv)$$

$$\text{Ce}_{\text{Ce}} \leftrightarrow \text{Ce}_{\text{i}}^{\cdots\cdot} + V_{\text{Ce}}'''' \qquad \Delta E = 11.11\text{eV} \qquad (v)$$

$$\text{O}_{\text{O}} \leftrightarrow \text{O}_{\text{i}}'' + V_{\ddot{\text{O}}} \qquad \Delta E = 3.20\text{eV} \qquad (vi)$$
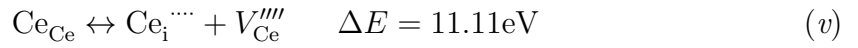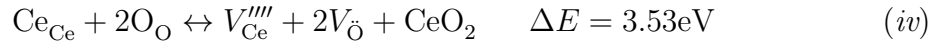
In the Kröger-Vink defect notation [11] used in the above reactions, V represents a vacancy, $\cdot$ a positive charge and $'$ a negative charge. Ce$_{\text{Ce}}$ and O$_{\text{O}}$ represent cerium and oxygen in their respective lattice sites, V_{Ce}'''' and $V_{\ddot{\text{O}}}$ represent cerium and oxygen vacancies respectively, and Ce$_{\text{i}}^{\cdots\cdot}$ and O$_{\text{i}}''$ represent cerium and oxygen interstitials respectively. Comparing ΔE values [12], reaction (vi) produces the dominant defect state, $V_{\ddot{\text{O}}}$ [13]. Generally, these defects are only present in low concentrations and do not cause non-stoichiometry. However, higher concentrations can be produced by exposing ceria surfaces to reducing gases. Reduction causes the cation/anion

ratio to increase > 0.5 (i.e. excess metal to anion content). There are two ways to compensate for the change in composition. Firstly, oxygen vacancies can be assumed to compensate holes formed on reduction. Removing O^{2-} from the crystal lattice results in an overall positive charge, and $2e^-$ need to be introduced for every O^{2-} removed. These $2e^-$ are associated with two cerium atoms that are reduced from a 4+ state to a 3+ state, thus maintaining overall neutrality of the crystal. This process is illustrated in reaction (i) where $x < 0.5$, or using defect notation:

$$\text{CeO}_2 \leftrightarrow 2x\text{Ce}_{\text{Ce}}{}' + (1 - 2x)\text{Ce}_{\text{Ce}} + x V_{\ddot{\text{O}}} + (2 - x)\text{O}_{\text{O}} + \frac{x}{2}\text{O}_{2\,(\text{g})} \qquad (vii)$$
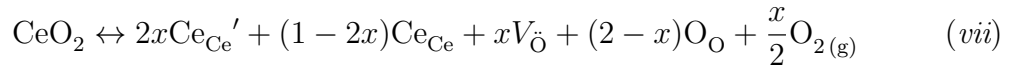
The presence of $V_{\ddot{\text{O}}}$ in the crystal lattice is shown in schematically in figure 4.1(a).

Alternatively, the creation of cation interstitials can create positively charged defects. These may be formed by the transfer of Ce cations at the surface to an interstitial position, accompanied by the removal of two anions to the gas phase for each Ce_{i} formed:

$$(1 + x)\text{CeO}_2 \leftrightarrow \text{Ce}_{1+x}\text{O}_2 + x\text{O}_{2\,(\text{g})} \qquad (viii)$$

when $x < 0.33$. However, reaction ($viii$) does not reveal where the e^- are localised. Several possibilities exist, as explained more satisfactorily using defect notation:

$$(1 + x)\text{CeO}_2 \leftrightarrow x\text{Ce}_{\text{i}}{}^{\cdots} + 3x\text{Ce}_{\text{Ce}}{}' + (1 - 3x)\text{Ce}_{\text{Ce}} + 2\text{O}_{\text{O}} + x\text{O}_{2\,(\text{g})} \qquad (ix)$$

$$(1 + x)\text{CeO}_2 \leftrightarrow x\text{Ce}_{\text{i}}{}^{\cdots\cdot} + 4x\text{Ce}_{\text{Ce}}{}' + (1 - 4x)\text{Ce}_{\text{Ce}} + 2\text{O}_{\text{O}} + x\text{O}_{2\,(\text{g})} \qquad (x)$$
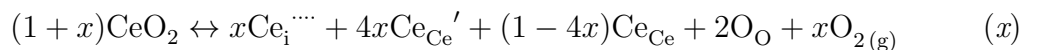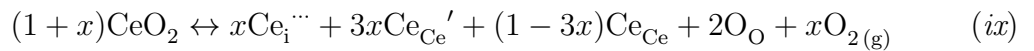
The presence of a $\text{Ce}_{\text{i}}{}^{\cdots\cdot}$ interstitial (reaction (x)) in the crystal lattice is shown

schematically in figure 4.1(b).

The OSC of ceria can be improved by the addition of a suitable metal (such as Rh [14, 15], Pd [15, 17, 18], Pt [19], Sn [20, 21], Au [22] and Gd [23]). However, despite extensive investigation, detailed mechanistic insight into the operation of this catalyst is lacking.

When deposited on ceria surfaces, Pd forms nanoparticles [18], providing a large surface area for catalysis with low coverages, which has a clear economical benefit. Pd/CeO_2 systems have been shown to catalyse methanol synthesis [24] and the water-gas shift (WGS) reaction [25, 26]. Additionally, Pd is an important additive to TWCs - CO readily adsorbs molecularly to Pd whilst ceria provides the oxygen required for oxidation and activates the Pd so that the adsorption is partially dissociative. The presence of Pd on the ceria surface alters the stoichiometry and can introduce oxygen vacancies [17].

4.1.3   Ceria thin films

The CeO_2 band gap of 3.2 eV prevents the study of single crystals at least at room temperature and below. Thus, the work described above has been conducted by using ultrathin single crystalline films of ceria, to allow the use of electron based spectroscopies. Films can be grown on a variety of single crystal metal substrates such as Pt(111) [27–30], Rh(111) [31], Re(0001) [32], Cu(111) [33], Ru(0001) [34], Ni(111) [34] and Pd(111) [35]. The non-stoichiometry of ceria surfaces is determined by the temperature and the pressure of O_2. Growth on Pt(111) is a well established technique, and it has been shown by STM that ceria grows as multi-layered islands on the Pt(111) surface [36]. Pd deposition occurs preferentially on islands of ceria, forming nanoparticles [18].
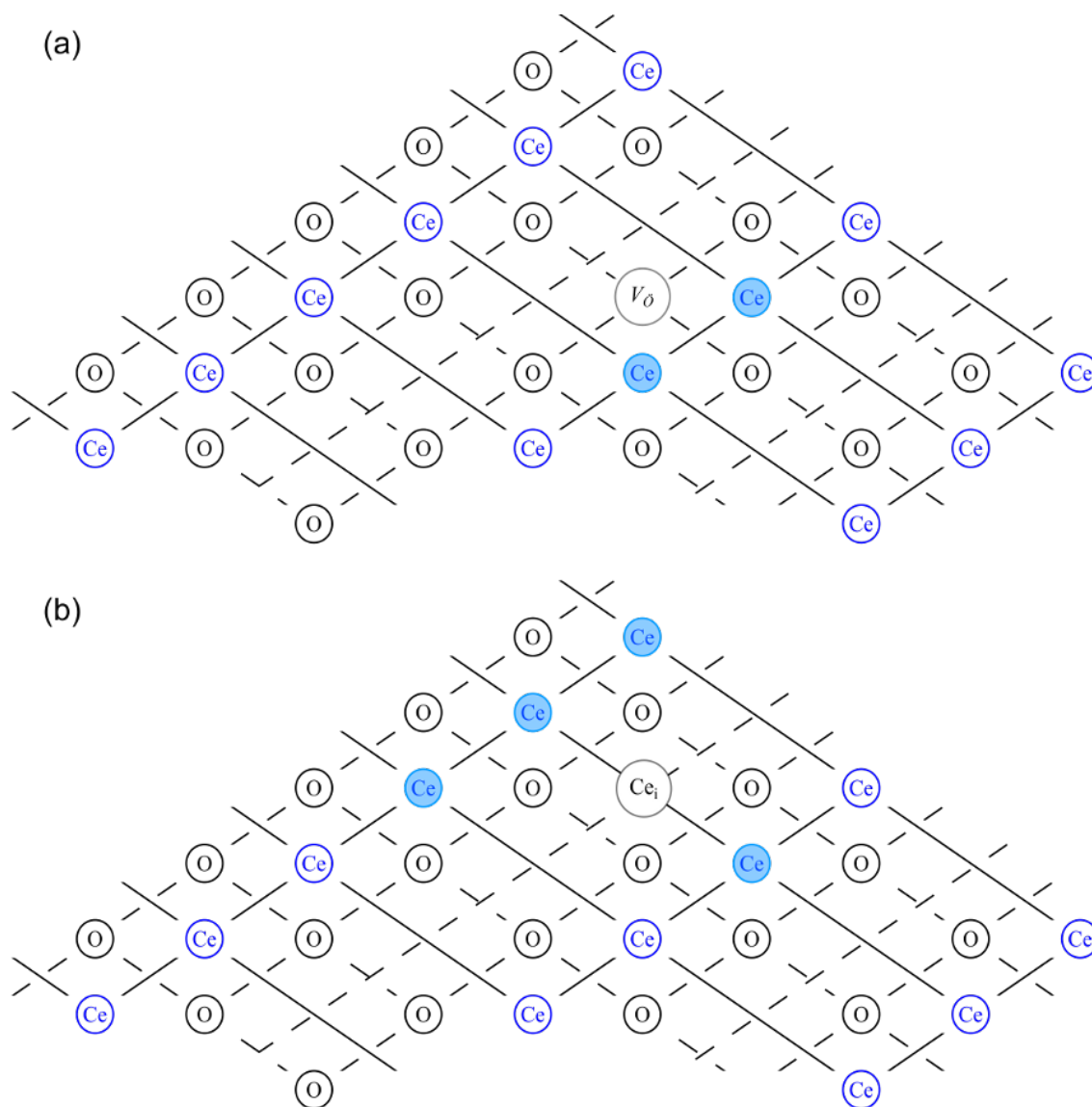
Figure 4.1: Schematic diagram showing (a) an oxygen vacancy($V_{\ddot{O}}$) and (b) a quadruply ionised cerium interstitial (Ce$_i$) in a reduced CeO$_2$ surface. Reduced Ce^{3+} cations are indicated by light blue shading.

$3d_{3/2}$	$3d_{5/2}$	Ox. state	Electronic configuration
v_O	u_O	Ce^{3+}	Mixture of $4f^2$ O $2p^5$ and $4f^1$ O $2p^6$
v	u	Ce^{4+}	Mixture of $4f^2$ O $2p^4$ and $4f^1$ O $2p^5$
v'	u'	Ce^{3+}	Mixture of $4f^2$ O $2p^5$ and $4f^1$ O $2p^6$
v''	u''	Ce^{4+}	Mixture of $4f^2$ O $2p^4$ and $4f^1$ O $2p^5$
v'''	u'''	Ce^{4+}	$4f^0$ O $2p^6$

Table 4.1: Table of Ce $3d$ satellites first described by Burroughs et al [37].

4.1.4 Measuring Stoichiometry

XPS of the Ce $3d$ region

X-ray photoelectron spectroscopy has been widely used to probe the Ce $3d$ region [37, 38]. Cerium in its elemental state shows a doublet in the $3d$ region with peaks at binding energies of 883.8 and 902.4 eV [39]. In oxides, there is interaction with oxygen which complicates the $3d$ region. In stoichiometric CeO$_2$, all cerium atoms are in the Ce^{4+} state with an unoccupied $4f^0$ configuration. Hybridisation of Ce $4f$ and O $2p$ orbitals gives rise to three possible final state electronic configurations, $4f^2$ O $2p^4$, $4f^1$ O $2p^5$ and $4f^0$ O $2p^6$ (the $5d$ and $6s$ orbitals being vacant). Notation for Ce $3d$ spectral features established by Burroughs et al [37] terms peaks arising from these configurations as v, v'', v''' (from Ce $3d_{5/2}$), u, u'' and u''' (from Ce $3d_{3/2}$). In Ce$_2$O$_3$ the cerium atoms are all Ce^{3+}, the outer electronic configuration is $4f^1$, and the energy required to transfer an electron from the O $2p$ band to the $4f$ state significantly exceeds the hybridisation energy. This results in only two possible final state electronic configurations, $4f^2$ O $2p^5$ and $4f^1$ O $2p^6$ with the peaks arising from them termed v_o, v' (from Ce $3d_{5/2}$), u_o and u' (from Ce $3d_{3/2}$). A Ce $3d$ XPS spectrum of reduced ceria, CeO$_{2-x}$ therefore consists of 5 doublet peaks - 3 arising from Ce^{4+} and 2 from Ce^{3+}. Deconvolution of the spectrum provides an estimation of the stoichiometry of the ceria. Whilst this approach has been widely used, it is not straightforward as it requires fitting of a number of overlapping peaks.

Previous studies by the Thornton group using XPS of the Ce 3d region [18] showed an increase in Ce^{3+} concentration on deposition of Pd onto CeO$_{2-x}$ films grown on Pt(111). Skála et al [17] also showed that the addition of Pd to a ceria ultrathin film grown on a Cu(111) substrate results in the creation of reduced Ce^{3+} states. In only one case, Pd deposition was reported to have had no effect on CeO$_{2-x}$ stoichiometry [15].

RESPES of the valence band

Whilst XPS has been used extensively in estimating ceria stoichiometry, results must be treated carefully. It has been shown by comparison with X-ray absorption near edge structure (XANES) that values of %Ce^{3+} are significantly larger when estimated by XPS, possibly due to depth dependence or surface reduction of ceria by photons [16]. Resonance photoemission spectroscopy (RESPES) is an alternative approach to determining the stoichiometry of ceria. This technique allows the separation of Ce 4f states from other contributions, is more surface sensitive and does not require complicated fitting analyses. When the incident photon energy matches specific resonant energies, electrons can be promoted from Ce 3d or 4d orbitals to the Ce 4f state. This manifests itself as a resonant peak in valence band spectra. Using constant intial state (CIS) scanning, the photon energy is varied over a range while scanning over a fixed binding energy range. This reveals separate resonant peaks for Ce^{3+} and Ce^{4+} at $h\nu$ =121 eV and $h\nu$ =124.5 eV respectively for the 4d-4f transition. By subtracting a suitable off-resonance scan, the heights of these resonant peaks, D can be determined, and the ratio DCe^{3+}/DCe^{4+} gives an indication of the stoichiometry of the ceria [17, 20–23, 40–42]. The inelastic mean free path (IMFP) of an ejected cerium electron with a kinetic energy of 119.6 eV (corresponding to the Ce^{3+} peak at 1.5 eV using photon energy of 121.1 eV) is 6 Å, whereas with a kinetic energy of 569.6 eV (u''' peak using Al K_α) the IMFP is 14 Å. RESPES is therefore more sensitive to the stoichiometry of the top two O-Ce-O

trilayers (trilayer thickness is 3.1 Å) and less influenced by deeper bulk cerium atoms than XPS.

4.1.5 Objectives

This work extends previous findings by the Thornton group [18] using XPS that showed deposition of Pd nanoparticles on ultrathin films of CeO_{2-x} grown on Pt(111) causes an increase in non-stoichiometry by charge transfer. Here - using $Pt(111)/CeO_{2-x}$ grown by the technique described in [27] and characterised by XPS and LEED - a direct comparison in the calculation of ceria stoichiometry will be made between XPS of the Ce $3d$ region and RESPES of the Ce $4d$-$4f$ transition in the study of the effect of Pd on the ceria surface.

4.2 Experimental

Experiments were conducted at the Materials Science Beamline, ELETTRA Synchrotron, Trieste, Italy. This is a soft X-ray beamline, providing a monochromatic light source in the photon energy range 20-800 eV. The experimental vacuum chamber is fitted with a *Specs PHOIBOS* hemispherical energy analyser (150 mm mean radius with 9 channels), a fast entry lock (FEL), LEED optics, an ion sputtering gun, Ce and Pd evaporators, a dual source Mg/Al K_α X-ray gun, a mass spectrometer and a sample heating system.

Synthesis of ceria thin films was carried out using an established method reported by Schierbaum [27]. A Pt (111) crystal was cleaned by cycles of Ar^+ sputtering, annealing in O_2 at 900 K and in UHV at 1100 K. The clean surface was characterised by a (1×1) hexagonal LEED pattern, and the absence of contaminant peaks (principally carbon and oxygen [43]) in XPS spectra, within the detection limits of
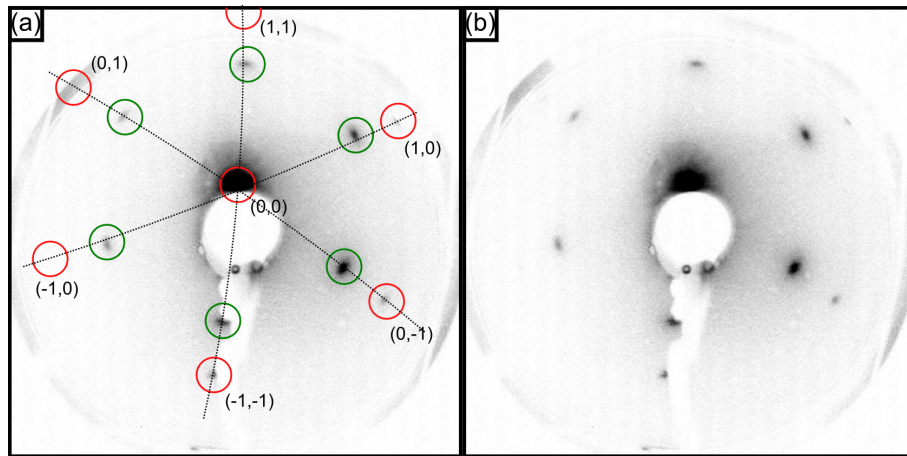
Figure 4.2: LEED (1.37×1.37) pattern for a 0.8 MLE $CeO_{2\text{-x}}$ film on Pt(111). (a) Red circles indicate first order spots from the Pt(111) (labelled), green circles are spots from the $CeO_{2\text{-x}}$. The image is reproduced without symbols in (b) for clarity. E_{beam}=80 eV.

the technique.

Cerium was deposited onto the Pt (111) substrate held at room temperature, then annealed under UHV to 1000 K. This gives rise to a (2×2) hexagonal LEED pattern due to the formation of a Pt-Ce alloy [27]. The deposited cerium was then oxidised by further annealing in 5×10^{-7} mbar O_2 at 1000 K, resulting in a (1.37×1.37) hexagonal LEED pattern (figure 4.2), consistent with a recent study [36]. Palladium was deposited onto the Pt(111)/$CeO_{2\text{-x}}$ films by e-beam heating of a Pd wire under UHV conditions.

XPS spectra were taken at each stage of the Ce $3d$, Pt $4d$, Pd $3d$ and O $1s$ regions using the Al K_α source. The Mg K_α source was inappropriate for use in this experiment as the Pd $M_{4,5}VV$ Auger peak at 327.5 eV [44] would complicate the Ce $3d$ spectra - this is avoided by using the Al K_α source.

XPS of the Ce $3d$ region (870-930 eV) was used to estimate the composition of the ceria as a function of Pd deposition. The Ce^{3+} concentration was calculated using an established procedure, whereby the Ce $3d$ spectrum is fitted with 5 Voigt doublet

peaks. The ion concentration ratio, $r(Ce^{3+}/Ce^{4+})$ is estimated by comparing the XPS peak heights of the features associated with Ce^{3+} to those associated with Ce^{4+}, as expressed by:

$$r(Ce^{3+}/Ce^{4+}) = \frac{\Sigma I_{Ce3+}}{\Sigma I_{Ce3+} + \Sigma I_{Ce4+}} \qquad (4.1)$$

where

$$\Sigma I_{Ce^{3+}} = I_{v_O} + I_{v'} + I_{u_O} + I_{u'} \qquad (4.2)$$

$$\Sigma I_{Ce^{4+}} = I_v + I_{v''} + I_{v'''} + I_u + I_{u''} + I_{u'''} \qquad (4.3)$$

This procedure has been used in a number of other studies [16, 38, 48]. For the Ce 3d spectra of each sample, a Shirley background was calculated, and peak widths and spin-orbit splitting (18.5 eV) were kept constant. It was important to strictly constrain these parameters as changes were relatively small. Following manual input of intensity parameters that provided a visually close fit to experimental data, a least-squares iterative refinement was used to improve the accuracy of the fit. The binding energies and peak widths used (which are adapted from parameters used in a fitting by Skála et al [17] using the same experimental setup) are summarised in table 4.2.

The thicknesses of CeO$_{2-x}$ films and Pd deposits were calculated using the relative areas of overlayer (Ce 3d, Pd 3d) and substrate (Pt 4d) XPS peaks, using the method described in appendix A. Thicknesses, d calculated in Å units can be converted to coverage units of monolayer-equivalence (MLE) by dividing d by the height of one unit cell of the adsorbate. One monolayer in this instance is defined as the number of Pt atoms in the top layer of the substrate; one monolayer equivalent is the number of adsorbate atoms that, when close packed, would uniformly cover the substrate. CeO$_2$ is a cubic structure with a lattice constant of $a = 5.411$Å [45]. Assuming bulk truncation of the (111) surface, this gives hexagonal surface unit cell

	Binding energy /eV	Branching ratio	Gaussian width /eV	Lorentzian width /eV	Voigt width /eV
$v_O + u_O$	880.2 898.7	0.56	1.73	0.93	2.26
$v + u$	882.5 901.0	0.70	1.03	1.35	1.91
$v' + u'$	884.8 903.3	0.56	0.57	4.47	4.54
$v'' + u''$	888.9 907.4	0.61	2.09	4.01	4.90
$v''' + u'''$	898.5 916.9	0.71	1.26	1.60	2.29

Table 4.2: Binding energies, branching ratios, Lorentzian and Gaussian widths and subsequently calculated Voigt widths used in the fitting of Ce $3d$ XPS spectra.

constants of 3.826 Å. Using this value for MLE calculations must be regarded as an approximation since it assumes the CeO$_2$ structure for CeO$_{2-x}$ films - it has been demonstrated that there is a small increase in lattice parameter with increasing x in CeO$_{2-x}$ [46, 47]. For Pd, assuming growth in the (100) direction, the unit cell parameter is 3.89 Å. STM experiments show ceria grows as islands on a Pt(111) surface [36]. Visually these islands cover roughly $\sim 50\%$ of the Pt surface, and from STM line profiles are around one or two O-Ce-O trilayers. Similarly, STM of Pd deposited on Pt(111)/CeO$_{2-x}$ shows preferential adsorption as nanoparticles on ceria islands [18]. The dimensions of these nanoparticles were reported to be between 2-6 Å in height and 5-30 Å in width.

RESPES scans of the valence band (VB, $E_B = 0-16$ eV) were recorded at each stage of deposition over a photon energy range of 113-131 eV using the synchrotron variable energy light source, and normalised to the current induced from the synchrotron beam striking a gold mesh located in front of the experimental UHV chamber.

4.3 Results

Three ceria films are presented here, with estimated thicknesses: (i) 0.5 ± 0.2 MLE, (ii) 0.7 ± 0.2 MLE and (iii) 0.8 ± 0.2 MLE.

4.3.1 XPS of Ce $3d$

The ion concentration ratio, $r(Ce^{3+}/Ce^{4+})$ for the films synthesised shows they have a small degree of non-stoichiometry and are partially reduced prior to Pd deposition. Depositing Pd in sequential stages shows an increase in the Ce^{3+} concentration. Ce $3d$ XPS spectra for a 0.8 MLE CeO$_{2\text{-x}}$ film monitoring this trend are shown in figure 4.3. At high coverages of Pd (above 1 MLE), $r(Ce^{3+}/Ce^{4+})$ appears to tend to a maximum. These results are summarised in table 4.3.

4.3.2 RESPES of the $4d$-$4f$ transition

CIS scans were recorded for the 0.7 and 0.8 MLE films, before and after the stages of Pd deposition. Figure 4.4 shows CIS scans across photon energies of 113-131 eV and binding energies of 0-16 eV for a 0.8 MLE CeO$_{2\text{-x}}$ film with and without a 0.9 MLE Pd deposit. Of particular interest are the peaks that appear at binding energies of 1.5 eV and 4 eV, at photon energies of 121 eV and 124.5 eV respectively. At these resonant energies, electrons are promoted from the core $4d$ levels to the $4f$ valence levels. These promoted electrons can then be excited from the $4f$ level to the vacuum and enhance the valence band peak. The resonant energy of the $4d$-$4f$ transition for Ce^{3+} (121 eV) is slightly less than that for Ce^{4+} (124.5 eV) and as a result there are two distinct resonant peaks. In figure 4.4(b) the addition of 0.9 MLE Pd causes the peak at E_B=1.5 eV to be more intense than in 4.4(a). An examination of the ratio DCe$^{3+}/D$Ce^{4+} of the intensities of these two features gives
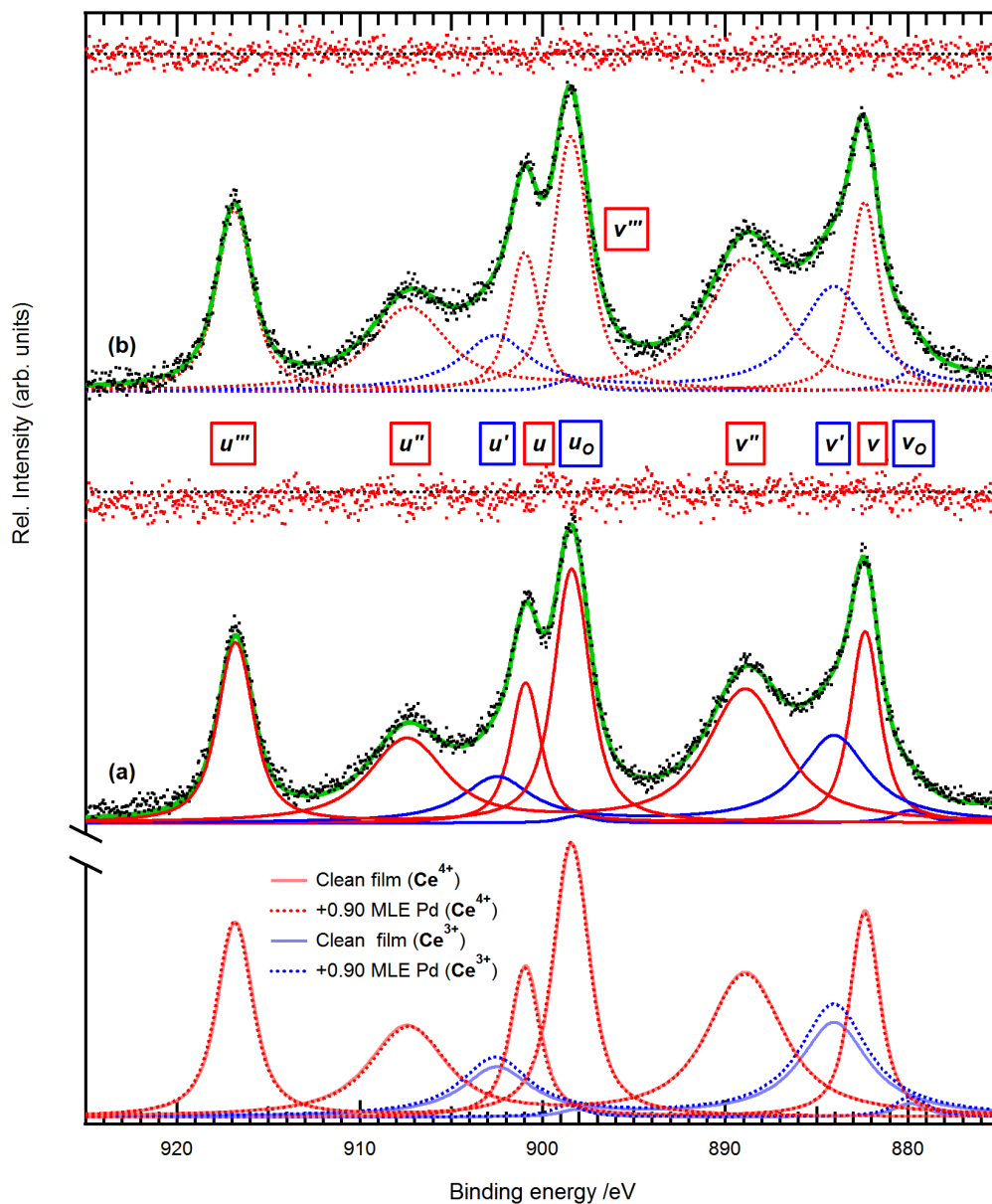
Figure 4.3: Ce 3d XPS spectrum of (a) a 0.8 MLE CeO$_{2-x}$ film and (b) with 0.9 MLE Pd. Blue and red curves correspond to Ce^{3+} and Ce^{4+} Voigt-like contributions respectively and these are compared directly in the broken axes at the bottom of the graph; the green curves are the sum of these calculated doublets, the black dots experimental data points and red dots are residuals. Spectra have been normalised to the same maximum intensity, $h\nu = 1486.6$ eV.

Film	CeO$_{2-x}$ film thickness	Pd thickness	$r(Ce^{3+}/Ce^{4+})$	DCe^{3+}/DCe^{4+}
(i)	0.5±0.2 MLE	0	0.155±0.005	
		0.4±0.3 MLE	0.174 ±0.007	
		1.3±0.9 MLE	0.187 ±0.009	
		5.3±1.2 MLE	0.186 ±0.020	
(ii)	0.7 ±0.2 MLE	0	0.140±0.005	0.220±0.002
		0.3±0.2 MLE	0.151±0.006	0.244±0.002
		0.7±0.6 MLE	0.156±0.008	0.255±0.002
(iii)	0.8±0.2 MLE	0	0.134±0.005	0.219±0.002
		0.9±0.3 MLE	0.161±0.007	0.310±0.002

Table 4.3: Ion concentration, $r(Ce^{3+}/Ce^{4+})$ and resonant peak intensity ratio, DCe^{3+}/DCe^{4+} for the three films presented in this study (i), (ii) and (iii) before and after successive Pd deposition.

an illustration of the composition of the ceria films and the Ce^{3+} concentration.

The intensities of the resonant peaks, DCe^{3+} and DCe^{4+} were measured as the difference between the on-resonance scans and an off-resonance scan (the scan measured at around $h\nu$ =115 eV). Figure 4.5 shows the on- and off-resonance scans for a 0.8 MLE CeO$_{2-x}$ film before and after addition of 0.9 MLE Pd, with subtraction curves (on- minus off-resonance) also displayed. These scans were normalised to the mesh current. The resonant peak DCe^{3+} increases on Pd deposition and increases the ratio DCe^{3+}/DCe^{4+}. The off-resonance scan changes slightly between the deposition step, this difference is due to the lower intensity of the DCe^{4+} peak after depositing Pd which alters the Fano line-shape. These results are summarised in table 4.3.

4.4 Discussion

The three films presented here are ultrathin, with a thickness range of 0.5-0.8 MLE. XPS peak fitting of Ce 3d spectra for the three films shows ion concentration ratios
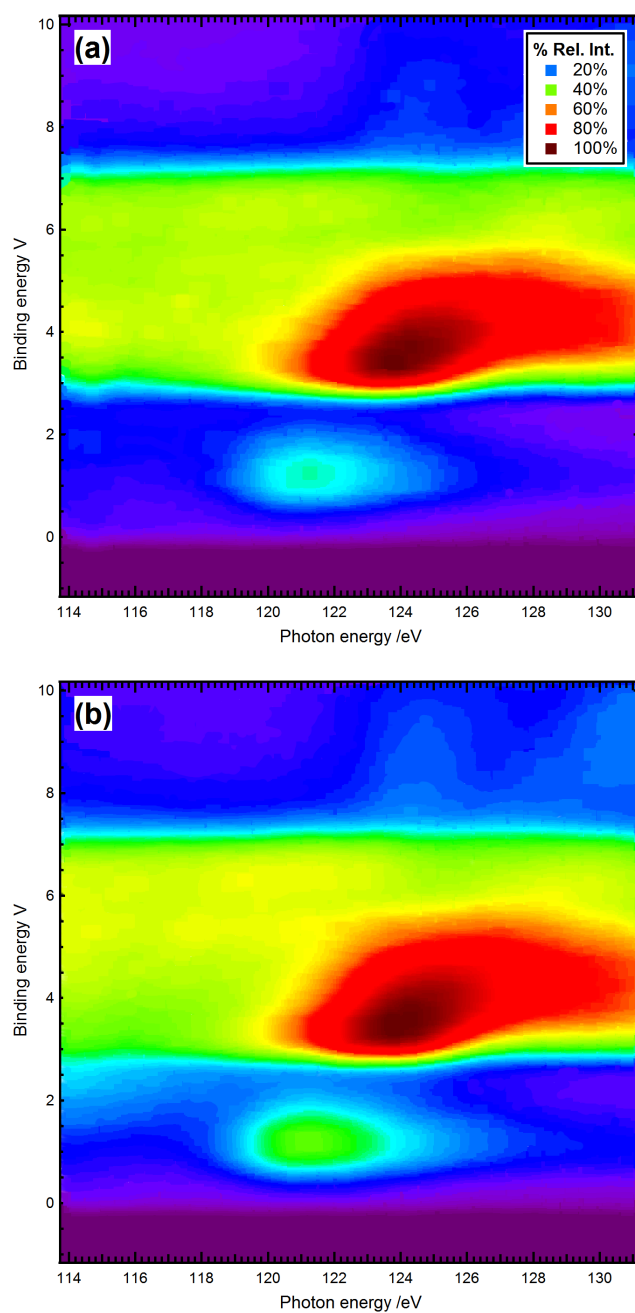
Figure 4.4: CIS scans for (a) a 0.8 MLE CeO$_{2-x}$ film, and with (b) 0.9 MLE Pd across a photon energy range $h\nu = 113 - 131$ eV. The z-axis (colour scale) is the % relative intensity (scans normalised to the same maximum intensity), with electron counts (arbitrary units) as a percentage of maximum intensity indicated by the inset colour scale.
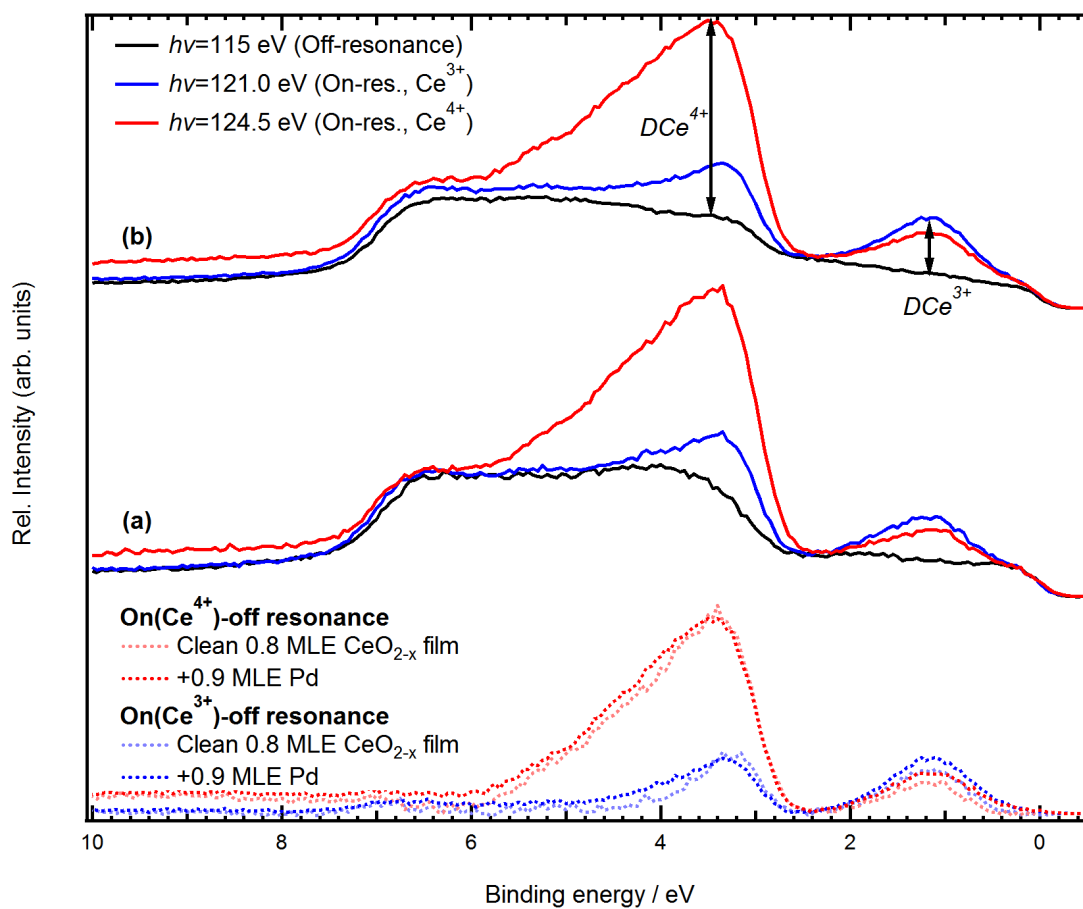
Figure 4.5: VB scans for (a) a 0.8 MLE CeO$_{2-x}$ film, and (b) with 0.9 MLE Pd, showing difference between on- and off-resonance scans. Synchrotron light source used, spectra have been normalised to the mesh current, $h\nu$ indicated in legend.

in the range 0.134-0.155, with a negative correlation suggesting a decreasing ion concentration ratio with increasing film thickness. Previously, a CeO$_{2-x}$ film consisting of three O-Ce-O layers ($\sim$ 11 Å) grown on Pt(111) was reported with an ion concentration ratio of 0.125 [18]. There is less strain in thicker films and hence fewer defects, which result in a lower concentration of Ce^{3+}.

On deposition of Pd, ceria films are reduced, as shown by the increase in ion concentration ratio. In this study only low coverages have been analysed but in the particular case of the 0.5 MLE film there is no appreciable increase in ion concentration ratio between the 1.3 and 5.3 MLE Pd coverages. A low signal-to-noise ratio, caused by increased attenuation by the 5.3 MLE Pd meant that both XPS and RESPES data was of poor resolution and so impossible to meaningfully analyse.

Although the trends evidenced in table 4.3 are consistent in showing an increase in Ce^{3+} concentration with Pd coverage, there is a considerable difference in the percentage change of both $r(Ce^{3+}/Ce^{4+})$ and DCe$^{3+}/D$Ce^{4+} between the three films presented. This discrepancy could arise from variations in growth conditions. Comparing the calculated Pd coverage with deposition times, there is a variation in flux which could affect the wetting of the ceria surface and thus the Ce^{3+} concentration.

RESPES is a more surface sensitive technique than XPS owing to a shorter probe depth. The difference between the ratios $r(Ce^{3+}/Ce^{4+})$ and DCe$^{3+}/D$Ce^{4+} can be explained by the growth of ceria islands rather than homogeneous monolayer by monolayer growth, as supported by STM studies [18, 36]. Thus RESPES is more sensitive to Ce^{3+} ions in the top two O-Ce-O trilayers. Further investigation using STM will provide more information regarding surface morphology.

DFT calculations showed that on deposition of Pd, charge transfer takes place from Pd atoms to Ce, resulting in Pd$^+$ and Ce^{3+} [18]. Results presented here confirm this observation, since the ion concentration ratio is seen to increase with Pd deposition as observed by both techniques. Similarly, these results compare favourably with

previous experiments of metals on CeO$_{2\text{-x}}$ thin films, although the effect is much more subtle than compared with for instance Ga [23].

4.5   Conclusions

The effect of Pd deposits on ultrathin films of CeO$_{2\text{-x}}$ grown on Pt(111) has been examined using XPS and RESPES. Both techniques show an increase in the ion concentration ratio, indicating an increase in Ce^{3+} states. In principle, reduction of the films could be due to oxygen vacancies created on deposition of Pd or charge transfer from the Pd nanoparticles to the ceria films. Evidence from recent DFT calculations [18] indicates the latter, with a charge transfer from Pd to Ce ions. The use of RESPES to analyse the valence band affords a higher degree of sensitivity to changes in the top O-Ce-O trilayer, where this charge transfer is expected to occur. The reducibility of ceria is an important property in its function as a catalyst, and the addition of Pd can enhance its catalytic function particularly with regard to its oxygen storage capacity.

References

[1] Trovarelli, A.; *Catalysis by Ceria and Related Materials, Vol. 2*, **2000**, Imperial College Press, London

[2] Kašpar, J., Fornasiero, P., Graziani, M.; *Catal. Today*, **1999**, *50*, 285

[3] Taylor, K.C.; *Catal. Rev. - Sci. Eng.*, **1993**, *35*, 457

[4] Trovarelli, A.; *Catal. Rev. - Sci. Eng.*, **1996**, *38*, 439

[5] Yao, H.C., Yu Yao, Y.F.; *J. Catal.*, **1984**, *86*, 254

[6] Lööf, P., Kasemo, B., Heck, K.-E.; *J. Catal.*, **1989**, *118*, 339

[7] Harrison, B., Diwell, A.F., Hallett, C.; *Platinum Metals Rev.*, **1988**, *32*, 73

[8] Su, E.C., Montreuil, C.N., Rothschild, W.G.; *Appl. Catal.*, **1985**, *17*, 75

[9] Engler, B., Koberstein, E., Schubert, P.; *Appl. Catal.*, **1989**, *48*, 71

[10] Hoskins, B.F., Martin, L.R.; *Aust. J. Chem.*, **1995**, *48*, 709

[11] Carter, C.B., Norton, M.G.; *Ceramic materials: science and engineering*, **2007**, Springer

[12] Minervini, L., Zacate, M.O., Grimes, R.W.; *Solid State Ionics*, **1999**, *116*, 339

[13] Sørenson, O.T.; *Non-stoichiometric oxides*, **1981**, Academic Press, New York

[14] Pfau, A., Schierbaum, K.D., Gopel, W.; *Surf. Sci.*, **1995**, *331*, 1479

[15] Senanayake, S.D., Zhou, J., Baddorf, A.P., Mullins, D.R.; *Surf. Sci.*, **2007**, *601*, 3215

[16] Zhang, F., Wang, P., Koberstein, J., Khalid S., Chan, S.-W.; *Surf. Sci.*, **2004**, *563*, 74

[17] Skála, T., Šutara, F., Škoda, M., Prince, K.C., Matolín, V.; *J. Phys. Condens. Matter*, **2009**, *21*, 055005

[18] Wilson, E. L., Grau-Crespo, R., Pang, C. L., Cabailh, G., Chen, Q., Purton, J. A., Catlow, C. R. A., Brown, W. A., de Leeuw, N. H., Thornton, G.; *J. Phys. Chem. C*, **2008**, *112*, 10918

[19] Schierbaum, K.D., Fischer, S., Torquemada, M.C., de Segovia, J.L., Roman, E., Martin-Gago, J.A., *Surf. Sci.*, **1996**, *345*, 261

[20] Matolín, V., Cabala, M., Chab, V., Matolínova, I., Prince, K.C., Škoda, M., Šutara, F., Skála, T., Veltruská, K.; *Surf. Interface Anal.*, **2008**, *40*, 225

[21] Škoda, M., Cabala, M., Cháb, V., Prince, K.C., Sedlacek, L., Skála, T., Šutara, F., Matolín, V.; *Appl. Surf. Sci.*, **2008**, *254*, 4375

[22] Škoda, M., Cabala, M., Matolínova, I., Prince, K.C., Skála, T., Šutara, F., Veltruská, K., Matolín, V.; *J. Chem. Phys.*, **2009**, *130*, 034703

[23] Skála, T., Šutara, F., Cabala, M., Škoda, M., Prince, K.C., Matolín, V.; *Appl. Surf. Sci.*, **2008**, *254*, 6860

[24] Matsumura, Y., Shen, W.-J., Ichihashi, Y., Okumura, M.; *J. Catal.*, **2001**, *197*, 267

[25] Hilaire, S., Wang, X., Luo, T., Gorte, R.J., Wagner, J.; *Appl. Catal. A*, **2001**, *215*, 271

[26] Bunluesin, T., Gorte, R.J., Graham, G.W.; *Appl. Catal. B*, **1998**, *15*, 107

[27] Schierbaum, K.D.; *Surf. Sci.*, **1998**, *399*, 29

[28] Berner, U.. Schierbaum, K.D.; *Phys. Rev. B Condens. Matter*, **2002**, *65*, 2354041

[29] Hardacre, C., Roe, G.M., Lambert R.M.; *Surf. Sci.*, **1995**, *326*, 1

[30] Rodriguez, J.A., Jirsak, T., Sambasivan, S., Fischer, D., Maiti, A.; *J. Chem. Phys.*, **2000**, *112*, 9929

[31] Eck, S. Castellarin-Cudia C., Surnev, S., Ramsey, M.G., Netzer, F.P.; *Surf. Sci.*, **2002**, *205*, 173

[32] Xiao, W., Guo, Q., Wang, E.G.; *Chem. Phys. Lett.*, **2003**, *368*, 527

[33] Siokou, A., Nix, R.M.; *J. Phys. Chem. B*, **1999**, *103*, 6984

[34] Mullins, D.R., Radulovic, P.V., Overbury, S.H.; *Surf. Sci.*, **1999**, *429*, 186

[35] Alexandrou, M., Nix, R.M.; *Surf. Sci.*, **1994**, *321*, 47

[36] Grinter, D.C., Ithnin, R., Pang, C.L., Thornton, G.; *J. Phys. Chem. C*, **2010**, *114*, 17036

[37] Burroughs, P., Hamnett, A., Orchard, A.F., Thornton, G.; *J. Chem. Soc. Dalton Trans.*, **1976**, 1686

[38] Romeo, M., Bak, K., El Fallah, J., Le Normand, F., Hilaire, L.; *Surf. Interf. Anal.*, **1993**, *20*, 508

[39] Cardona, M., Ley, L., eds.; *Photoemission in Solids I: General Principles*, Springer-Verlaug, Berlin, **1978**

[40] Šutara, F., Cabala, M., Sedláček, L., Skála, T., Škoda, M., Matolín, V., Prince, K.C., Cháb, V.; *Thin Solid Films*, **2008**, *516*, 6120

[41] Matolín, V., Sedlacek, L., Matolínova, I., Šutara, F., Skála, T., Smid, B., Libra, J., Nehasil, V., Prince, K.C.; *J. Phys. Chem. C*, **2008**, *112*, 3751

[42] Skála, T., Šutara, F., Prince, K.C., Matolín, V.; *J. Electron Spectrosc. Rel. Phenom*, **2009**, *169*, 20

[43] Grunze, M., Ruppender, H., Elshazly, O.; *J. Vac. Sci. Technol. A*, **1988**, 1266

[44] Brun, M., Berthet, A., Bertolini, J. C.; *J. Electron Spectrosc. Rel. Phenom*, **1999**, *104*, 55

[45] K.A. Gschneider, K.A., Eyring, L. (Eds); *Handbook on the Physics and Chemistry of Rare Earth*, **1979**, North-Holland, Amsterdam.

[46] Brauer, D.J.M.; *J. Inorg. Nucl. Chem.*, **1955**, *1*, 49

[47] Chiang, H.W., Blumenthal, R.N., Fournelle, R.A.; *Solid State Ionics*, **1993**, *66*, 85

[48] Preisler, E., Marsh, O.J., Beach, R.A., McGill, T.C.; *J. Vac. Sci. Tech. B*, **2001**, *19(4)*, 1611

Chapter 5

Synthesis of $TiO_2(110)$ ultrathin films on W(100) and their reactivity with H_2O

5.1 Introduction

5.1.1 Importance of TiO_2

The last two decades have seen an increase in interest in the study of metal oxides. Much modern technology is dependent on the properties of metal oxide surfaces [1] and their wide range of applications [2], including heterogeneous catalysis, supports for catalysts, metal-ceramic interfaces, gas sensors and in solid-state devices.

Titanium dioxide, $TiO_2(110)$ is the most studied metal oxide surface [3] and is considered to be the prototypical metal oxide system [4], owing to its stability, relative ease of preparation, availability as a single crystal, electrical conductivity when reduced and its use in a wide range of applications, such as in catalysis and pho-

tocatalysis. Indeed, the behaviour of TiO$_2$ is determined by the stoichiometry at the surface. Although perfect TiO$_2$ is a 3.1 eV band gap material [5], when reduced there is sufficient electrical conductivity to use electron based spectroscopies and tunnelling techniques to probe the surface. However, difficulties lie in the reproducible preparation and interrogation of non-stoichiometric surfaces [6], and this requires further study.

5.1.2   TiO$_2$ thin film synthesis

Thin films that are sufficiently ordered to mimic the surfaces of their bulk counterparts can be synthesised [7], providing a means to modify the stoichiometry in a more controlled fashion. Lithographic techniques offer a "top-down" approach to the formation of thin films, but are slow and structures are limited to a minimum thickness of ~ 100 Å. The alternative "bottom-up" approach [8, 9] is to grow epitaxial thin films [10, 11] that are well-ordered and exhibit sufficient conducting character to enable study by electron spectroscopy and scanning tunnelling microscopy (STM) [12]. Previously, thin films grown on refractory metal substrates have been shown to provide a suitable system for surface science studies of their properties [11, 13–15]. Moreover, these properties are similar to those of bulk materials. Ultra-thin films - those which are less than 10 Å thick - offer the potential for new applications, such as in high density visual displays [16].

The first issue to address in the growth of stoichiometric thin films is the choice of a suitable substrate. The lattice parameters of the TiO$_2$(110) unit cell have a high aspect ratio (2.19) which is a barrier to simple epitaxial match with most metals. However, successful growth of TiO$_2$ thin films has been reported on Cu(001) [17], Mo(100) [18], Mo(110) [19], Mo(112) [20], Ni(110) [21, 22], Pt(111) [23], Ru(0001) [24] and W(100) [25].

Growth on the W(100) surface

McCavish and Bennett report that W(100) is an appropriate surface to use as a substrate for TiO$_2$(110) stoichiometric thin films [25]. Upon adsorption of oxygen, the surface undergoes a p(2×1) reconstruction [26, 27], resulting in a unit cell of dimensions 6.32 × 3.16 Å^2. This is comparable in size to the TiO$_2$ (110) unit cell, 6.49 × 2.96 Å^2, a 2.7% × −6% mismatch. Films were grown by metal vapour deposition of Ti in UHV with subsequent annealing in O$_2$ and by reactive deposition of Ti in an O$_2$ partial pressure. Fully oxidised and ordered TiO$_2$(110) thin films, of thickness 0.5-30 ML exhibit a LEED pattern that is a composite of the (1 × 1) pattern observed from a clean, ordered W(100) surface and the (1 × 1) pattern from an ordered TiO$_2$ surface, resulting in streaking along the principal axes. Films grown by this technique have been used for studies using vibrational spectroscopy [28] and STM [29].

5.1.3 The TiO$_2$(110) surface and reactivity with H$_2$O

The TiO$_2$ rutile unit cell is shown in figure 5.1(a). The (110) surface is the most stable and consists of alternate rows of bridging oxygen atoms (O$_b$) and fivefold coordinate titanium atoms (Ti$_{5c}$) with a periodicity of 6.49 Å (figure 5.1(b) and (c)).

TiO$_2$ is widely used in heterogeneous catalysis, and surface science studies of the material are most extensive in the area of adsorption of molecules and atoms, and their dissociation and/or reactions [4]. Water (H$_2$O) is probably the most important of these adsorbates at the TiO$_2$ surface. Many applications of TiO$_2$ take place in aqueous environments (for example photocatalytic applications). Titanium is also a very useful material in medical applications, since it is light, has excellent mechanical properties, a low corrosion rate and good biocompatibility. Over the course of several
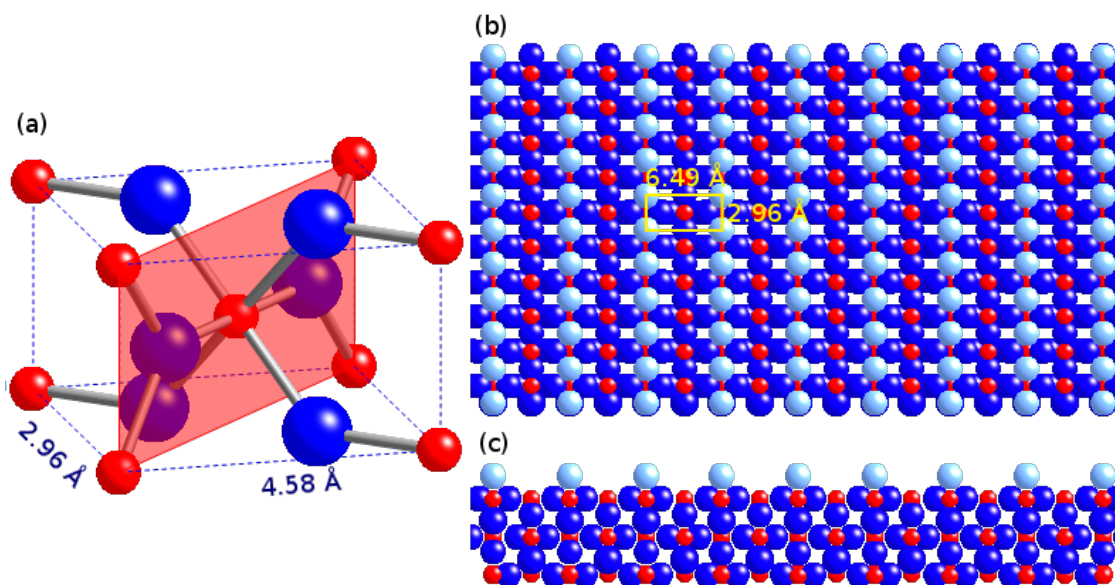
Figure 5.1: Models depicting (a) TiO$_2$ rutile unit cell, with the (110) plane marked, (b) top view and (c) side view of the (110)(1×1) surface. Ti atoms are red, top-layer bridging O atoms in light blue and subsurface O atoms in blue.

months, strong bonding can develop between the metal and living tissue or bone, making Ti and Ti alloys excellent materials for medical implants and prostheses [30]. Even in ultra-high vacuum (UHV), H$_2$O adsorption must be considered as it is a significant component of the residual gas.

Fujishima and Honda demonstrated the use of TiO$_2$ as an electrode in an electrochemical cell and showed that H$_2$O dissociates on the surface of TiO$_2$ in the presence of UV light [31]. Surface science studies of the H$_2$O interaction with the TiO$_2$(110) surface began to build up a picture of the adsorption process and revealed evidence for the presence of surface hydroxyls (as a result of dissociation) at room temperature, although it was thought that dissociation did not occur on defect free surfaces [32–35].

Synchrotron radiation studies by Kurtz et al showed an increase in Ti^{3+} defect state density on dissociative adsorption of H$_2$O on nearly perfect TiO$_2$(110) surfaces [36]. Similarly on other surfaces of TiO$_2$, earlier work suggested that the concentration of

surface OH was independent of defect density concentration [37–39]. Pan et al [40] showed that there is negligible correlation between H$_2$O saturation of a slightly defective TiO$_2$(110) surface (0.08 ML oxygen vacancies, O$_{vac}$) with surface defect concentration, compared to a fully stoichiometric surface. Dosing onto a highly defective surface (0.4 ML O$_{vac}$) resulted in a higher H$_2$O saturation coverage limit. Temperature Programmed Desorption (TPD) measurements found that molecular water desorbs at 275 K but that around 25% is disproportionated and remains as surface OH [41]. Further TPD measurements by Henderson showed that molecular water desorbs from the TiO$_2$(110) surface at 270 K, and that multilayer H$_2$O adsorption only occurs below 175 K [42]. The importance of defects in the dissociation reaction was shown since perfect TiO$_2$(110) showed only molecular adsorption (below 270 K) and absence of surface hydroxyls - thus TiO$_2$(110) is only active to H$_2$O dissociation if structural defects such as kinks, step edges or oxygen vacancies are present [42, 43].

The application of scanning tunnelling microscopy (STM) to the interaction of H$_2$O with TiO$_2$ in the last decade has provided more insight into the mechanism of dissociation. It was confirmed that molecular water adsorbs at 150 K on fivefold co-ordinate Ti sites, Ti$_{5c}$, but desorbs by 290 K to leave two bridging hydroxyls, OH$_b$, one in place of an O$_{vac}$ and a second on one of the two nearest neighbouring O$_b$ [44–46]. Non-contact atomic force microscopy, NC-AFM confirmed the STM findings [47].

Adsorption Mechanism

In summation of the literature discussed, the current accepted mechanism for adsorption and dissociation of H$_2$O on TiO$_2$(110) at room temperature is presented (figure 5.2). An H$_2$O molecule adsorbs at an O$_{vac}$ site. Dissociation occurs and results in an OH pair: an OH$_b$ group in place of the O$_{vac}$, and a second OH$_b$ formed
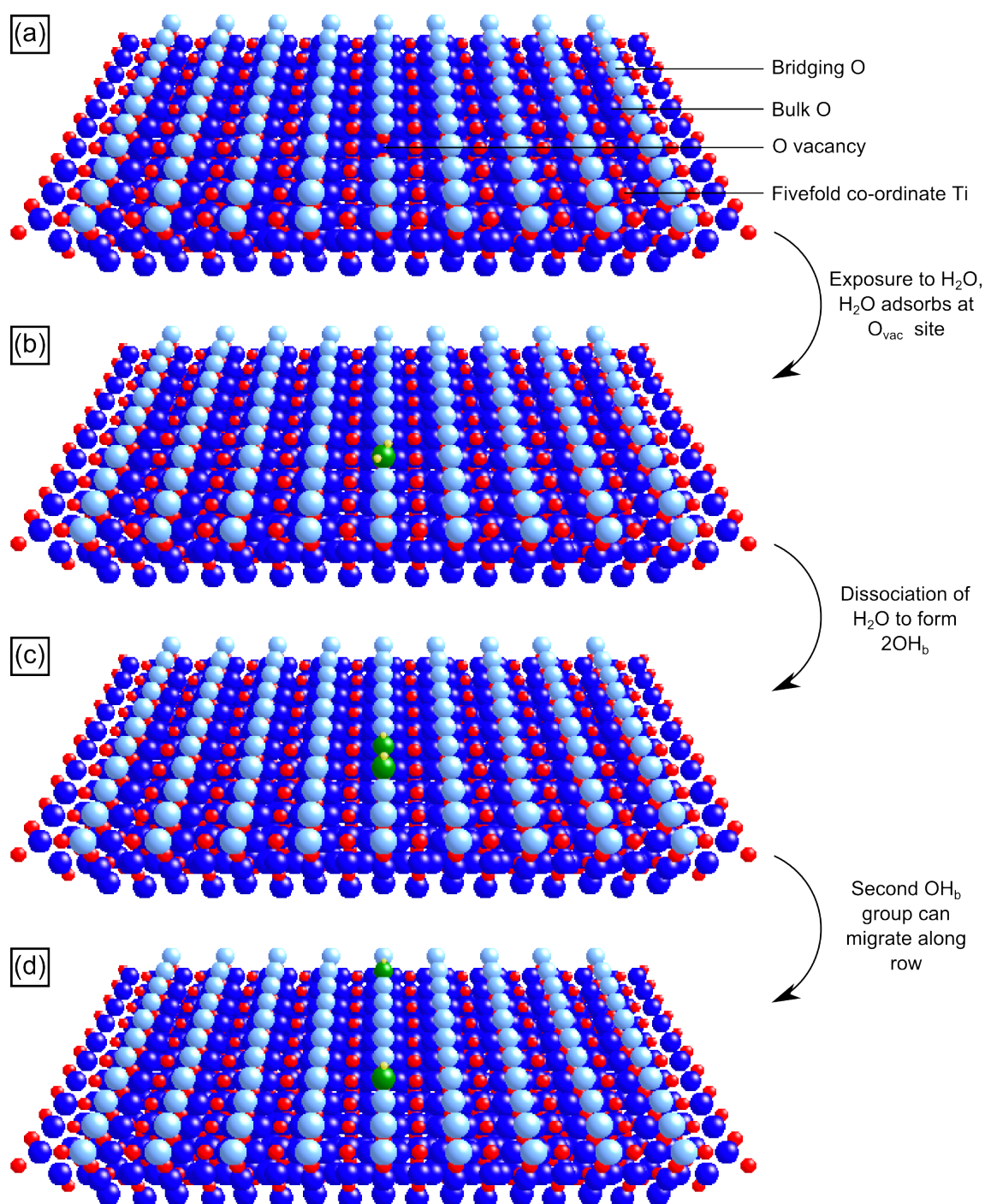
Figure 5.2: Schematic diagram showing the mechanism of adsorption and dissociation of H$_2$O on the TiO$_2$(110) surface to form an OH pair. Ti atoms are red, O$_b$ are sky blue and subsurface O are blue. H$_2$O and subsequent dissociation products are represented by a green O atom and two yellow H atoms.

from the dissociated H atom and another bridging O (O$_b$) atom:

$$H_2O + O_{vac} + O_b \longrightarrow 2OH_b \qquad\qquad (xi)$$
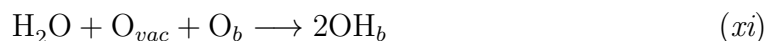
5.1.4 Interaction between hydroxylated-TiO$_2$(110) and O$_2$

The resulting OH$_b$ pair from the H$_2$O dissociation reaction plays an important role in reactivity of the surface with O$_2$. Diffusion of H atoms can take place, and two mechanisms for this action are proposed. Below 300 K, migration is dominated by H transition along the same O$_b$ row (along the [001] direction) [46]. However at low OH$_b$ coverage and above 400 K the dominant mode of migration is H$_2$O mediated to neighbouring rows in the [1$\bar{1}$0] direction [48], although at such temperatures high H$_2$O coverages are not possible due to the high desorption rate [49].

Molecular oxygen, O$_2$ has also been shown to dissociate in O$_{vac}$, healing the vacancy with an O$_b$ and an additional adatom (O$_a$) adsorbed on a Ti$_{5c}$ site [45, 50–53]:

$$O_2 + O_{vac} \longrightarrow O_b + O_a \qquad\qquad (xii)$$

A second pathway has also been proposed [54]:

$$O_2 \xrightarrow{\text{Ti}_{5c}^{4+}} 2O_a \qquad\qquad (xiii)$$

In the absence of O$_{vac}$, O$_2$ can also react directly with OH$_b$ [55, 56]. This reaction proceeds via the creation of intermediate products HO$_2$, terminal hydroxyl groups (OH$_t$) and O$_a$ [57]:

$$OH_b + O_2 \longrightarrow O_b + HO_2 \qquad\qquad (xiv)$$

$$OH_b + O_a \longrightarrow OH_t + O_b \qquad\qquad (xv)$$

$$OH_b + HO_2 \longrightarrow O_b + O_a + H_2O_{(g)} \qquad\qquad (xvi)$$

$$OH_b + OH_t \longrightarrow O_b + H_2O_{(g)} \qquad\qquad (xvii)$$
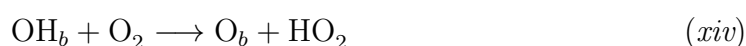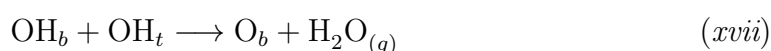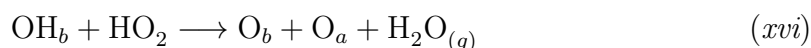
For a partially hydroxylated TiO$_2$(110) surface, a proposed mechanism suggests H$_2$O acts as a catalyst in the reactions (xv) and ($xvii$). Step (xiv) is the initial step in the reaction and thus elimination of OH$_b$ is much slower for partial hydroxylation. The overall reaction can be simplified to:

$$O_2 + 4OH_b \longrightarrow 4O_b + 2H_2O_{(g)} \qquad\qquad (xviii)$$
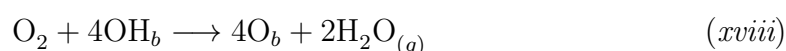
The intermediate species, HO$_2$ and OH$_t$ have been observed with STM [58]. The reaction with O$_2$ and OH$_b$ is direct and spontaneous, and there is a charge transfer from the surface to the molecule largely coupled to the transfer of a proton (H$^+$) from OH$_b$ [59].

5.1.5 Objectives

Here, ultrathin films of TiO$_2$(110) will be synthesised on a W(100) substrate to use as a model system to investigate the reaction with H$_2$O. The reactivity of the hydroxylated TiO$_2$(110) surface with O$_2$ will also be examined. Whilst a method for growth of ultrathin TiO$_2$(110) films on Ni(110) has previously been established and used with STM by the Thornton group [21], Ni is a ferromagnet and so cannot be

used with electron paramagnetic resonance (EPR). W(100) however, is a paramagnet and thus could provide a suitable system for future study using EPR. Films of ultrathin thickness (<20 Å) - comparable to the thinnest films previously reported in [25] - will be studied as this avoids charging when using charged probes [60]. XPS and LEED will be utilised to check order and structure of the films and changes in electronic structure on exposure to water.

5.2 Experimental

Experiments were conducted in an ultra high vacuum (UHV) chamber with a base pressure of 3×10^{-10} mbar. The system was equipped with the necessary instruments for sample preparation (Ar$^+$ ion gun for sputtering and sample heating system) and characterisation (LEED and XPS). Data was recorded at room temperature, using an unpolarised Mg K_α radiation source ($h\nu = 1253.6$ eV) and a *VSW/Omicron* EA125 hemispherical analyser. Measurements were made with the sample at normal emission to the analyser ($\theta_{em} = 0°$); the angle of incidence of X-ray photons was $\phi_{inc} = 45°$. A pass energy of 40 eV was used giving an energy resolution of 0.3 eV, and the angular acceptance was $\Delta\theta = \pm 6°$. The experimental chamber is described in further detail in chapter 3. Binding energies were measured relative to the Fermi level which was measured at each stage, to within 0.1 eV.

The W(100) crystal (*SPL*) was cleaned by Ar$^+$ sputtering, followed by repeated cycles of annealing in 1×10^{-7} mbar of high purity O$_2$ (*SIP Analytical*) at 1100 K and flash annealing in UHV to 2000 K to remove principal contaminants O and C [61]. The clean surface was characterised by a sharp (1×1) LEED pattern and the absence of O 1s and C 1s peaks in XPS spectra, within the detection limits of the technique. The temperature of the sample was monitored using an optical pyrometer (Cyclops 100, *Land Instruments International*).
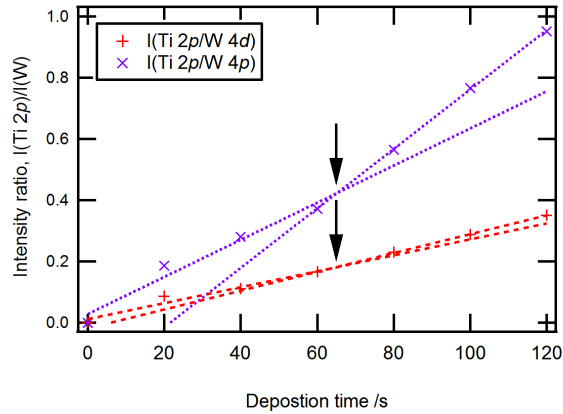
Figure 5.3: Calibration of the Ti doser was achieved by monitoring the intensity ratio, $I(Ti2p)/I(W)$ in XPS (using Mg K_α, $h\nu = 1253.6$ eV). Breakpoints in the ratios, indicated by arrows correspond to a coverage of 1 ML Ti.

Ti was deposited using a home-built e-beam evaporator as described in section 3. The doser was calibrated using the intensity ratios of the Ti $2p$, W $4p$ and W $4d$ XPS peaks as shown in figure 5.3. Breakpoints in the ratios indicate monolayer coverage [62] and can be used to approximate the amount of Ti deposited. Oxidation of deposited Ti was achieved by annealing in 1×10^{-7} mbar O₂ at 800 K for 2 hrs.

Films were characterised by a (1×1) LEED pattern with additional spots along the axes [25] and the stoichiometry estimated from Ti $2p$ XPS spectra. Film thicknesses were estimated from the areas of the Ti $2p$ and W $4d$ XPS peaks, using the method described in appendix A.

De-ionised H₂O was prepared for dosage by degassing using freeze-pump-thaw (FPT) cycles (as described in section 3.2.1). Degassed H₂O was dosed into the vacuum chamber using a high precision leak valve. Exposures were measured in Langmuir units, L, where 1 L = 1.32×10^{-6} mbar · s.

5.3 Results

5.3.1 TiO$_2$(110) thin film growth

Growth approaches

Three approaches to ultrathin film growth were used (based on [25]): Ti was deposited onto a clean W(100) surface in UHV (two-stage growth) onto a pre-oxidised W(100) surface in UHV (pre-oxidised growth) and in a partial pressure of O$_2$ (reactive growth). After annealing in O$_2$, samples were allowed to cool to room temperature in vacuum before measurements were made.

Two-stage growth   Ti deposited on the clean W(100) surface is metallic in nature. This was evident from XPS of the Ti 2p region, showing asymmetric Doniach-Šunjić [63] type peaks at E_B=454.7 eV (2$p_{3/2}$) and 460.7 eV (2$p_{1/2}$) (bottom spectrum, figure 5.4(a)), indicative of metallic Ti in its ground state [64]. The presence of a small amount of Ti^{2+} and Ti^{3+} states cannot be ruled out. After annealing in 1×10^{-7} mbar O$_2$ at 800 K for 2 hrs, oxidation causes the Ti 2p XPS peaks to shift to 459.0 eV (2$p_{3/2}$) and 464.7 eV (2$p_{1/2}$), typical of Ti^{4+} [66,67](top spectrum, figure 5.4(a)).

Pre-oxidised deposition   In the case of Ti deposition on the W(100) surface which has been pre-oxidised by annealing in 1×10^{-7} mbar O$_2$ at 800 K for 3 min, the Ti 2p XPS peaks bear some resemblance to those of Ti on the clean W(100) surface with some broadening (figure 5.4(b)). Again, these peaks shift to positions associated with Ti^{4+} states after the 2 hr O$_2$ anneal.
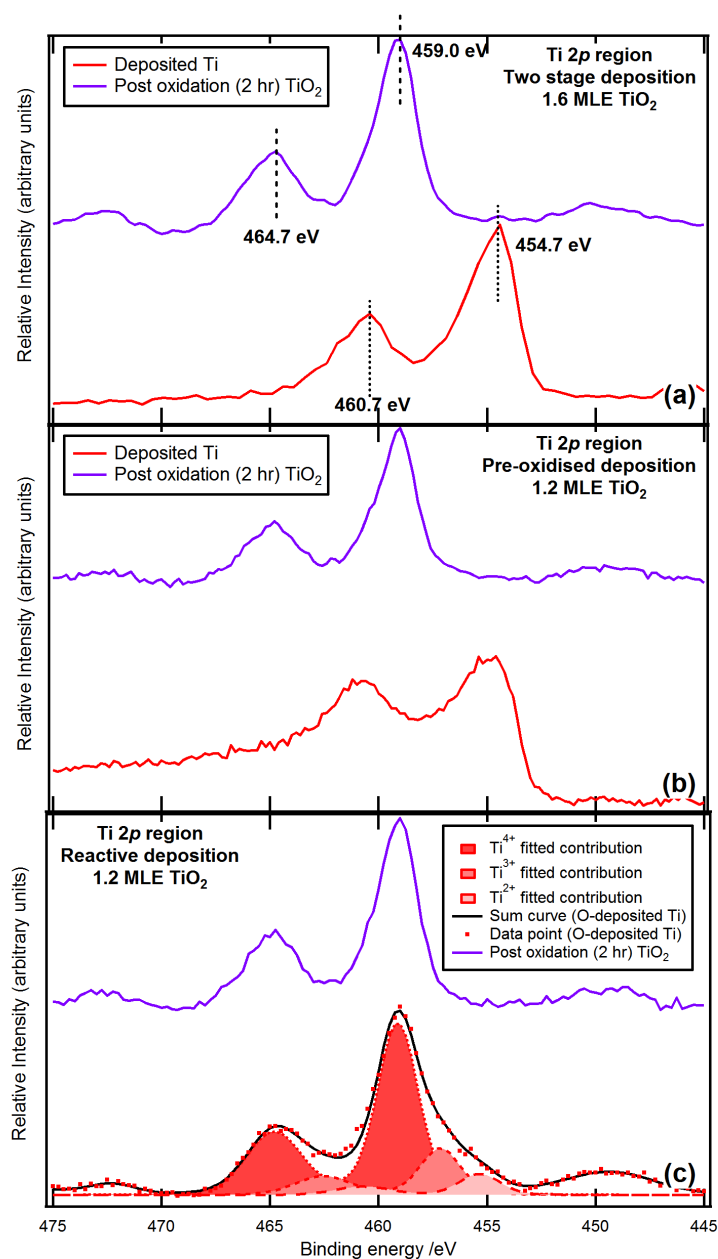
Figure 5.4: XPS spectra showing (a) the shift in E_B of the Ti2p peaks after oxidation in 1×10^{-7} mbar O$_2$ for 2 hr at 800 K for a 1.6 MLE TiO$_2$ film, (b) the broadened Ti 2p peaks of Ti deposited on an oxidised W(100) surface (bottom) and the shift to fully oxidised peaks after oxidation in 1×10^{-7} mbar O$_2$ for 2 hr at 800 K (top) for a 1.2 MLE TiO$_2$ film and (c) the mixed valence Ti states on depositing Ti in 1×10^{-7} mbar O$_2$ (bottom), and the removal of these states on oxidation in 1×10^{-7} mbar O$_2$ for 2 hr at 800 K (top) for a 1.2 MLE TiO$_2$ film. Spectra normalised to same maximum intensity and Shirley backgrounds subtracted, $h\nu = 1253.6$ eV.

Reactive deposition Depositing Ti in 1×10^{-7} mbar O_2 initially results a Ti $2p$ spectrum showing contributions from Ti^{4+} states as well as reduced Ti^{3+} and Ti^{2+} states (figure 5.4(b)) [66] indicating incomplete oxidation. After the 2 hr O_2 anneal the Ti $2p$ XPS peaks sharpen as Ti^{2+} states (at E_B=455.4 eV and 460.8 eV) were removed completely and Ti^{3+} states were largely removed.

LEED

Films of between 0.2-5.7 MLE TiO_2(110) were synthesised. One monolayer equivalent in this instance is defined as the number of close packed TiO_2 surface unit cells that will uniformly cover the surface of the W(100) substrate. On deposition of Ti, the observed LEED pattern consists of a very high background with the faint (1×1) spots of the W(100) substrate, indicating no long range order in the deposited Ti. Fully oxidised films produced LEED patterns (figure 5.5, (c)) that were a composite (1×1) spots of the W(100) substrate (figure 5.5, (a)) and the (1×1) spots of the LEED pattern from an ordered TiO_2(110) surface (figure 5.5, (b))*. Additional spots appear along both axes, indicating that TiO_2(110) films grow in two domains. In films of thickness < 1 MLE, LEED patterns were faint, likely due to incomplete coverage of the W(100) substrate and oxidation of regions of bare W(100). In films of thickness > 1 MLE patterns were clearer for the films.

XPS

Surface Stoichiometry Examination of Ti $2p$ XPS spectra shows that synthesised films were not completely stoichiometric and that contributions from Ti^{3+} and Ti^{4+} states were present (figure 5.6). Reduced states can arise from surface defects or charge transfer from the W substrate to interfacial Ti [28]. Deconvoluting the Ti

---

*LEED pattern of TiO_2(110) recorded by Chi-Ming Yim at University College London as part of his PhD research, used with permission.
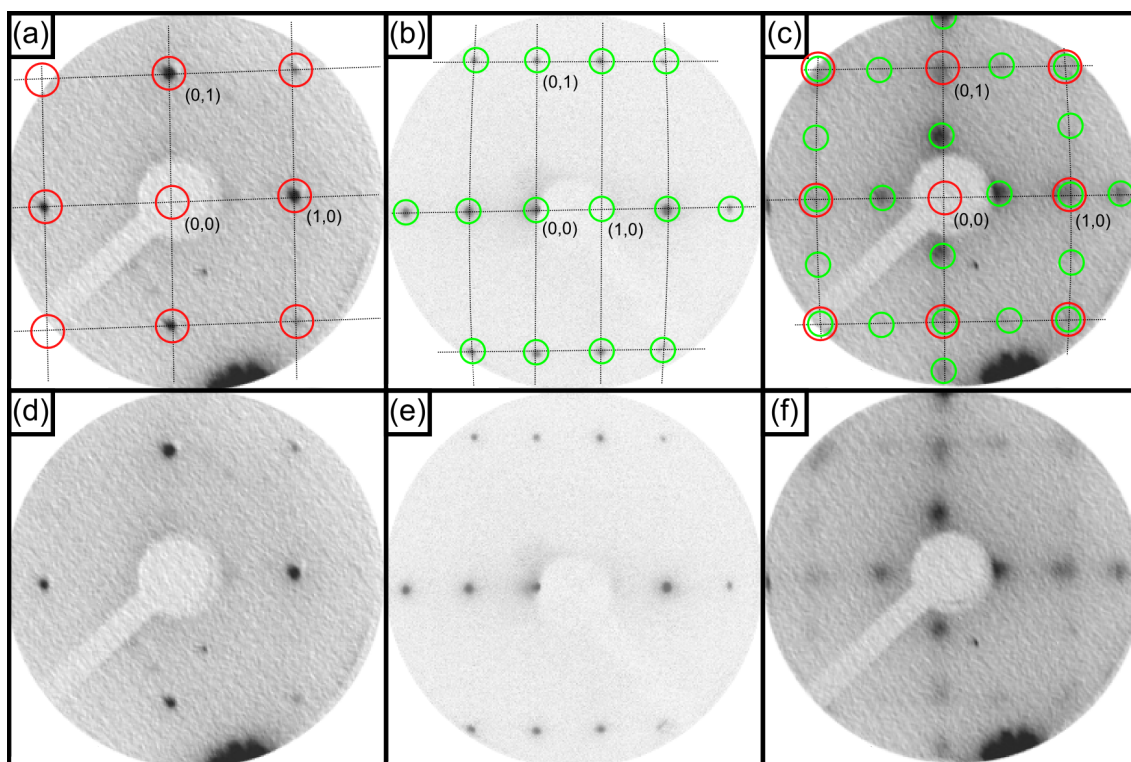
Figure 5.5: LEED patterns for (a) the clean W(100) surface (beam energy, $E_{beam} = 55$ eV), with red circles indicating the (1×1) spots (first order W(100) spots labelled), (b) a reference TiO$_2$(110) crystal ($E_{beam} = 66$ eV), with the green circles indicating the (1×1) spots (first order TiO$_2$(110) spots labelled) and (c) the composite pattern displayed from a 5.8 MLE TiO$_2$(110) film grown by the pre-oxidised method on W(100) ($E_{beam} = 55$ eV), with red and green circles showing the composite nature of the pattern (first order W(100) spots labelled). The figures are reproduced (d-f) without the symbols for clarity.

$2p$ spectrum gives a quantifiable estimation of these states and non-stoichiometry can be expressed as %Ti^{3+} states present. Fitting parameters are given in table 5.1. It was found that there was a greater degree of non-stoichiometry in thinner films, and that %Ti^{3+} states in the films decreases with increasing thickness (figure 5.7). In very thin films, there is a larger influence on the signal from interfacial states where there is a greater substrate charge transfer. However, the resolution of Ti $2p$ peaks for thinner films is poor due to low intensity above the noise level, introducing a greater deal of uncertainty over the %Ti^3+ value. This correlation has been previously observed [25] and is due to reduced strain in the thicker films.
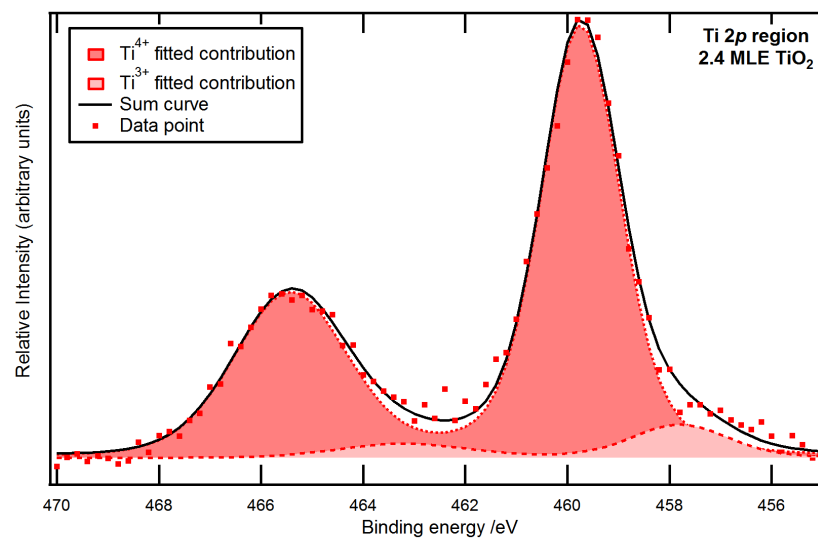
Figure 5.6: Ti 2p XPS spectrum showing contributions from Ti^{3+} and Ti^{4+} ions in a 2.4 MLE thick TiO$_2$(110) film grown using the pre-oxidised W(100) method, as estimated by fitting with two Voigt doublets. Ti^{3+} ions make up 8.57% of all Ti sites in the film. A Shirley background has been subtracted, $h\nu = 1253.6$ eV.
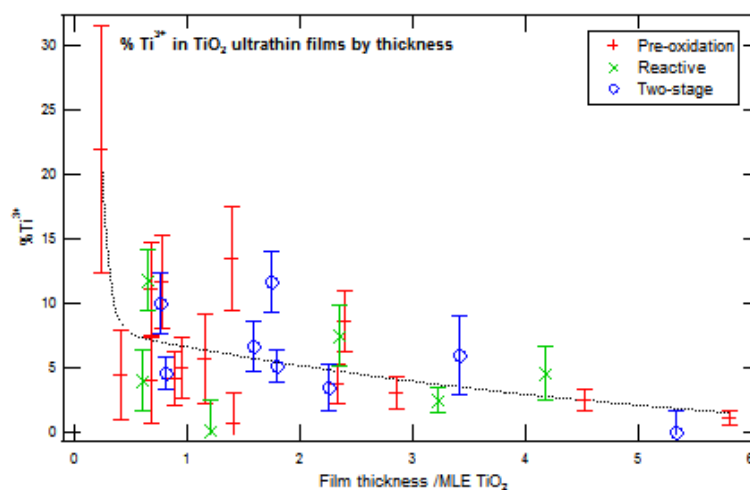
Figure 5.7: Change in %Ti^{3+} concentration as a function of film thickness.

		Position /eV	FWHM (G) /eV	FWHM (L) /eV	FWHM (V) /eV
Ti^{4+}	$2p_{3/2}$	459.0	1.84	0.60	2.16
	$2p_{1/2}$	464.8	2.65	0.60	2.97
Ti^{3+}	$2p_{3/2}$	457.1	1.88	0.60	2.20
	$2p_{1/2}$	462.5	2.68	0.60	2.99
Ti^{2+}	$2p_{3/2}$	455.4	1.90	0.60	2.22
	$2p_{1/2}$	460.8	2.70	0.60	3.02

Table 5.1: Parameters used in Ti $2p$ fitting procedure, showing peak position, and Gaussian (G), Lorentzian (L) and Voigt (V) full-width at half-maximum (FWHM) values.

Indeed, thicker films (> 5 MLE TiO$_2$(110)) were almost stoichiometric with only $\sim 1\%$ Ti^{3+} states present.

O 1s XPS Spectra   Deconvolution of the O 1s XPS spectra reveals two contributions (figure 5.8), one centred around a binding energy of 530.4 eV which corresponds to oxygen in the bulk below the surface layer, and a satellite peak, denoted S$_1$ shifted $+1.4$ eV from the main peak (fitting parameters shown in table 5.2). The S$_1$ contribution, expressed as a percentage of the total O 1s XPS peak area, was greater in films < 1 MLE TiO$_2$ thick, and for films > 1 MLE TiO$_2$ thick the contribution accounts for roughly 26.6% of the O 1s XPS peak area (figure 5.9). This suggests that the species responsible for S$_1$ is found in the surface layer (since in thicker films, the signal from the main O 1s XPS peak was stronger). There is ambiguity in the literature surrounding the assignment of S$_1$, and further discussion is made below in section 5.4.2 with reference to the reactivity of TiO$_2$ with H$_2$O.

The Substrate-Film Interface   The nature of the substrate-film interface can be investigated by comparison of the W 4d XPS spectra for different stages of the growth process [25]. Upon adsorption of oxygen, a slight broadening of the W 4d XPS peaks at higher binding energy occurs compared with the clean surface (figure
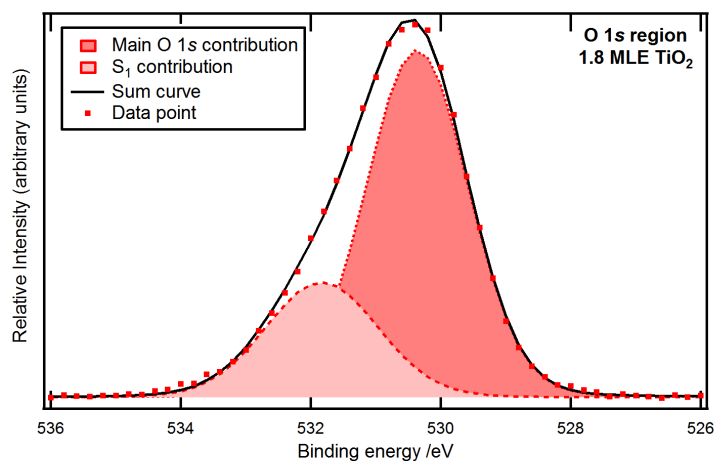
Figure 5.8: XPS Spectrum of the O 1s region for a 1.8 MLE thick TiO$_2$ film grown using the pre-oxidised W(100) method, showing contributions from the main O 1s XPS peak and the satellite, S$_1$. S$_1$ accounts for 26.66% of the total O 1s XPS peak area. A Shirley background has been subtracted, $h\nu = 1253.6$ eV.
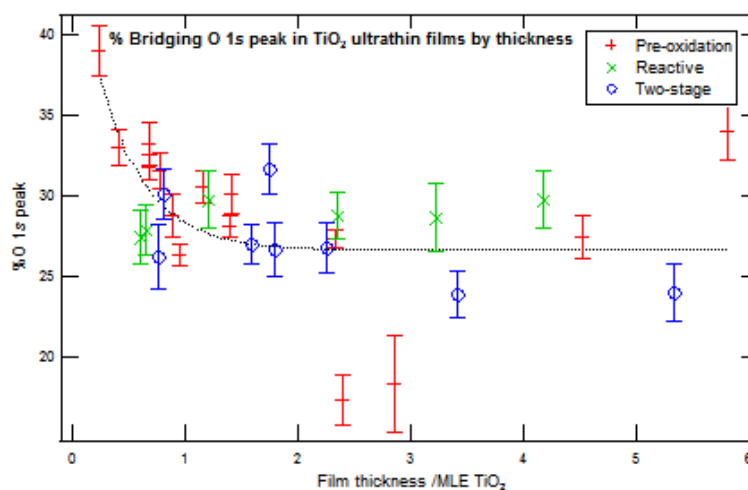
Figure 5.9: Change in the percentage contribution of the S$_1$ O 1s satellite peak with film thickness.
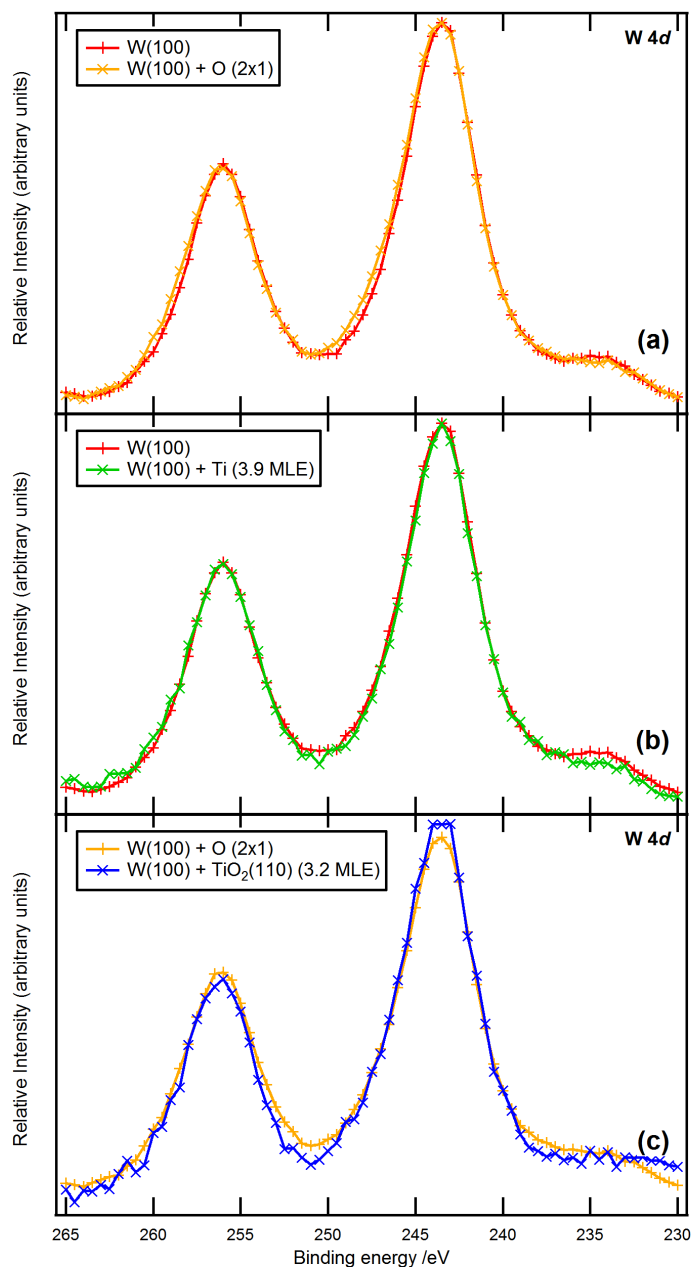
Figure 5.10: Comparison of the W 4d XPS spectra for (a) W(100) and W(100)-(2×1)-O surfaces, (b) W(100) and Ti-deposited (3.9 MLE Ti) W(100) surfaces, and (c) W(100)-(2 × 1)-O surface and a fully oxidised TiO₂(110) thin film on W(100) (grown using the two-stage method). Shirley backgrounds subtracted and spectra normalised to the same maximum intensity, $h\nu = 1253.6$ eV.

	Position /eV	FWHM (G) /eV	FWHM (L) /eV	FWHM (V) /eV
Main O 1s XPS peak	530.4	1.27	0.70	1.66
S$_1$	531.8	1.36	0.70	1.75

Table 5.2: Parameters used in O 1s fitting procedure, showing peak position, and Gaussian (G), Lorentzian (L) and Voigt (V) full-width at half-maximum (FWHM) values.

5.10(a)). Streaking along the (1×1) axes was also observed in the LEED pattern, with sufficient exposure to oxygen this sharpens to a (2×1) pattern [65]. There was no apparent change in the W 4d XPS spectra of the clean W(100) surface and a Ti-deposited W(100) surface (figure 5.10(b)). The W 4d spectrum for a fully oxidised TiO₂(110) film on W(100) shows peaks with similar widths to those for the oxidised W(100) surface (figure 5.10(c)). The difference in appearance of W 4d spectra, particularly in the satellite at low E_B is caused by attenuation due to overlayers in (b) and (c).

5.3.2　Interaction with H₂O

TiO₂ thin films prepared by the pre-oxidised W(100) method were exposed to $\leq$ 200 L H₂O in stages at 293 K. After each stage, the Ti 2p and O 1s regions were examined. No change was observed in the LEED pattern, aside from attenuation of spots indicating adsorption without long range order.

Stoichiometry changes

Changes in the stoichiometry of films upon H₂O exposure were monitored by the Ti 2p XPS spectra. Changes in the Ti 2p states are shown for three of the films, with thicknesses of 0.9 MLE TiO₂ (figure 5.11(a-c)), 1.4 MLE TiO₂ (figure 5.12(a-c)) and 5.3 MLE TiO₂ (figure 5.13(a-c)). In each case, there was an increase in
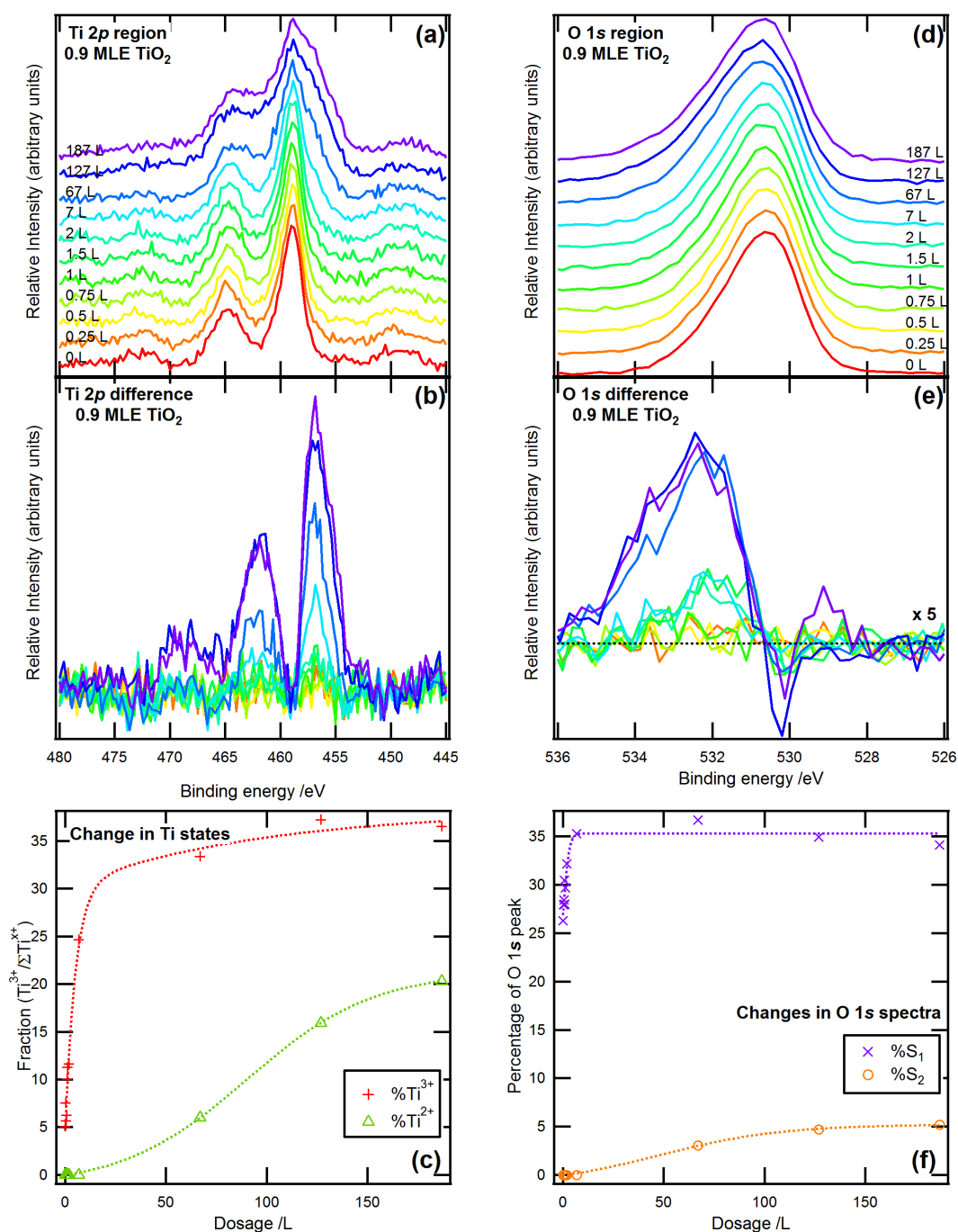
Figure 5.11: 0.9 MLE TiO₂ thin film (pre-oxidised growth) exposed to 187 L H₂O: (a) Ti 2*p* XPS spectra (Shirley backgrounds subtracted) at each exposure, normalised to the same maximum intensity, (b) difference spectra showing changes compared with the film prior to H₂O exposure, (c) change in %Ti³⁺ versus H₂O exposure, (d) O 1*s* XPS spectra (Shirley backgrounds subtracted) at each exposure, normalised to the same maximum intensity, (e) difference spectra showing changes compared with the film prior to H₂O exposure, (f) change in %S₁ O 1*s* signal versus H₂O exposure. $h\nu = 1253.6$ eV.
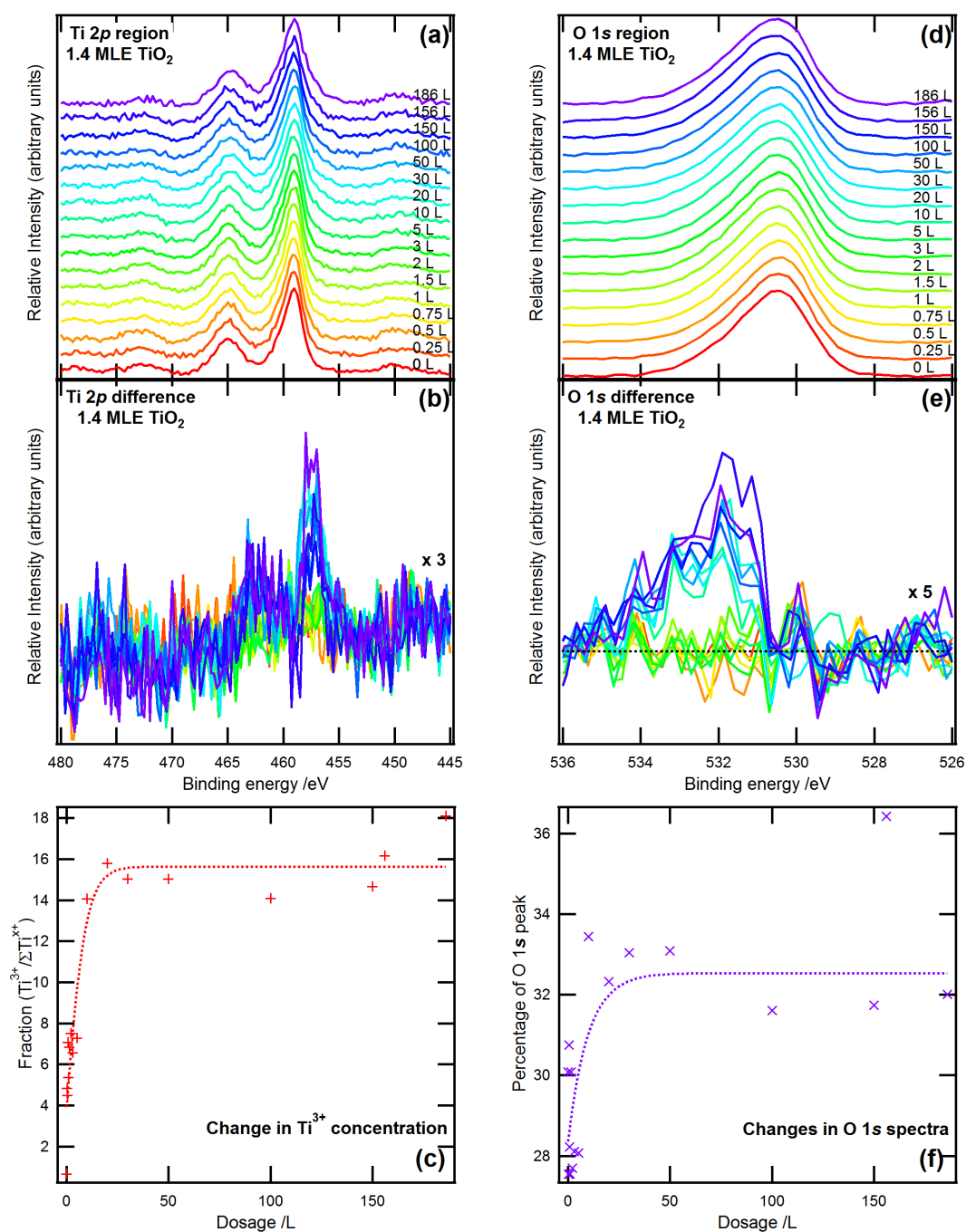
Figure 5.12: 1.4 MLE TiO₂ thin film (pre-oxidised growth) exposed to 186 L H₂O:(a) Ti 2*p* XPS spectra (Shirley backgrounds subtracted) at each exposure, normalised to the same maximum intensity, (b) difference spectra showing changes compared with the film prior to H₂O exposure, (c) change in %Ti³⁺ versus H₂O exposure, (d) O 1*s* XPS spectra (Shirley backgrounds subtracted) at each exposure, normalised to the same maximum intensity, (e) difference spectra showing changes compared with the film prior to H₂O exposure, (f) change in %S₁ O 1*s* signal versus H₂O exposure. $h\nu = 1253.6$ eV.
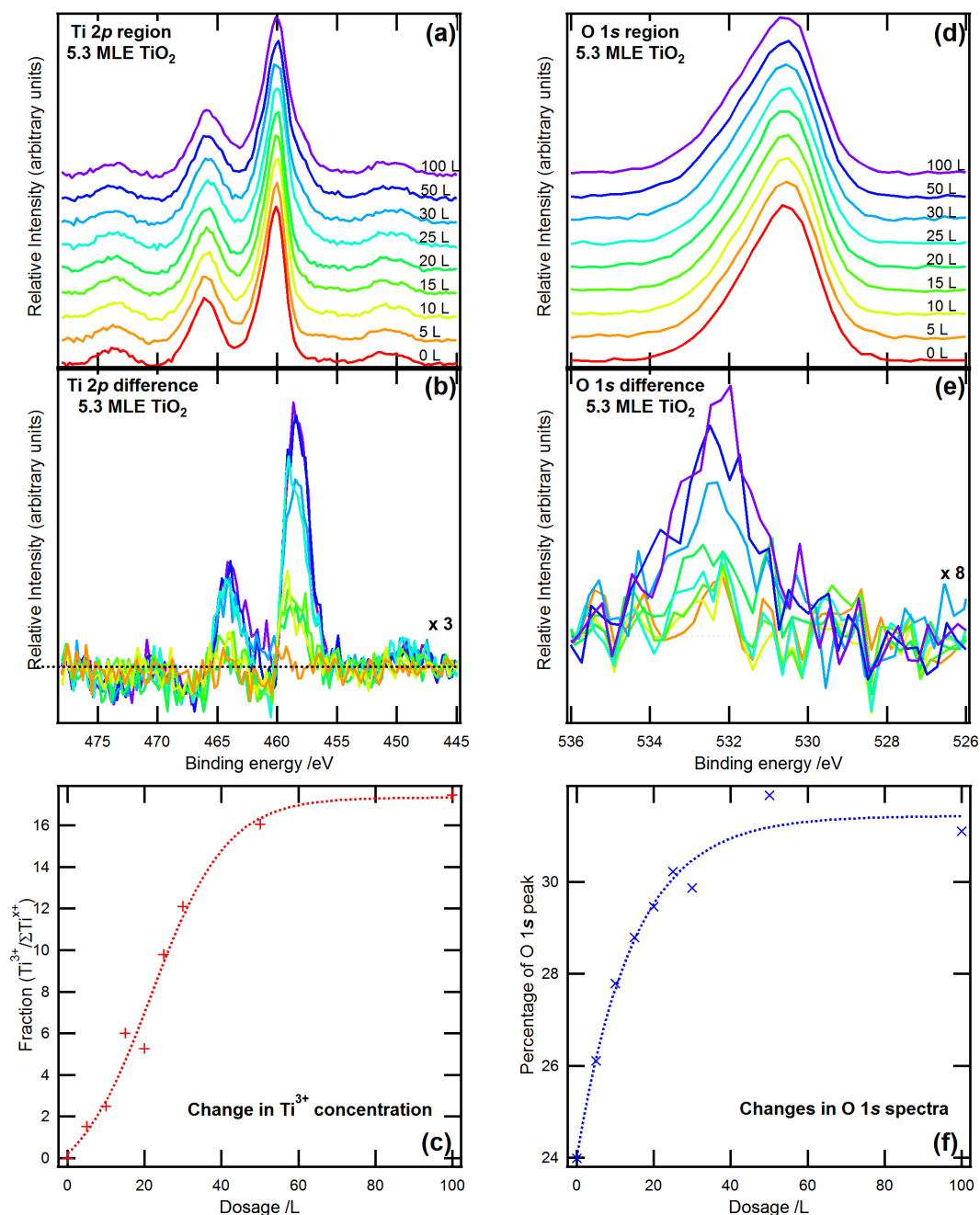
Figure 5.13: 5.3 MLE TiO$_2$ thin film (pre-oxidised growth) exposed to 100 L H$_2$O:(a) Ti 2p XPS spectra (Shirley backgrounds subtracted) at each exposure, normalised to the same maximum intensity, (b) difference spectra showing changes compared with the film prior to H$_2$O exposure, (c) change in %Ti^{3+} versus H$_2$O exposure, (d) O 1s XPS spectra (Shirley backgrounds subtracted) at each exposure, normalised to the same maximum intensity, (e) difference spectra showing changes compared with the film prior to H$_2$O exposure, (f) change in %S$_1$ O 1s signal versus H$_2$O exposure. $h\nu = 1253.6$ eV.
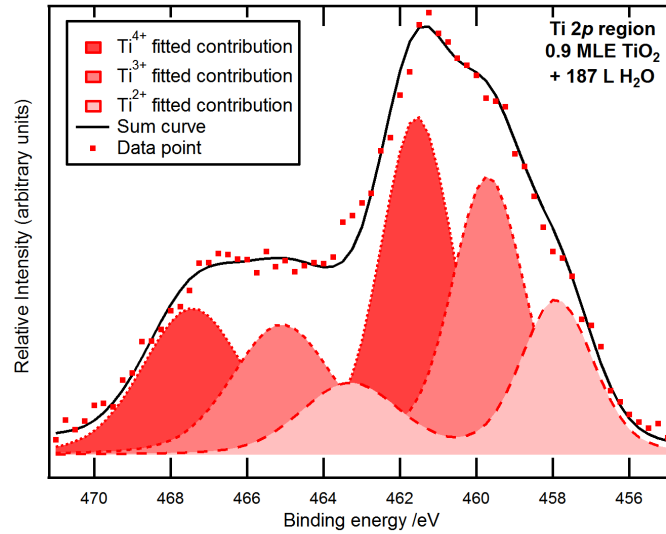
Figure 5.14: Ti 2p XPS spectrum showing contributions from Ti^{2+}, Ti^{3+} and Ti^{4+} ions in a 0.9 MLE TiO$_2$ film (pre-oxidised growth) exposed to 187 L H$_2$O, as estimated by fitting with three Voigt doublets. Ion concentrations were 20.3% Ti^{2+} and 36.5% Ti^{3+}. A Shirley background has been subtracted, $h\nu$=1253.6 eV

.

non-stoichiometry.

In figure 5.11(a), increases on the lower E_B side of both peaks of the thinnest film are apparent. Figure 5.11(b) shows the difference of each stage minus the scan for 0 L exposure. Up to 7 L H$_2$O exposure a doublet with peaks at 458.1 eV and 463.5 eV appears, corresponding to Ti^{3+} states. Above this exposure, the difference doublet peak gains some asymmetry to lower E_B. This can be fitted with another doublet with peaks at 455.4 eV and 460.8 eV and suggests the presence of Ti^{2+} states [66] (a fit is shown in figure 5.14). By peak fitting and comparing peak areas, the %Ti^{3+} and %Ti^{2+} states can be calculated. Plotting these values against exposure (figure 5.11(c)) shows a sigmoidal increase in %Ti^{3+}, nearing a maximum at 37.2% Ti^{3+} after 100 L exposure. A shallower sigmoidal increase to a maximum of 20.3% Ti^{2+} was observed, with Ti^{2+} states not present below 7 L exposure.

In thicker films (figures 5.12 and 5.13), no Ti^{2+} states were observed, although it is

possible that in the case of the 1.4 MLE TiO$_2$(110) film the Ti^{2+} signal is lost behind noise. An increase was still observed on the lower E_B side of the Ti 2p XPS peaks, more obviously on the 2$p_{3/2}$ peak (figures 5.12(a) and 5.13(a)). The doublet peak appearing in difference spectra is more symmetric and can be fitted with a single doublet with peaks at 458.1 eV and 463.5 eV appears corresponding to Ti^{3+} states (figures 5.12(b) and 5.13(b)). The increase in %Ti^{3+} states was again sigmoidal, with maxima of 14.6% Ti^{3+} at 30 L for the 1.4 MLE TiO$_2$ thick film, and 17.5% at 60 L for the 5.3 MLE TiO$_2$ thick film.

Changes in O 1s XPS peak

Changes in the O 1s XPS spectra were also monitored and are shown for the same 3 films: 0.9 MLE TiO$_2$ (figure 5.11(d-f)), 1.4 MLE TiO$_2$ (figure 5.12(d-f)) and 5.3 MLE (figure 5.13(d-f)).

For the 0.9 MLE TiO$_2$ film, an increase at higher E_B was observed on increasing H$_2$O exposure (figure 5.11(d)). This increase is more apparent in the difference spectra of each scan minus the scan for 0 L H$_2$O exposure (figure 5.11(e)). Peak fitting of the XPS spectra indicates the presence of a second satellite, denoted S$_2$ at +2.6 eV above the main O 1s XPS peak for exposures of over 7 L H$_2$O exposure. An increase to a maximum was observed in S$_1$ peak area as a percentage of the whole O 1s area, to a maximum value of 35.0%. Above 7 L, the S$_2$ signal also increases to a maximum value of 8.6%.

An increase at higher E_B to the main O 1s XPS peak was also observed for the 1.4 MLE TiO$_2$ (figure 5.12(d)) and 5.3 MLE TiO$_2$ (figure 5.13(d)) films. However, on peak fitting there was no evidence for the presence of S$_2$. The increase shown in difference spectra (figure 5.12(e) and figure 5.13(e)) is an increase in the S$_1$ satellite. Values increased until maxima were reached at 31.7% at 30 L for the 1.4 MLE film and 31.4% at 40 L.

TiO$_2$ thickness /MLE	Initial %Ti^{3+}	Initial %S$_1$	Saturation %Ti^{3+}	Saturation %S$_1$
0.9	5.0	26.3	37.2	35.0
1.4	0.7	30.1	14.7	31.7
1.6	6.6	27.0	15.3	29.4
4.2	4.5	29.7	15.3	32.6
5.3	0.0	24.0	17.5	31.1

Table 5.3: Summary of initial and saturation values for %Ti^{3+} and %S$_1$ for TiO$_2$ ultrathin films of varying thickness.

Initial and saturation values of %Ti^{3+} and %S$_1$ for the films are tabulated in table 5.3.

Interaction between hydroxylated TiO$_2$(110) and O$_2$

Following exposure to H$_2$O, films were again annealed at 800 K in 1 $\times 10^{-7}$ mbar O$_2$. Figure 5.15(a) shows the change in Ti 2p states after 5 and 10 min anneals. After 5 min all Ti^{3+} states have been removed and the Ti 2p spectrum resembles that of the spectrum prior to H$_2$O exposure. Similarly, figure 5.15(b) shows the change in O 1s XPS spectra after annealing. The %S$_1$ area was 25.0% after 10 min anneal, close to the %S$_1$ for the film prior to H$_2$O exposure.

Interaction between W(100) and H$_2$O

H$_2$O was exposed up to 100 L on a clean, bare W(100) surface to examine any interaction. Although studies are few, it has been reported that H$_2$O acts as an oxidising agent on W(100) at room temperature - H$_2$O molecules adsorb dissociatively, with O atoms diffusing into the W(100) to form an oxide and H escaping as an element [82]:

$$W + 2H_2O \longrightarrow WO_2 + 2H_{2(g)} \qquad (xix)$$
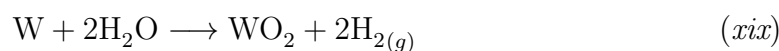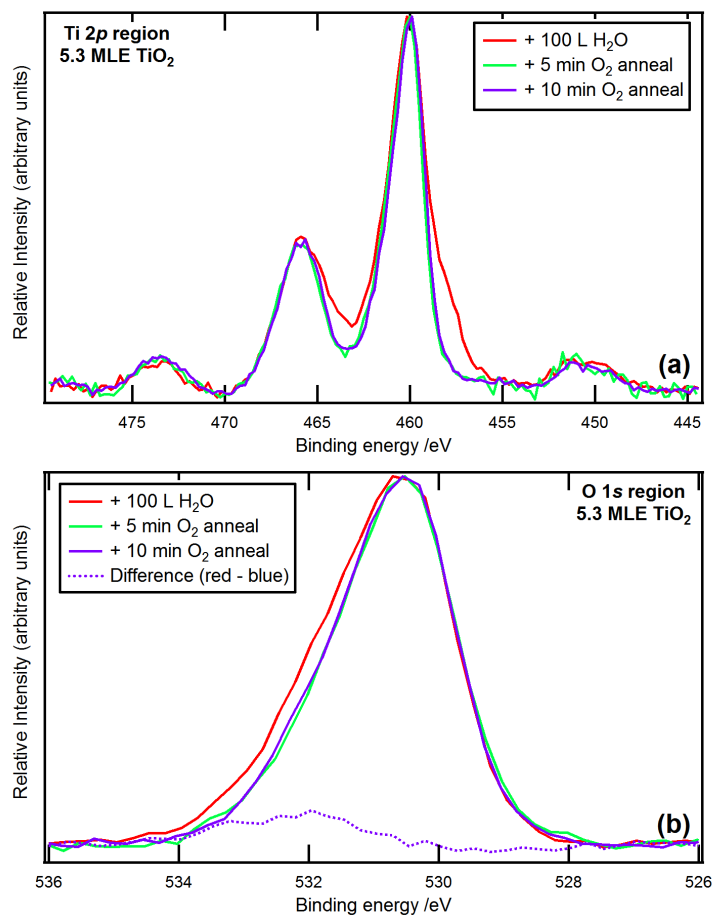
Figure 5.15: XPS spectra of (a) the Ti 2p region and (b) the O 1s region showing the change on annealing in O$_2$ after exposure to 100 L H$_2$O to a 5.3 MLE TiO$_2$ thin film. Shirley backgrounds have been subtracted, $h\nu = 1253.6$ eV.
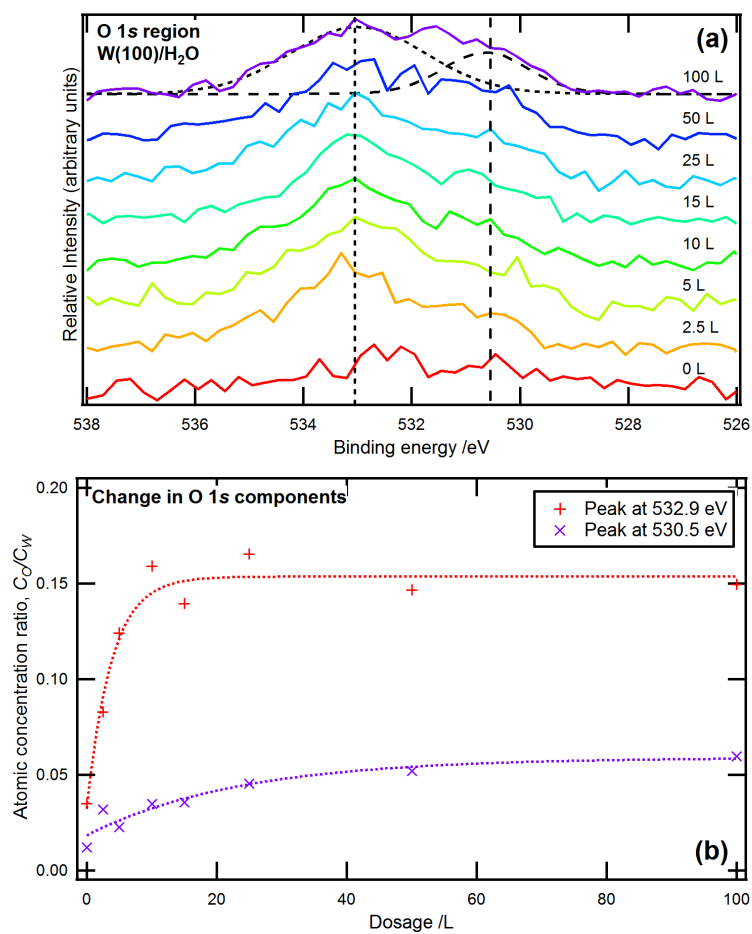
Figure 5.16: (a) XPS spectra of the O 1*s* region for W(100) exposed to H₂O (Shirley backgrounds have been subtracted, $h\nu = 1253.6$ eV), (b) changes in O 1*s* components on exposure to H₂O.

$$W + 3H_2O \longrightarrow WO_3 + 3H_{2(g)} \qquad\qquad (xx)$$

$$WO_3 + xH_2O \longrightarrow WO_3 \cdot xH_2O \qquad\qquad (xxi)$$
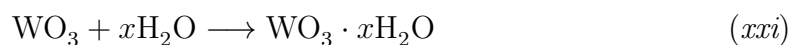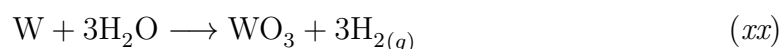
Figure 5.16(a) shows the changes in O 1s XPS spectra as exposure increases. Even with very thorough cleaning procedures, a trace amount of O was present on the clean surface (peak at 530.5 eV). The intensity of this peak increases to a maximum on exposure to H$_2$O. The O 1s XPS peak can be fitted with two Voigt singlet peaks at 530.5 eV and 532.9 eV. Using the area of these peaks and the area under the W 4d XPS spectra, the change in atomic concentration of both species was seen to increase (figure 5.16(b)) to a saturation limit of 0.15 for the peak at 532.9 eV and 0.06 for the peak at 530.5 eV.

The C 1s line was monitored at all stages throughout film growth and H$_2$O exposure, and at all stages its intensity was below the level of detection.

5.4   Discussion

5.4.1   Ultrathin films

The similarity in final Ti 2p and O 1s XPS spectra for each of the growth mechanisms used suggests that films produced by each mechanism were equivalent. At the temperature at which the films were annealed (800 K), oxygen can diffuse through TiO$_2$ [76] and films can be completely oxidised regardless of initial conditions at the substrate interface. LEED data indicate that there was no order in Ti deposited on W(100) surfaces, but that ordered films result post-oxidation. LEED patterns were

clearer for thicker films since there is less substrate influence and less strain in the films.

The slight non-stoichiometry exhibited, which decreases with increasing film thickness is likely due to charge transfer from the substrate to interfacial Ti or the presence of Ti interstitials. Non-stoichiometry can also result from surface defects such as O_{vac}. The W $4d$ spectrum of the W(100)/TiO$_2$(110) interface resembles the same spectrum for oxidised W(100), indicating that the substrate-film interface is made by O atoms rather than Ti.

5.4.2   Interaction with H$_2$O

The increase in Ti^{3+} states on exposure to H$_2$O suggests dissociation on the TiO$_2$ surface. As previously outlined, H$_2$O molecules adsorbed at O_{vac} dissociate leaving an adsorbed OH_b and an additional H atom, which combines with another O_b and forms a second OH_b (illustrated in reaction (xi)). Thus for every O_b converted to a OH_b, an additional Ti$^3+$ state is created [36]. The precise nature of charge distribution, transport and origin throughout this reaction is a complex issue not fully resolved in the literature [77]. O_{vac} sites repel each other by redistribution along O_b rows likely due to excess charge, although low temperature STM scans of filled states suggest that charge is not located on O_{vac} but rather on the next two Ti$_{5c}$ sites adjacent to the Ti$_{5c}$ site neighbouring O_{vac} [78]. Resonant photoemission diffraction experiments corroborate this conclusion [79]. Moreover, it has been observed that ∼90% of all H migrations along O_b rows are from OH_b groups next to the original O_{vac}, suggesting that the environment around geminate OH_b groups is different [49]. Further investigation using techniques capable of determining local electronic structure (such as low temperature STM) is required.

Ti^{2+} states were only present in the exposure of H$_2$O to the 0.9 MLE TiO$_2$ thick film. Since the film was < 1 MLE thick, it is likely that with the surface not completely

saturated with TiO_2, there is space for mobility of adsorbates and thus the formation of lower ordered oxides such as TiO.

An additional consideration is that for thin film metal oxides the substrate essentially acts as an infinitely large electron reservoir and below a critical film thickness can donate electrons to electropositive adsorbates or accept electrons from electronegative adsorbates. Additionally, the substrate can enhance the van der Waals forces felt by adsorbates on thin film surfaces [80, 81]. This is the likely cause of the largest change occurring in the thinnest films, where screening from the film is less.

From table 5.3, it appears that the saturation values of $\%Ti^{3+}$ increase for films over 1 MLE TiO_2 thick. However, this value never exceeds the percentage of all Ti ions in the top layer of the film. Thus, it is concluded that reaction with H_2O only affects the surface (top layer) of films.

There is ambiguity in the literature regarding the assignment of the contributions S_1 and S_2 in the O 1s XPS spectra. A peak at +2.40 eV from the main peak has been previously assigned as either OH_b [33, 69] or molecularly adsorbed water, $H_2O_{(a)}$ [71, 72, 74, 75]. The experiment with bare W(100) and H_2O sheds light on the S_2 peak, only observed for the 0.9 MLE $TiO_2(110)$ thick film. At room temperature, H_2O has been shown to oxidise the W(100) surface but also to hydrate WO_3 [82]. S_2 appears at a binding energy of 533.0 eV, similar to the second O 1s XPS peak observed on exposing a clean W(100) surface to H_2O. It can be concluded that this peak represents molecular H_2O adsorbed to regions of oxidised tungsten. Thus S_2 is only significant at low film coverages, where there is more chance of H_2O interaction with the substrate.

S_1 has previously been assigned to two-fold bridging oxygen atoms (O_b) on the $TiO_2(110)$ surface [33, 68–70]. However, recent studies have questioned this assignment and instead suggest that this peak was due to OH_b arising from reaction with residual water in the background vacuum [71–73]. In experiments presented here,

%S$_1$ increases to a maximum saturation value. As such it is suggested that S$_1$ must arise due to the presence of adsorbed hydroxyls, OH$_{(a)}$. The presence of S$_1$ prior to H$_2$O exposure is likely due to H$_2$O in the residual vacuum [72].

This assignment of S$_1$ and S$_2$ tallies with the present model of the H$_2$O adsorption/dissociation mechanism, as outlined in section 5.1.3. The absence of S$_2$ in thicker films corresponds with the accepted view that molecular H$_2$O does not adsorb to TiO$_2$(110) surfaces without dissociation at room temperature [42–44].

5.4.3 Interaction between hydroxylated TiO$_2$(110) and O$_2$

The electronegativity of TiO$_2$(110) surfaces is variable according to the degree of reduction, within the range 4.4-5.8 eV [83]. In the case of an adsorbate with lower electronegativity than the TiO$_2$(110) surface, such as H$_2$O there is negligible difference between adsorption on clean or defected surfaces. However, in the case where adsorbates have a higher electronegativity, such as O$_2$ the effect of an excess of electrons on the surface (when the surface is reduced) reduces the energy of adsorption compared with the perfect (defect-free) surface. Both density functional theory (DFT) calculations [84] and experimental evidence [85] have shown the equivalence of O$_{vac}$ and 2OH$_b$ on the TiO$_2$(110) surface in interactions with O$_2$ - one O$_{vac}$ and two OH$_b$ groups both donate 2 electrons to an O$_2$ adsorbate molecule [77]. The implication is that the same redox chemistry is possible regardless of the source of excess electrons. Therefore O$_2$ reacts with hydroxylated surfaces in much the same way as with reduced surfaces.

As outlined in section 5.1.4, O$_2$ reacts with OH$_b$ and ultimately replaces OH$_b$ with O$_b$ via reaction intermediates HO$_2$, OH$_t$ and O$_t$. The removal of excess electrons (from the OH$_b$ group) results in the conversion of Ti^{3+} to Ti^{4+} as observed by the Ti 2p XPS spectra after annealing in O$_2$.

Reaction (*xviii*) shows that H$_2$O is a product of the reaction between the hydroxylated TiO$_2$(110) surface and O$_2$. No signal for H$_2$O was observed in the O 1s XPS spectrum as might be expected, however this was because the temperature of the anneal (800 K) is well in excess of the desorption temperature for molecular H$_2$O. The S$_1$ peak remains evident in the spectrum after reaction with oxygen. However, since a depopulation of Ti^{3+} states was observed in the Ti 2p XPS spectrum, no OH$_b$ were expected to remain. Instead this S$_1$ contribution can be attributed to the presence of oxygen ad-atoms, O$_a$ which appear in XPS spectra at almost the same E_B as OH$_b$ [73].

5.5   Conclusions

Three methods of synthesising ultra-thin films of TiO$_2$(110) on a W(100) substrate have been investigated using XPS and LEED. These methods have been found to be equivalent and films of between 0.2-5.7 MLE have been synthesised. The reactivity of the TiO$_2$(110) surface has been examined by exposure to H$_2$O. XPS spectra of the Ti 2p and O 1s peaks show an increase in Ti^{3+} states and S$_1$ peaks, respectively, consistent with an increase in excess charge on the TiO$_2$(110) surface. Further evidence for the assignment of this S$_1$ peak - an O 1s satellite peak - as OH$_b$ has been provided. Molecular H$_2$O was not observed spectroscopically except for films of < 1 MLE TiO$_2$ thickness, where regions of exposed WO$_x$ were present and can be hydrated. A control experiment demonstrates that exposure of a clean W(100) surface to H$_2$O results in molecular adsorption. This is observed spectroscopically by a second satellite in the O 1s XPS spectrum, termed S$_2$ which is +2.6 eV from the principal O 1s peak. O$_2$ reacts with hydroxylated TiO$_2$(110) surfaces - specifically OH$_b$ (sources of excess charge) - replacing OH$_b$ with O$_b$ and causing a conversion of Ti^{3+} states to Ti^{4+}. This is observed in XPS spectra by the Ti 2p and O 1s spectra of O$_2$ reacted films resembling those of the same films before water exposure. The

exact nature, distribution and transport of excess charge on the TiO_2(110) surface remains undefined and further research using techniques to examine local electronic structure (such as low temperature STM of filled states) is required.

Although numerous studies of H_2O and O_2 adsorption on TiO_2(110) have been reported, only one other study has used thin films of TiO_2 (on Ni(110)) [72]. The findings of the present study compare favourably with experiments reported in the literature using bulk TiO_2(110) crystal, and demonstrate the validity of using thin films on W(100) as analogues of bulk TiO_2. Using thin films opens up the possibility of using other electron based surface science techniques. For instance, STM experiments could provide further information about the nature of H_2O adsorption and dissociation. Additionally, given the suitability of W(100) as a substrate for ultra-thin TiO_2(110) films it could be used in EPR experiments owing to its paramagnetic nature.

References

[1] Baumer, M., Freund, H.J.; *Prog. Surf. Sci.*, **1999**, *61*, 127

[2] Linsebigler, A.L., Lu, G.Q., Yates Jr., J.T.; *Chem. Rev.*, **1995**, *95*, 735

[3] Woodruff, D.P., ed.; *The Chemical Physics of Solid Surfaces, Vol. 9: Oxide Surfaces*, **2001**, Elsevier, London

[4] Diebold, U.; *Surf. Sci. Rep.*, **2003**, *48*, 53

[5] Kavan, L., Grätzel, M, Gilbert, S.E., Klemenz, C., Scheel, H.J.; *J. Am. Chem. Soc.*, **1996**, *118*, 6716

[6] Li, M., Hebenstreit, W., Diebold, U., Tyryshkin, A.M., Bowman, M.K., Dunham, G.G., Henderson, M.A.; *J. Phys. Chem. B*, **2000**, *104*, 4944

[7] Chambers, S.A.; *Surf. Sci.*, **2000**, *39*, 105

[8] Murray, P.W., Brookes, I.M., Haycock, S.A., Thornton. G.; *Phys. Rev. Lett.*, **1998**, *80*, 988

[9] Thornton, G.; *Science*, **2003**, *300*, 1378

[10] Campbell, C.T.; *Surf. Sci. Rep.*, **1997**, *27*, 1

[11] Henry, C.R.; *Surf. Sci. Rep.*, **1998**, *31*, 235

[12] Jaeger, R., Kuhlenbeck, H., Freund, H.-J., Wutig, M., Hoffman, W., Franchy, R., Iback, H.; *Surf. Sci.*, **1991**, *259*, 235

[13] Herman, G.S., Gallagher, M.C., Joyce, S.A., Peden, C.H.F.; *J. Vac. Sci. Tech. B*, **1996**, *14*, 1126

[14] Lai, X., Guo, Q., Min, B.K., Goodman, D.W.; *Surf. Sci.*, **2001**, *487*, 1

[15] Street, S.C., Xu, C., Goodman, D.W.; *Annu. Rev. Phys.*, **1997**, *48*, 43

[16] Grätzel, M.; *Nature*, **2001**, *409*, 575

[17] Finetti, P., Caffio, M., Cortigiani, B., Atrei, A., Rovida, G.; *Surf. Sci.*, **2008**, *602*, 1101

[18] Oh, W.S., Xu, C., Kim, D.Y., Goodman, D.W.; *J. Vac. Sci. Technol. A*, **1997**, *15(3)*, 1710

[19] Guo, Q., Oh, W.S., Goodman, D.W.; *Surf. Sci.*, **1999**, *437*, 49

[20] Kumar, D., Chen. M.S., Goodman, D.W.; *Thin Solid Films*, **2006**, *515*, 1475

[21] Ashworth, T.V., Thornton, G.; *Thin Solid Films*, **2001**, *400*, 43

[22] Ashworth, T.V., Muryn, C.A., Thornton, G.; *Nanotechnology*, **2005**, *16*, 3041

[23] Sedona, F., Llabrés i Xamena, F.X., Rizzi, G.A., Granozzi, G., Ostermann, D., Schierbaum, K.D.; *J. Phys. Chem. B*, **2005**, *109(51)*, 24411

[24] Männig, A., Zhao, Z., Rosenthal, D., Christmann, K., Hoster, H., Rauscher, H., Behm, R.J.; *Surf. Sci.*, **2005**, *576*, 29

[25] McCavish, N.D., Bennett, R.A.; *Surf. Sci.*, **2003**, *546*, 47

[26] Yamazaki, H., Kamisawa, T., Kokubun, T., Haga, T., Kamimizu, S., Sakamoto, K.; *Surf. Sci.*, **2001**, *477*, 174

[27] Yamazaki, H., Kamimuzu, S., Hara, K., Sakamoto, K.; *Surf. Sci.*, **2003**, *538*, L505

[28] Bennett, R.A., Mulley, J.S., Newton, M.A., Surman, M.; *J. Chem. Phys.*, **2007**, *127*, 084707

[29] Bennett, R.A., McCavish, N.D.; *Topics in Catalysis*, **2005**, *36*, 11

[30] Tengvall, P., Lundström, I.; *Clin. Mater.*, **1992**, *9*, 115

[31] Fujishima, A., Honda, K.; *Nature*, **1972**, *238*, 37

[32] Henrich, V.E., Dresselhaus, G., Ziegler, H.G.; *Solid State Commun.*, **1977**, *24*, 623

[33] Sham, T.K., Lazarus, M.S.; *Chem. Phys. Lett.*, **1979**, *68*, 426

[34] Eriksen, S., Naylor, P.D., Egdell, R.G.; *Spectrochimica Acta*, **1987**, *43A*, 1535

[35] Suda, Y., Morimoto, T.; *Langmuir*, **1987**, *3*, 786

[36] Kurtz, R.L., Stockbauer, R., Madey, T.E., Román, E., de Segovia, J.L.; *Surf. Sci.*, **1989**, *218*, 178

[37] Smith, P.B, Bernasek, S.L.; *Surf. Sci.*, **1987**, *188*, 241

[38] Bustillo, F.J., Roman, E., de Segovia, J.L.; *Vacuum*, **1990**, *41*, 19

[39] Muryn, C.A., Hardman, P.J., Crouch, J.J., Raiker, G.N., Thornton, G., Law, D.S.-L. Law; *Surf. Sci.*, **1991**, *251/252*, 747

[40] Pan, J.-M., Maschhoff, B.L., Diebold, U., Madey. T.E.; *J. Vac. Sci. Technol. A*, **1992**, *10(2)*, 2470

[41] Hugenschmidt, M.B., Gamble, L., Campbell, C.T.; *Surf. Sci.*, **1994**, *302*, 329

[42] Henderson, M.A.; *Surf. Sci.*, **1996**, *355*, 151

[43] Henderson, M.A.; *Langmuir*, **1996**, *12*, 5093

[44] Brookes, I.M., Muryn, C.A., Thornton, G.; *Phys. Rev. Lett.*, **2001**, *87*, 266103

[45] Bikondoa, O., Pang, C.L., Ithnin, R., Muryn, C.A., Onishi, H., Thornton, G.; *Nat. Mater.*, **2006**, *5*, 189

[46] Zhang, Z., Bondarchuk, O., Kay, B.D., White, J.M., Dohnálek, Z.; *J. Phys. Chem. B*, **2006**, *110*, 21840

[47] Pang, C.L., Sasahara, A., Onishi. H., Chen, Q., Thornton, G.; *Phys. Rev. B*, **2006**, *74*, 073411

[48] Wendt, S., Matthiesen, J., Schaub, R., Vestergaard, E.K., Lægsgaard, E., Besenbacher, F., Hammer, B.; *Phys. Rev. Lett.*, **2006**, *110*, 21840

[49] Li, S.-C., Zhang, Z., Sheppard, D., Kay, B.D., White, J.M., Du, Y., Lyubinetsky, I., Henkelman, G., Dohnálek, Z.; *J. Am. Chem. Soc.*, **2008**, *130*, 9080

[50] Wendt, S., Schaub, R., Matthiesen, J., Vestergaard, E. K., Wahlstroem, E., Rasmussen, M. D., Thostrup, P., Molina, L. M., Lægsgaard, E., Stensgaard, I., Hammer, B., Besenbacher, F.; *Surf. Sci.*, **2005**, *598*, 226

[51] Du, Y.G., Dohnálek, Z., Lyubinetsky, I.; *J. Phys. Chem. C*, **2008**, *112*, 2649

[52] Diebold, U., Lehman, J., Mahmoud, T., Kuhn, M., Leonardelli, G., Hebenstreit, W., Schmid, M., Varga, P.; *Surf. Sci.*, **1998**, *411*, 137

[53] Henderson, M.A., Epling, W.S., Perkins, C.L., Peden, C.H.F., Diebold, U.; *J. Phys. Chem. B*, **1999**, *103*, 5328

[54] Wendt, S., Sprunger, P.T., Lira, E., Madsen, G.K.H., Li, Z.S., Hansen, J.O., Matthiesen, J., Blekinge-Rasmussen, A., Lægsgaard, E., Hammer, B., Besenbacher, F.; *Science*, **2008**, *320*, 1755

[55] Henderson, M.A., Epling, W.S., Peden, C.H.F, Perkins, C.L.; *J. Phys. Chem. B*, **2003**, *107*, 534

[56] Epling, W.S., Peden, C.H.F., Henderson, M.A., Diebold, U.; *Surf. Sci.*, **1998**, *413*, 333

[57] Zhang, Z., Du, Y., Petrik, N.G., Kimmel, G.A., Lyubinetsky, I., Dohnálek, Z.; *J. Phys. Chem. C*, **2009**, *113*, 1908

[58] Du, Y., Deskins, N.A., Zhang, Z., Dohnálek, Z., Dupuis, M., Lyubinetsky, I.; *J. Phys. Chem. C*, **2009**, *113*, 666

[59] Tilocca, A., Di Valentin, C., Selloni, A.; *J. Phys. Chem. B*, **2005**, *109*, 20963

[60] Freund, H.-J., Pacchioni, G., *Chem. Soc. Rev.*, **2008**, *37*, 2224

[61] Grunze, M., Ruppender, H., Elshazly, O.; *J. Vac. Sci. Technol. A*, **1998**, *6*, 1266

[62] Vaquila, I., Passeggi Jr., M.C.G., Ferrón, J.; *Phys. Rev. B*, **1997**, *55*, 13925

[63] Doniach, S., Šunjić, M.; *J. Phys. C: Solid State Phys.*, **1970**, *3*, 285

[64] Thompson, A.C., Vaughan, D. (Eds.); *X-Ray Data Booklet, 2nd edition*, `http://xdb.lbl.gov/xdb.pdf`, **2001**, Lawrence Berkeley National Laboratory, University of California

[65] Bauer, E., Poppa, H., Viswanath, Y.; *Surf. Sci.*, **1976**, *58*, 517

[66] Siemensmeyer, B., Schultze, J.W.; *Surf. Interf. Anal.*, **1990**, *16*, 309

[67] Sayers, C.N., Armstrong, N.R.; *Surf. Sci.*, **1978**, *77*, 301

[68] Göpel, W.; *Surf. Sci.*, **1984**, *139*, 333

[69] Bullock, E.L., Patthey, L., Steinemann, S.G.; *Surf. Sci.*, **1996**, *352-354*, 504

[70] Cardenas, J., Sjöberg, S.; *Surf. Sci.*, **2003**, *532-535*, 1104

[71] Wang, X.-P., Yu, Y., Hu, X.-F., Gao, L.; *Thin Solid Films*, **2000**, *371*, 148

[72] Papageorgiou, A.C., Cabailh, G., Chen, Q., Resta, A., Lundgren, E., Andersen, J.N., Thornton, G.; *J. Phys. Chem. C*, **2007**, *111*, 7704

[73] Lindsay, R., Allegretti, F., Skála, T., Libra, J., Šutara, F., Matolín, V.; *Submitted for publication*, **2010**

[74] Henderson, M.A.; *Surf. Sci. Rep.*, **2002**, *46*, 1

[75] Allegretti, F., O'Brien, S., Polcik, M., Sayago, D.I., Woodruff, D.P.; *Phys. Rev. Lett.*, **2005**, *95*, 226104

[76] Mayer, J.T., Diebold, U., Madey, T.E., Garfunkel, E.; *J. Elect. Spect. Rel. Phenom.*, **1995**, *73*, 1

[77] Dohnálek, Z., Lyubinetsky, I., Rousseau, R.; *Prog. Surf. Sci.*, **2010**, *85*, 161

[78] Minato T., Sainoo, Y., Kim, Y., Kato, H.S., Aika, K., Kawai, M., Zhao, J., Petek, H., Huang, T. He, W., Wang, B., Wang, Z., Zhao, Y., Yang, J.L., Hou, J.G.; *J. Chem. Phys.*, **2009**, *130*, 124502

[79] Kruger, P., Bourgeois, S., Domenichini, B., Magnan, H., Chandesris, D., Le Fevre, P., Flank, A.M., Jupille, J., Floreano, L., Cossaro, A., Verdini, A., Morgante, A.; *Phys. Rev. Lett.*, **2008**, *100*, 055501

[80] Nilius, N.; *Surf. Sci. Rep.*, **2009**, *64*, 595

[81] Giordano, L., Baistrocchi, M., Pacchioni, G.; *Phys. Rev. B*, **2005**, *72*, 115403

[82] Lassner, E., Schubert, W.-D.; *"Tungsten: Properties, Chemistry, Technology of the element, Alloys and Chemical Compounds"*, **1999**, New York; Springer

[83] Onda, K., Li, B., Petek, H.; *Phys. Rev. B*, **2004**, *70*, 045415

[84] Deskins, N.A., Rousseau, R., Dupuis, M.; *J. Phys. Chem. C*, **2010**, *114*, 5891

[85] Petrik, N.G., Zhang, Z.R., Du, Y.G., Dohnlek, Z., Lyubinetsky, I., Kimmel, G.A.; *J. Phys. Chem. C*, **2009**, *113*, 12407

Chapter 6

Imaging TiO$_2$ ultra-thin films on W(100): an STM study of growth and thickness effects

6.1 Introduction

In the previous chapter, the growth and reactivity of ultrathin TiO$_2$(110) films grown on W(100) were studied using XPS. This revealed information about the spatially averaged chemical and electronic changes that take place in terms of surface stoichiometry and presence of different adsorbate species. In this chapter, STM is used to investigate the growth and structure of films as a function of film thickness.

6.1.1 Imaging the TiO$_2$(110) surface

The structure of the TiO$_2$(110) surface is described in chapter 5. Early STM studies largely ignored metal oxides in favour of more easily probed metals and semiconduc-

tors. The first attempts at imaging TiO$_2$ using STM were complicated by ambiguity over the contrast of images [1–3]. Initially, heavily reduced bulk crystal samples were used to allow sufficient conductivity for tunnelling, however the resulting high defect concentration gave rise to a number of different surface structures [2,3]. Images of less reduced TiO$_2$(110) surfaces that had produced sharp (1 × 1) LEED patterns showed a structure consistent with the expected (1 × 1) surface structure, with terraces separated by 3.2 Å along the [111] and [100] directions, and rows separated by 6.5 Å in the [001] direction [4]. Fischer et al assigned light rows to O$_b$ and the dark rows to Ti$_{5c}$, corresponding to the true surface topography [5]. However, pseudopotential calculations of the electronic states in the surface showed the reverse - that in fact the dark rows correspond to O$_b$ and the light rows to Ti$_{5c}$ [6]. This is now the accepted interpretation and thus STM images the local density of states (LDOS) rather than the morphology of TiO$_2$ [7].

6.1.2   STM of thin metal oxide films

Since bulk metal oxide crystal surfaces require treatment to induce sufficient conductivity for study using charged particle probes (such as STM), the use of thin, electron transparent films grown on metallic substrates presents a suitable alternative [8]. STM is possible even on films of thickness up to 100 Å, although the tunnelling characteristic follows different rules to those for metallic samples [1]. In particular, the contribution from spatially varying electronic properties may appear larger. At low bias, the apparent morphology of thin metal oxide films may be completely governed by the substrate-film interface. Similarly, at a bias close to the onset of the conduction or valence bands in the metal oxide, a new contrast may develop in images which may have no topographic origin [8].

STM images of TiO$_2$ thin films grown on Mo(100) [9], Mo(112) [10], Ni(110) [11–13], Ru(0001) [14], Pt(111) [15], Cu(001) [16] and W(100) [17] have been reported. The
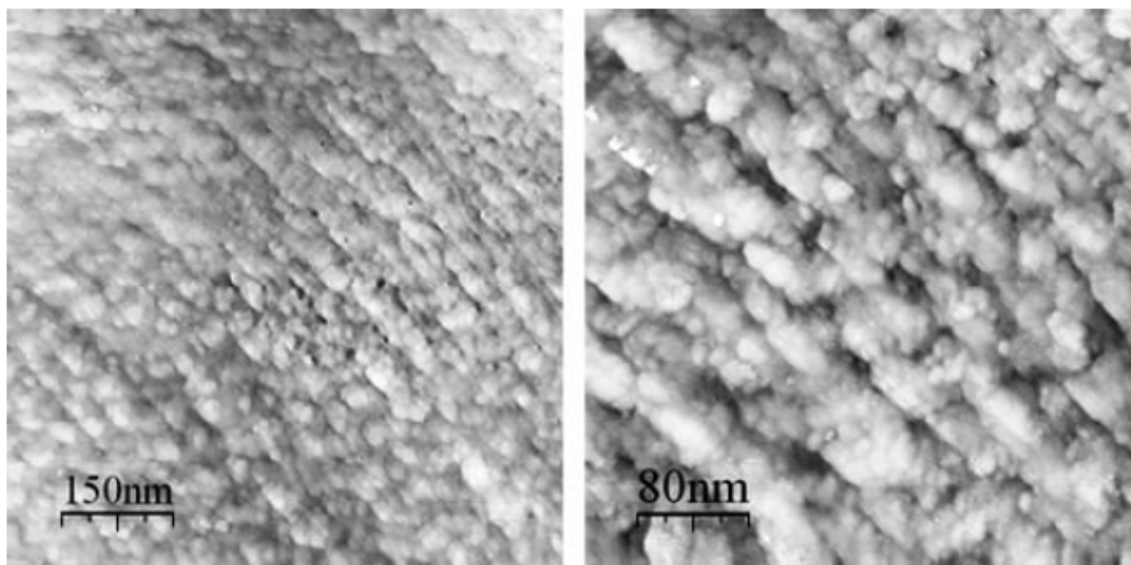
Figure 6.1: *Ex situ* STM images of a 4 MLE TiO$_2$(110) film grown on W(100). The film is quite flat and islands are aligned in the same direction. [17]

thickness of these films range from the submonolayer regime, through single mono-layer thickness to multilayer thickness. The unit cell of very thin films is observed to contract, with relaxation increasing with thickness [11]. Atomic resolution is possible and defect states can be imaged.

Here, W(100) is used as a substrate to grow TiO$_2$(110) thin films based on an established procedure [17–19]. Annealing W(100) in O$_2$ leads to a reconstructed W(100)-(2 × 1)-O surface with a unit cell of 6.49 × 2.96 Å. This is a close epitaxial match with TiO$_2$(110) which has a unit cell of 6.32 × 3.16 Å, a 2.7% × −6% mismatch. The only previously published STM images of this system were recorded *ex situ*, and show the growth of elongated structures [17] (figure 6.1). However, the resolution of these images was only sufficient to discern the rough morphology of the surface.

6.1.3   The W(100)-(2×1)-O surface

Chemisorption on the W(100) surface has been extensively studied since the 1970s, although these studies have been mainly concerned with low coverage ($\sim$0.5 ML) [20]. Exposure of a clean W(100) face to O$_2$ at 1050 K causes several transitions in the LEED pattern, the first of which results in a p(2×1) pattern [21]. STM of W(100) with atomic resolution is facile. The W(100)-(2×1)-O reconstructed surface has been imaged previously, with light and dark rows that correspond to topographic structure [22].

6.1.4   Objectives

Building on the findings of chapter 5, ultrathin films of TiO$_2$(110) will be grown on W(100) and characterised using STM, AES and LEED. The very high annealing temperatures required to remove O from W(100) are not possible with the STM instrument used, so films grown on pre-oxidised W(100) (as reported in chapter 5) will be investigated. STM will be used to gather information regarding Ti adsorption, the W(100) substrate surface and the growth and final morphology of TiO$_2$(110) films.

6.2   Experimental

Experiments were conducted using the VT-STM (as described in chapter 3) at UCL. This system is dual-chambered with a fast entry load lock. The base pressure in both chambers is $\leq 1 \times 10^{-10}$ mbar. The system is equipped with the necessary instruments for sample preparation - ion sources and LEED/AES optics, and manipulator arms capable of sample heating. A commercial VT-STM manufactured by *Omicron Vakuumphysik, GmbH* is fitted to the system, capable of scanning samples

at temperatures of 50-1100 K. All measurements presented here were recorded at ambient temperature (~ 293 K).

A W(100) crystal (*SPL*) was prepared first by Ar^+ sputtering and then by annealing in 1×10^{-7} mbar O_2 (*SIP Analytical*) to remove C [23]. The presence of C was monitored by AES, and the surface was considered clean when no C AES signal was detected above the noise level. Due to the technical limitations of the manipulator arm, the upper temperature limit did not allow for the complete removal of O from the W(100) surface by high temperature annealing. However, as shown previously in chapter 5, $TiO_2(110)$ films can be grown on a W(100)-O surface. The W(100) crystal was flashed to 1500 K and then annealed in 5×10^{-9} mbar O_2 at 1050 K, resulting in a (2×1) LEED pattern.

Ti was deposited on the W(100)-(2×1)-O reconstructed surface using a homebuilt e-beam Ti doser. This was calibrated by comparing the intensity ratios of the strongest AES peaks in the 100-600 eV region - W $N_5O_3O_3$ and Ti $L_3M_{2,3}M_{2,3}$ AES peaks at 169 and 387 eV, [24] respectively (figure 6.2). The breakpoint (as indicated by an arrow) indicates monolayer coverage. Full oxidation of the deposited Ti is achieved by annealing at 800 K in 1×10^{-7} mbar O_2 for 2 hrs.

Films were characterised by a composite of the W(100)(1×1) and $TiO_2(110)(1 \times 1)$ LEED patterns (as in chapter 5). Film thicknesses are estimated from the change in intensity of the W $N_5O_3O_3$ AES signal before and after film deposition, as described in appendix A.

All STM images were recorded at ambient temperature. Images were prepared using the *WSxM* software [25].
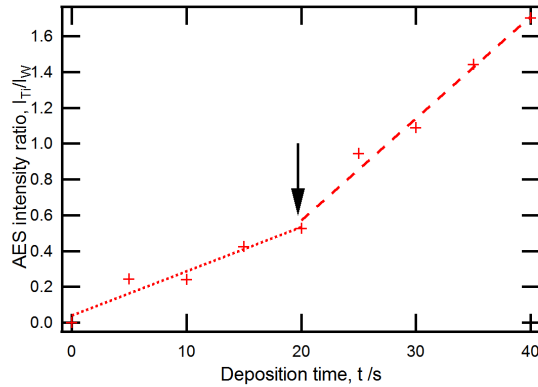
Figure 6.2: Calibration of the Ti doser was achieved by monitoring the intensity ratio, $I(\text{Ti } L_3M_{2,3}M_{2,3})/I(\text{W } N_5O_3O_3)$ in AES. The breakpoint is indicated by an arrow, corresponding to 1 ML Ti.

6.3 Results

6.3.1 Preparation of the W(100)-(2×1)-O surface

Following the cleaning cycles of annealing in O_2 and UHV and a final short O_2 anneal, the substrate surface appears to consist of small bumps on large, fairly flat, terraces in STM with a faint (2×1) LEED pattern (figure 6.3(a)). An AES spectrum of this surface shows no other elements present than W or O, within detection limits. A further 10 min UHV anneal to 1275 K appears to remove bumps, leaving flat terraces and a much sharper (2×1) LEED pattern (figure 6.3(b)).

A closer inspection of the surface (figure 6.4) shows alternate bright and dark rows, separated by 6.3 Å (red line profile). This is in line with reported STM of this surface [22], and the contrast of images corresponds to the true topography of the surface. Two domains exist, orientated 90° from each other, in approximately equal proportions.

The difference in height between terraces is ∼1 Å (figure 6.5(a) and (b)). Terraces are terminated in a ragged manner, and there is no clear preferences for terraces to
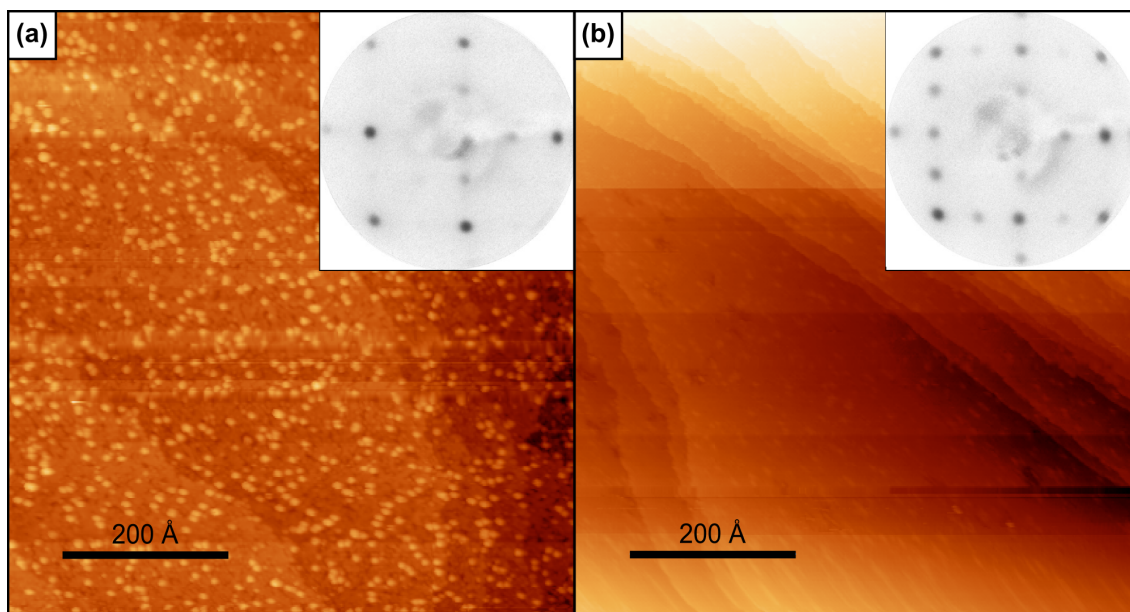
Figure 6.3: STM images of the preparation of a smooth W(100)-(2 × 1)-O surface. (a) STM image of a surface prepared by annealing in O$_2$ (image size 1000 × 1000 Å^2, V_{sample} = 2 V, I_F = 200 pA), inset LEED image showing a faint (2×1) pattern, E_{beam}=55 eV; (b) STM image of the same surface following a 10 min UHV anneal to 1275 K (image size 1000 × 1000 Å^2, V_{sample} = 2 V, I_F = 200 pA), inset LEED image showing a sharp (2×1) pattern, E_{beam}=55 eV.
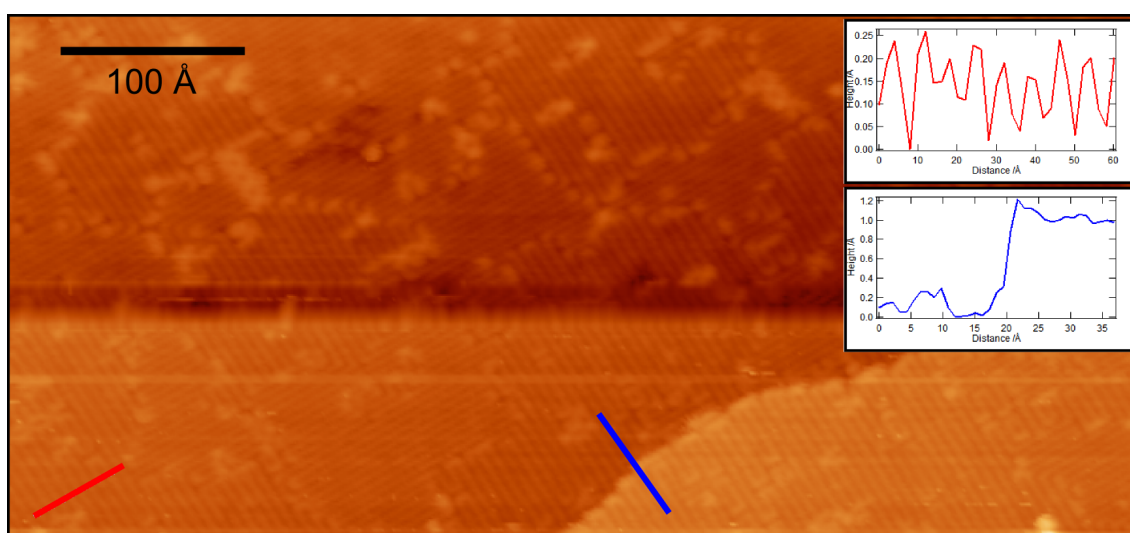
Figure 6.4: STM image showing row structure on the W(100)-(2 × 1)-O surface, with inset line profiles showing row separation and step height (image size 165 × 360 Å^2, V_{sample} = 2 V, I_F = 200 pA).
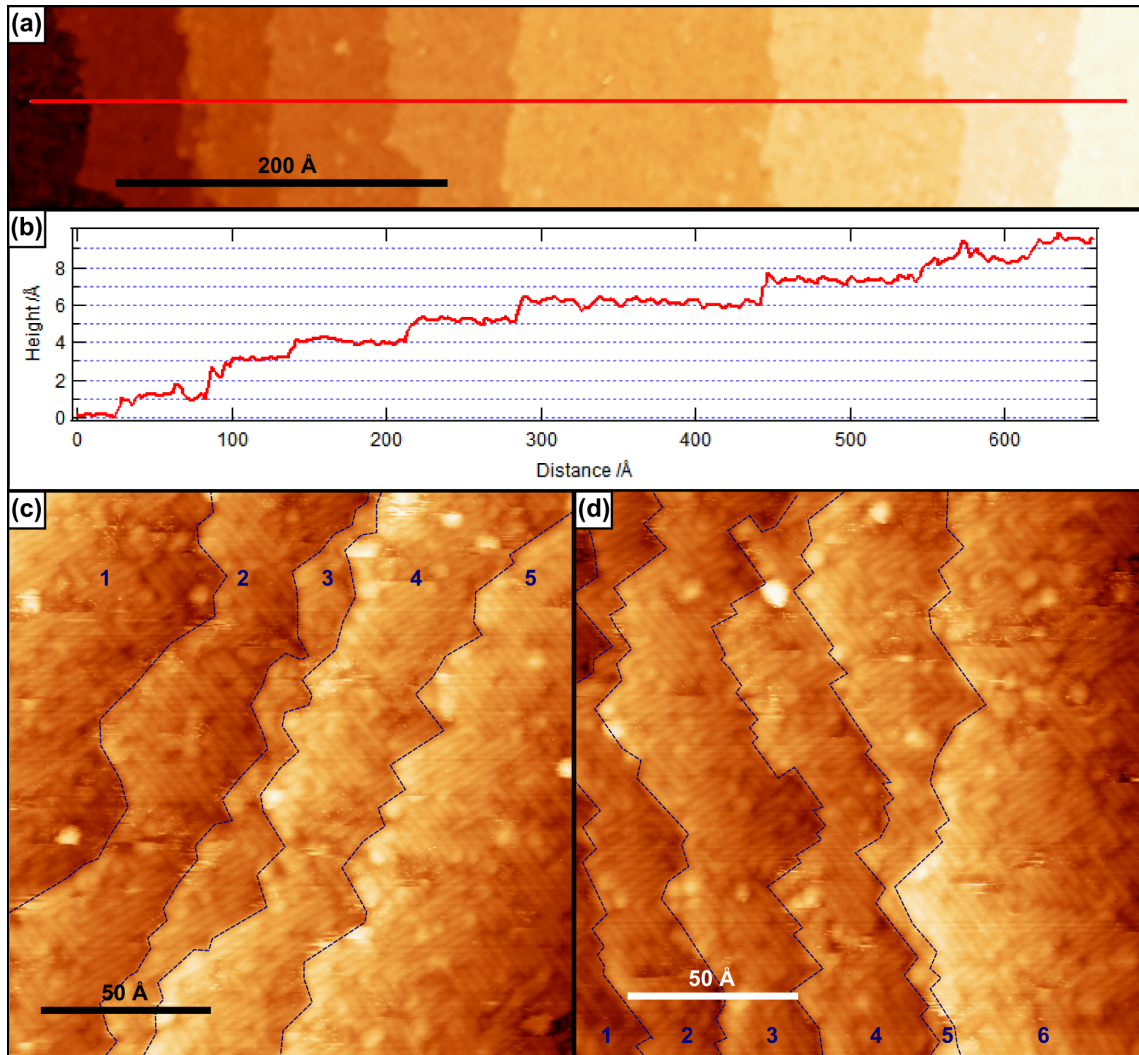
Figure 6.5: Terrace structure on the W(100)-(2 × 1)-O surface. (a) STM image showing the step like structure of the surface (image size 700 × 125 Å^2, $V_{sample} = 2$ V, $I_F = 200$ pA), (b) line profile showing the difference in height from step to step, which is ~ 1 Å, (c) and (d) STM images showing in closer detail the step edge structure; terraces are numbered in order of increasing height (image sizes 175 × 175 Å^2, $V_{sample} = 2$ V, $I_F = 200$ pA).
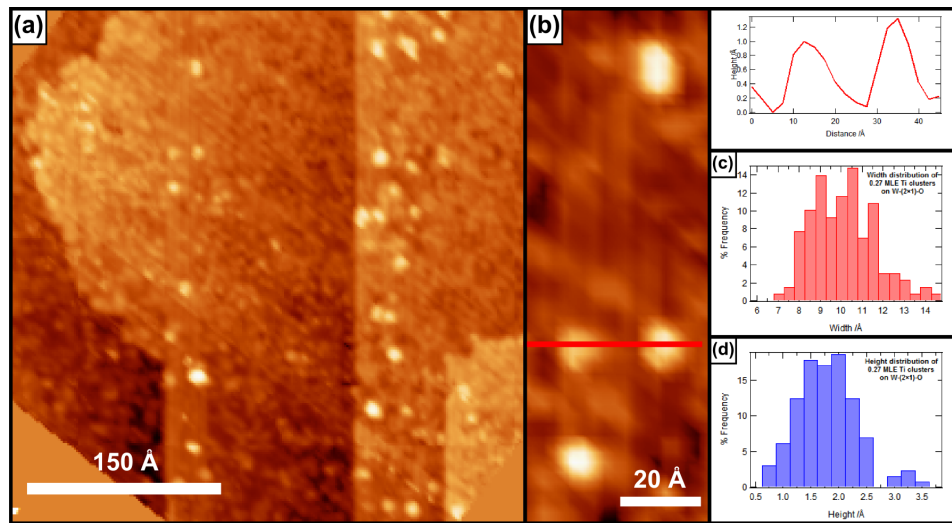
Figure 6.6: 0.27 MLE Ti deposited on a W(100)-(2 × 1)-O surface. (a) STM image showing Ti clusters on a stepped W(100)-(2 × 1)-O surface (image size 340 × 340 Å^2, V_{sample} = 1.5 V, I_F = 200 pA), (b) STM image showing Ti clusters on rows of W(100)-(2 × 1)-O (image size 50 × 100 Å^2, V_{sample} = 1.5 V, I_F = 200 pA), (c) distribution of cluster widths, (d) distribution of cluster heights (sample size of 128 clusters for both).

be terminated with rows running either parallel or perpendicular to the edge (figure 6.5(c) and (d)).

6.3.2   Deposition of Ti on the W(100)-(2 × 1)-O surface

0.27 MLE Ti (measured from AES) was deposited in UHV at room temperature onto a clean W(100)-(2 × 1)-O surface. Although STM offers no chemical specificity, by comparing images of pre- and post-Ti deposited surfaces it appears that Ti forms clusters on the W-(100)-(2 × 1)-O surface (figure 6.6(a)). Clusters appear to preferentially form centred over dark (topographically low) rows (figure 6.6(a)). These clusters have a mean diameter of 10 Å and a mean height of 1.8 Å (figure 6.6(c) and (d)).
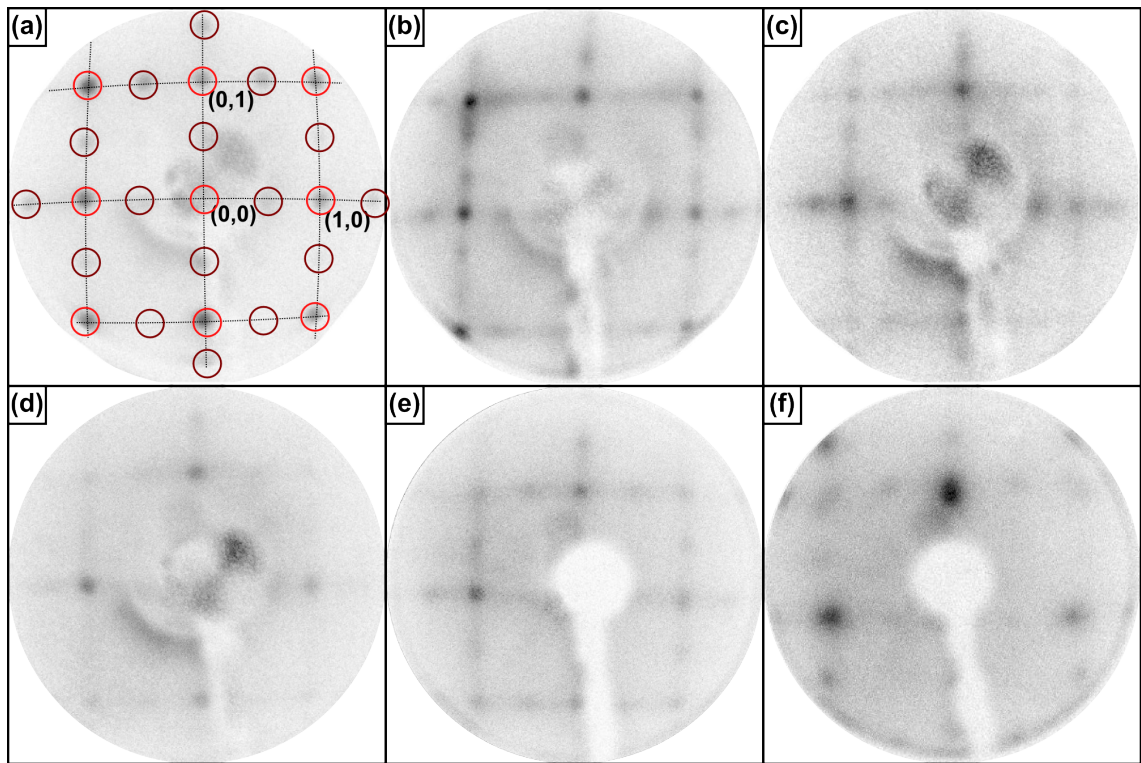
Figure 6.7: Series of LEED images for (a) a W-(2×1)-O surface, ($E_{beam} = 60$ eV), (b) 0.69 ($E_{beam} = 85$ eV), (c) 0.74, ($E_{beam} = 85$ eV), (d) 1.66, ($E_{beam} = 85$ eV), (e) 3.15, ($E_{beam} = 85$ eV), and (f) 4.04 MLE TiO$_2$ ($E_{beam} = 55$ eV).

6.3.3 Variation in TiO$_2$ thin films as a function of film thickness

Deposited Ti of varying thickness was oxidised by annealing in O$_2$ for 2 hr. The thickness of the TiO$_2$(110) thin films grown was estimated from the attenuation of the W $N_5O_3O_3$ peak following Ti deposition and annealing, using an established technique [26] (see appendix A).

0.69 MLE TiO$_2$ film

The LEED pattern produced from a 0.69 MLE TiO$_2$ film is shown in figure 6.7(b), with the LEED pattern for the bare W-(2×1)-O surface shown in figure 6.7(a). The
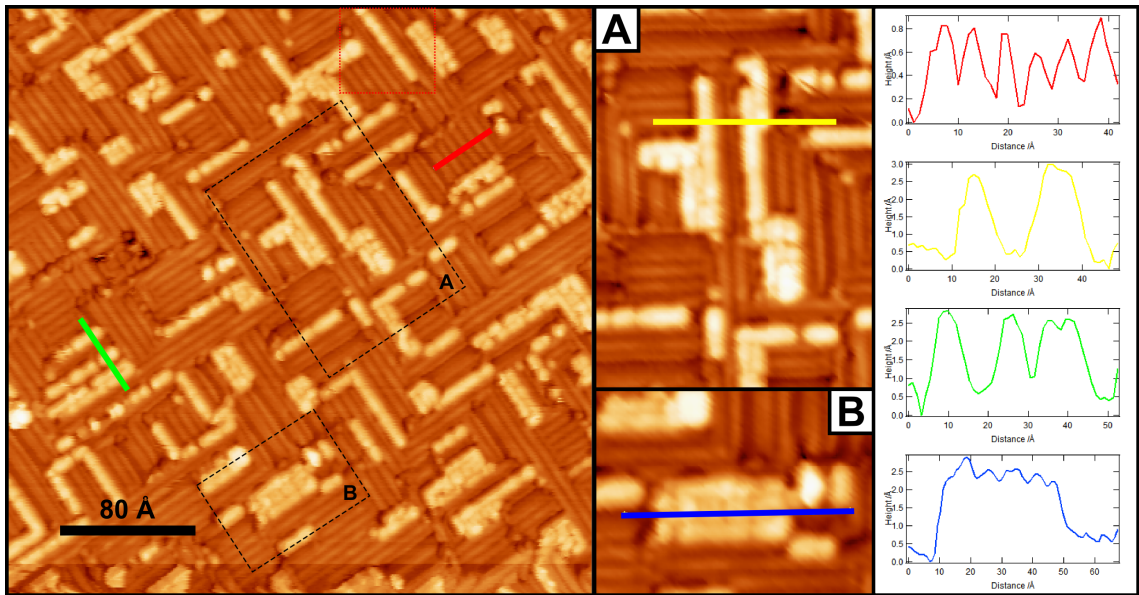
Figure 6.8: STM images showing a 0.69 MLE TiO$_2$ film on W-(2 × 1)-O. Image size 440 × 440 Å^2, V_{sample} = 2 V, I_F = 200 pA. Line profiles show row separation (red) and nanowire dimensions (yellow, green and blue).

(1 × 1) spots remain clear while spots along the axes are blurred.

Results from the previous chapter suggest a departure from stoichiometry for low coverages. As such, the features appearing in STM images will be considered as TiO$_x$. Due to the low coverage, STM (figure 6.8) shows large regions of uncovered W-(2 × 1)-O with a row separation of ~6.3 Å (red line profile), upon which TiO$_x$ "nanowires" appear - structures typically ~8 Å wide (yellow line profile, inset A) and up to ~ 100 Å in length. These nanowires are orientated along the two perpendicular axes of the W-(2×1)-O surface, and appear to lie along the dark rows of the substrate (most clearly illustrated by the region in figure 6.8 outlined in red). The dark rows of W-(2 × 1)-O are known to have a topographic origin [22]. In some places, TiO$_x$ "nanodots" and small islands form (inset B). Islands appear to be composed of two or more of the nanowire structures joined together. The blue line profile shows ridges separated by about 6.5 Å, however detailed structure could not be resolved. The island is ~ 2 Å high. The distribution of TiO$_x$ structures appears to be random, with no particular preference for step edges.
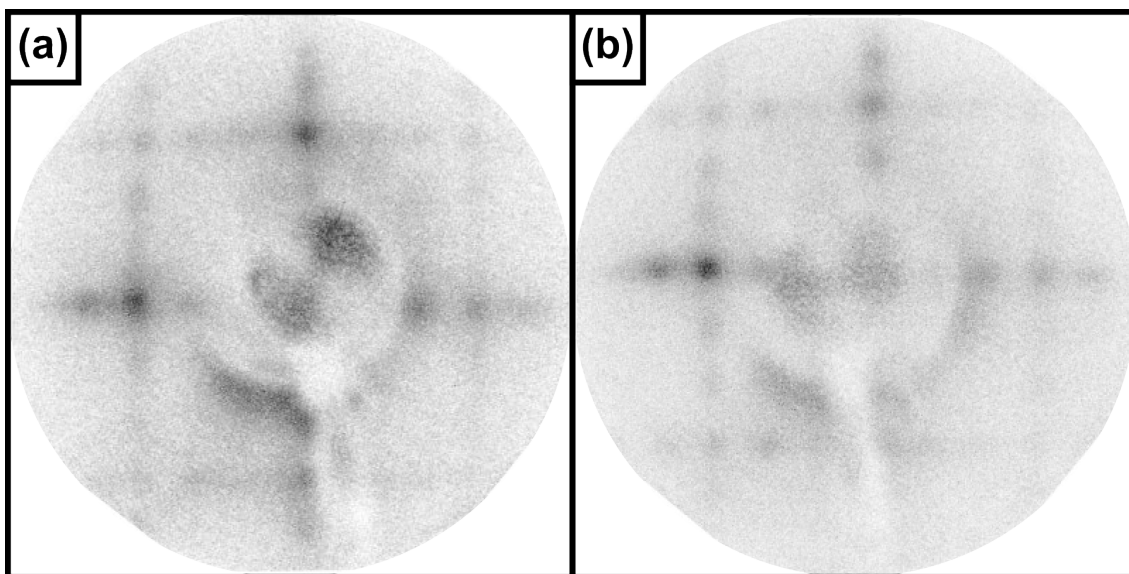
Figure 6.9: Comparison of LEED patterns for a (a) 0.74 MLE TiO$_2$ film (E_{beam} = 85 eV) and (b) the same film after 15 min UHV anneal at 875 K (E_{beam} = 85 eV).

0.74 MLE TiO$_2$ film

A small increase in thickness of the TiO$_2$ film results in a small loss of definition in the corresponding LEED pattern (figure 6.7(c); cf. (b)). Whilst the pattern is slightly more blurred, the same features are present: the blurred lines along the axes of the (2×1) pattern of the W-(2×1)-O surface.

Well resolved STM of this surface was not easily attained. The surface consists of small islands, presumably TiO$_x$ of around 12 Å in dimension (figure 6.10(a)). The surface appears to be quite well covered, although some structure indicative of the W-(2×1)-O substrate is still visible. Following an additional 10 min UHV anneal at 875 K and 5 min anneal in O$_2$ to 800 K, the LEED pattern appears similar with slightly less noise (figure 6.9(b)). There was no change in the intensity ratio of the Ti and W signals in AES, indicating no migration of Ti into the bulk substrate.

STM of the post-annealed surface shows the presence of small islands of TiO$_x$ (figure 6.10(b)), of up to around 30 Å in dimension (red line profile). There are very few
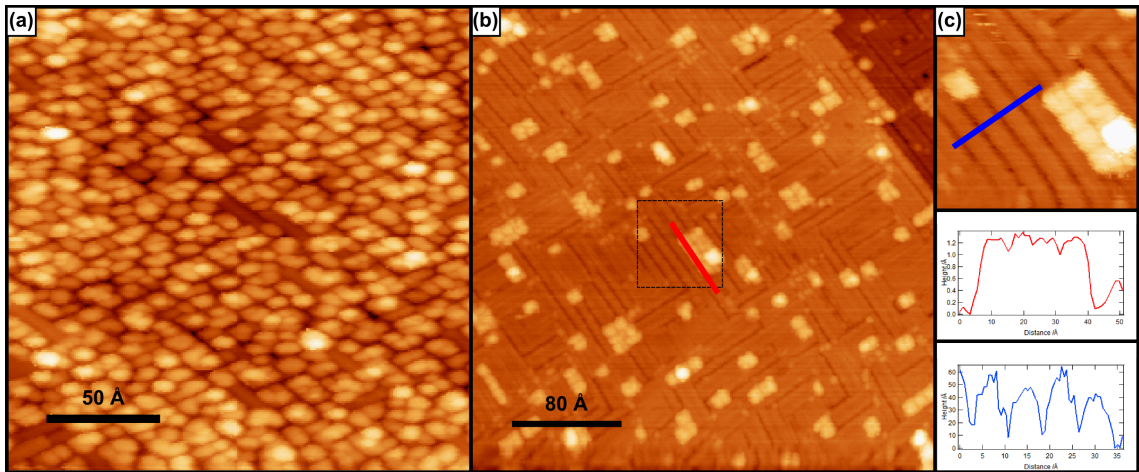
Figure 6.10: STM images showing a 0.74 MLE TiO$_2$ film on W-(2 $\times$ 1)-O. (a) The surface after annealing to 800 K in O$_2$ for 2 hr (image size 250 $\times$ 250 Å^2, $V_{sample} = 2$ V, $I_F = 200$ pA), (b) the surface following a 10 min UHV anneal at 875 K, followed by a 5 min O$_2$ anneal to 800 K (image size 350 $\times$ 350 Å^2, $V_{sample} = 2$ V, $I_F = 200$ pA), (c) an enlarged area of the same surface (image size 70$\times$ 70 Å^2, $V_{sample} = 2$ V, $I_F = 200$ pA.)

of the "nanowire" structures. The distribution of TiO$_x$ again shows no preference for step edges. Figure 6.10(c) shows an enlarged area. Island boundaries tend to coincide with the dark rows of the substrate. In this case however, the row separation of the substrate is around 9 Å (blue line profile), suggesting a further reconstruction of the surface to a (3 $\times$ 1) surface. This reconstruction is not observed across all of the substrate which may explain the faint LEED pattern.

1.66 MLE TiO$_2$ film

The LEED pattern for a 1.66 MLE TiO$_2$ film is shown in figure 6.7(d). The pattern is much fainter than the previous two thicknesses, although the same streaking along the axes is present. STM shows a rough surface consisting of small islands (figure 6.11(a)), around 13 Å in dimension, not unlike for the 0.74 MLE film.

A further 10 min UHV anneal to 875 K, followed by a 5 min O$_2$ anneal at 800 K resulted in the appearance of rectangular islands and very small nanodots (figure
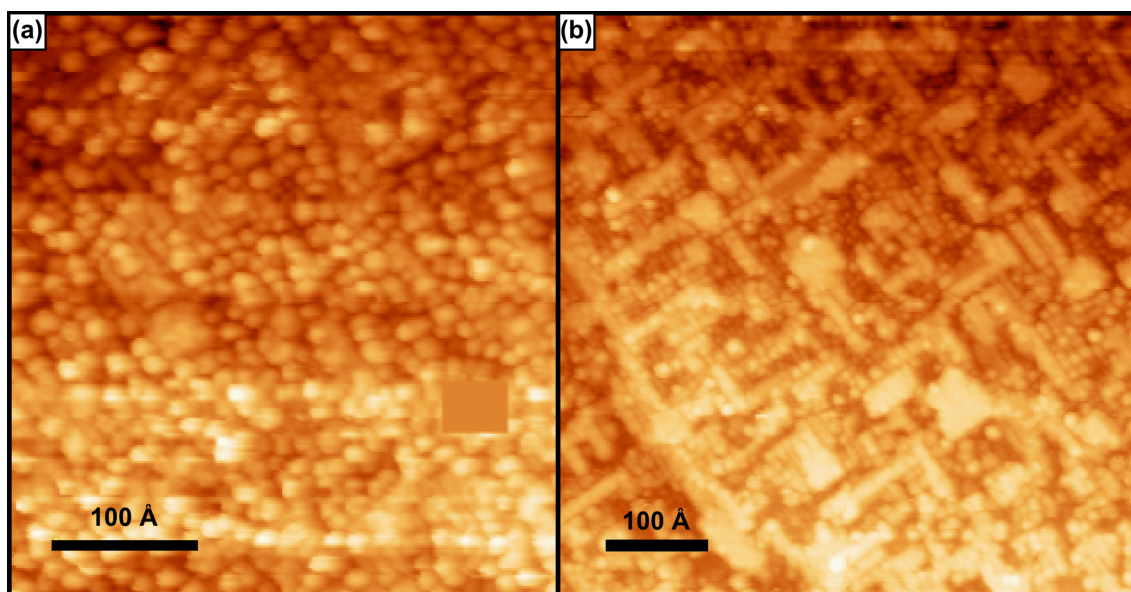
Figure 6.11: STM images of a 1.66 MLE thick TiO$_2$ film. (a) After a 2 hr anneal in O$_2$ at 800 K (image size 500 × 500 Å^2, V_{sample} = 1.5 V, I_F = 100 pA), (b) following a 10 min anneal to 875 K in UHV and 5 min O$_2$ anneal to 800 K (image size 600 × 600 Å^2, V_{sample} = 1.2 V, I_F = 100 pA).

6.11(b)). There is no structure visible that is related to the W-(2 × 1)-O surface, however the islands appear to be orientated along the two perpendicular axes of the substrate. More detailed structure could not be resolved. AES indicated no change in the Ti/W peak intensity ratio following the UHV anneal.

3.15 MLE TiO$_2$ film

The LEED pattern for a 3.15 MLE film is shown in figure 6.7(e). The pattern is slightly more defined than the previous images. There is still streaking along the axes but a little more clarity around the (2 × 1) spots. STM shows a very rough surface (6.12(a)). As such the resolution of images was severely limited. The orientation of features along the two axes of the substrate is just visible.

Following a 10 min UHV anneal at 875 K followed by a 5 min O$_2$ anneal at 800 K, the surface is markedly different (figure 6.12(b)). Large, smooth islands orientated
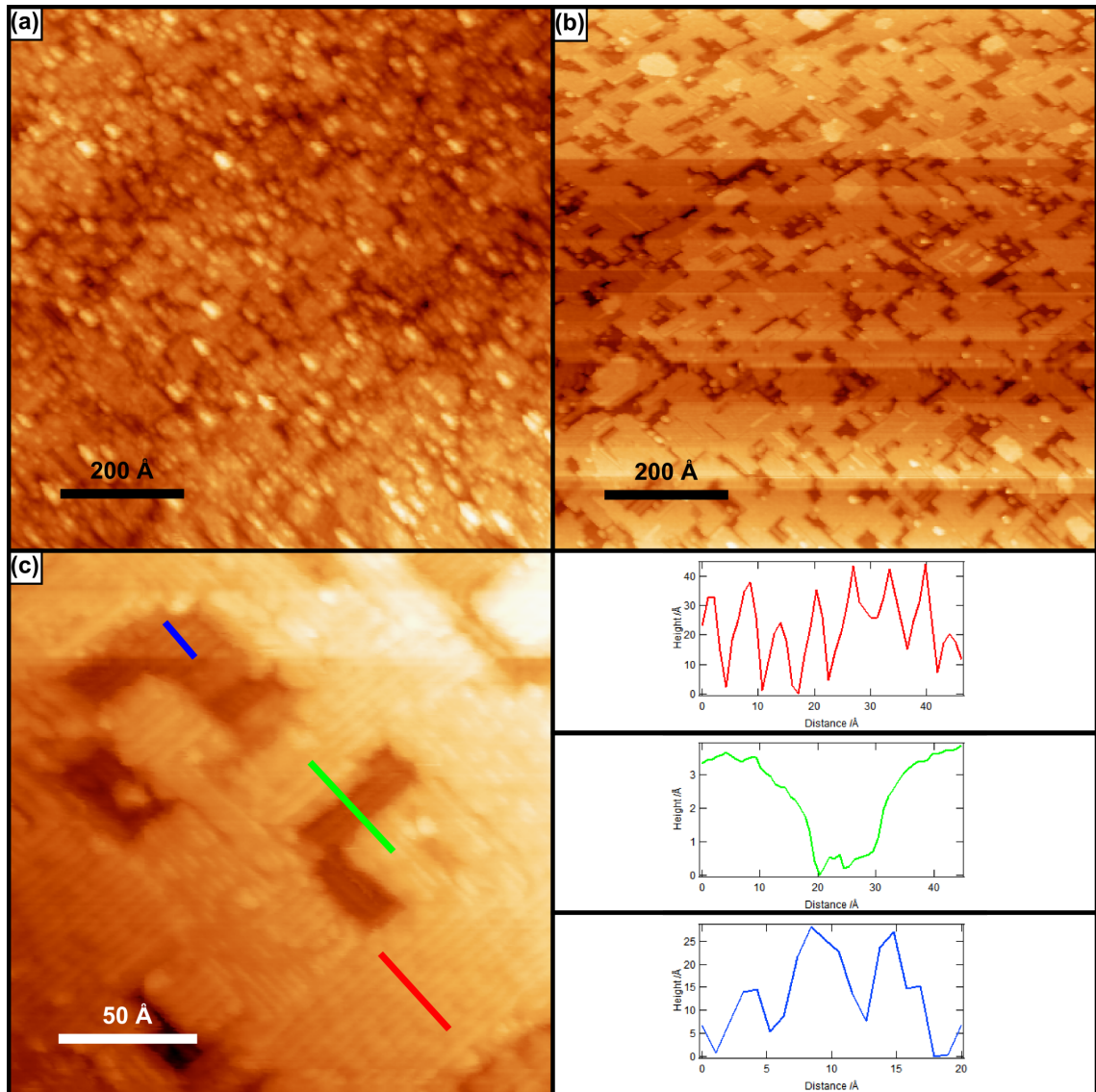
Figure 6.12: STM images showing a 3.15 MLE thick TiO$_2$ film. (a) After a 2 hr anneal to 800 K in O$_2$ (image size 1000 × 1000 Å^2, $V_{sample} = 1.5$ V, $I_F = 200$ pA), (b) following a 10 min UHV anneal to 875 K and 5 min O$_2$ anneal to 800 K (image size 1000 × 1000 Å^2, $V_{sample} = 0.5$ V, $I_F = 100$ pA), (c) at closer resolution, showing row structure and step edges (image size 200 × 200 Å^2, $V_{sample} = 0.7$ V, $I_F = 100$ pA).
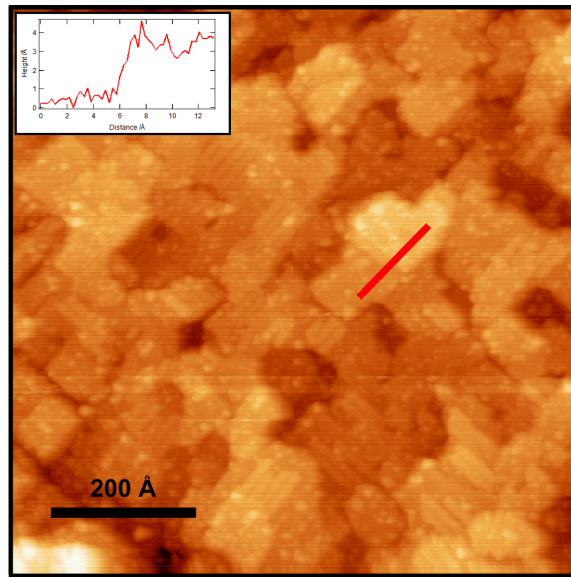
Figure 6.13: STM image showing the surface of a 4.04 MLE TiO$_2$ film (image size 800 × 800 Å^2, V_{sample} = 1.2 V, I_F = 50 pA).

along both the perpendicular axes of the substrate are visible. These islands have dimensions ranging from 20-150 Å. Figure 6.12(c) shows the row structure present on the surface in the two perpendicular orientations. The average row separation in both the top and second layers is comparable (red and blue line profiles), around 6.0 Å. Row separation was estimated by fitting line profiles with Gaussian curves and measuring the peak-to-peak distance. This similarity indicates none of the W-(2 × 1)-O substrate is visible. The step height is around 3.2 Å (green line profile).

4.04 MLE TiO$_2$ film

The LEED pattern for a 4.04 MLE TiO$_2$ film is shown in figure 6.7(f). The principal spots are slightly more vivid although the pattern is blurry. Figure 6.13 is an STM image showing that the surface consists of fairly large islands (up to 200 Å in size). The step height is around 3.2 Å. Row resolution could not be resolved on this surface.
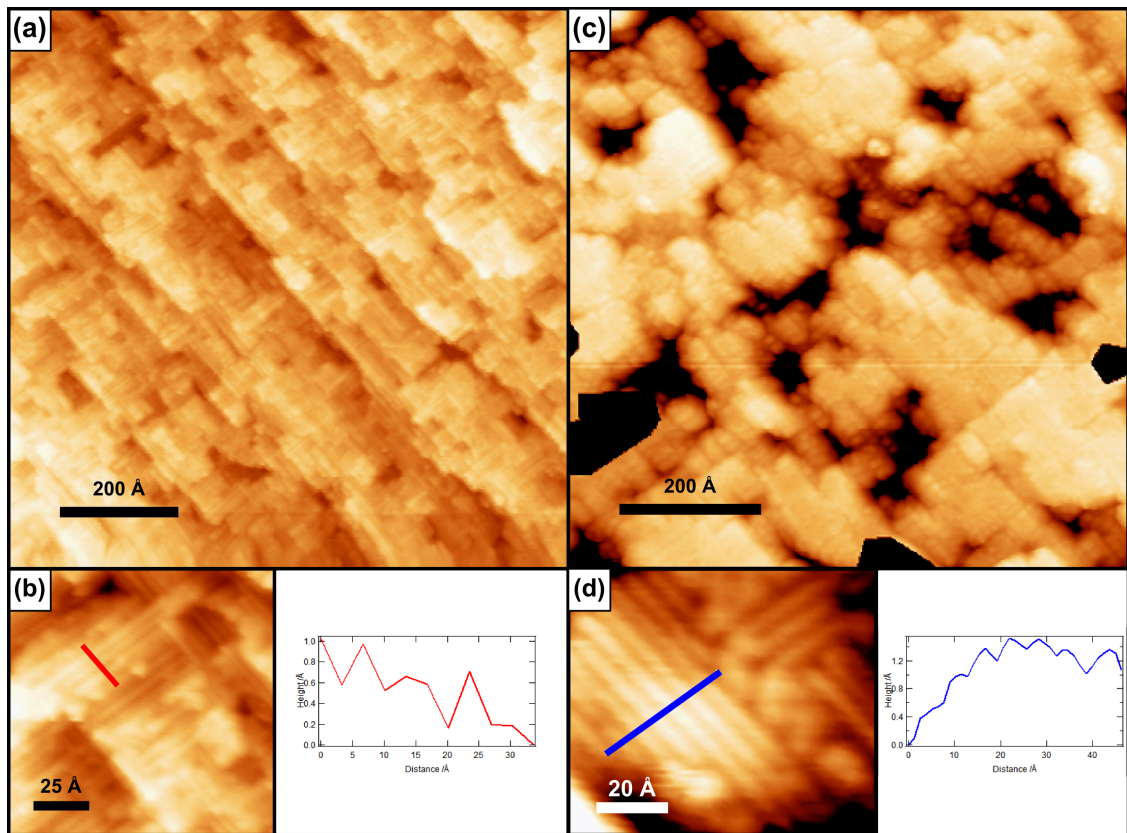
Figure 6.14: STM images of a 8.79 MLE TiO$_2$ film. (a) Surface of the film after oxidation (image size 1000 × 1000 Å^2, V_{sample} = 0.7 V, I_F = 200 pA), (b) a more detailed image of the same surface showing row structure (image size 120 × 120 Å^2, V_{sample} = 0.7 V, I_F = 200 pA), (c) the film after a 10 min UHV anneal to 875 K, followed by a 5 min O$_2$ anneal (image size 900 × 900 Å^2, V_{sample} = 1.5 V, I_F = 200 pA), (d) row structure of this surface (image size 90 × 80 Å^2, V_{sample} = 1.5 V, I_F = 200 pA).

8.79 MLE TiO$_2$ film

No discernible LEED pattern could be recorded from the surface of a 8.79 MLE thick TiO$_2$ film, even after an additional 15 min UHV anneal to 875 K followed by 5 min O$_2$ anneal to 800 K.

STM of the surface after the 2 hr O$_2$ anneal shows a very uneven surface consisting of islands in both perpendicular domains (figure 6.14(a)). Row structure is visible (figure 6.14(b), red line profile) showing rows separated by ~6.5 Å. The surface
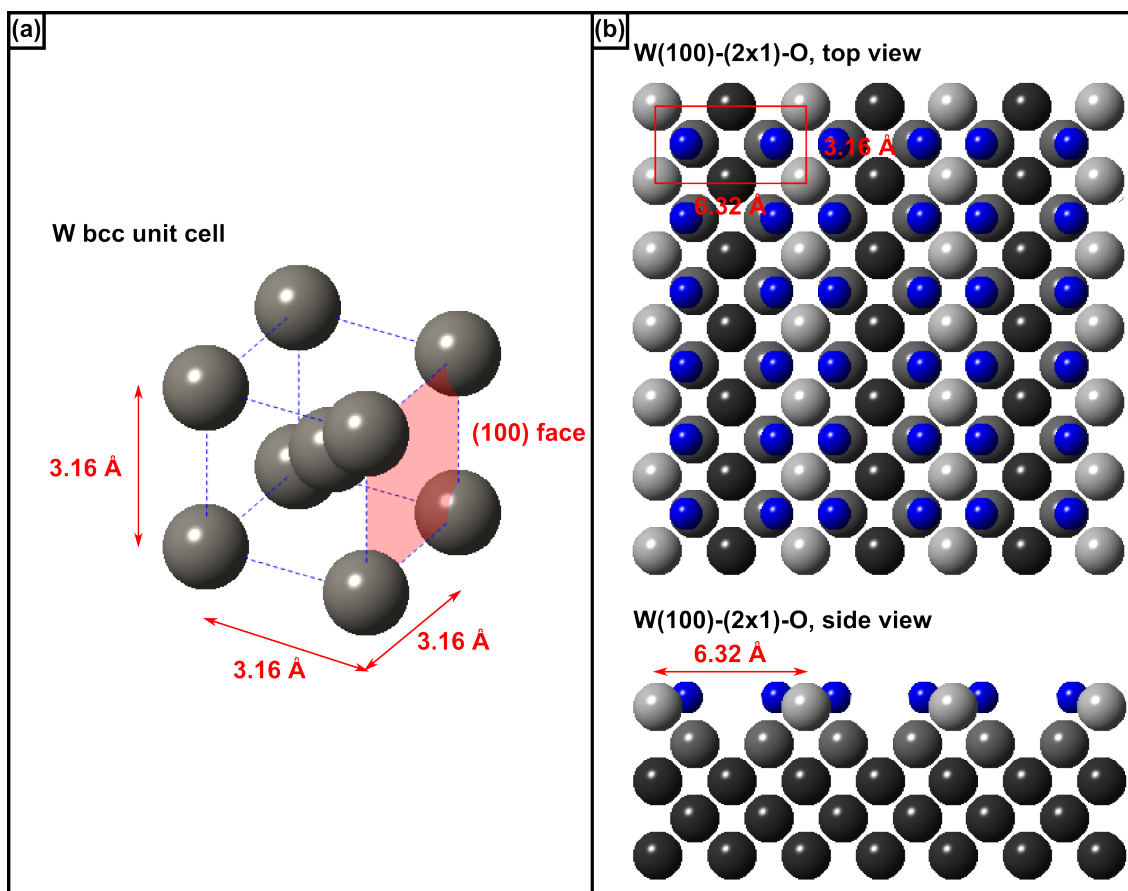
Figure 6.15: Models showing (a) the W body-centred cubic (bcc) unit cell with (100) face and (b) top and side views of the predicted ideal structure for the W(100)-(2×1)-O reconstruction, O atoms are blue; top level W atoms are shaded light grey, second level W atoms in grey and deeper W atoms in dark grey.

was annealed in UHV at 875 K for 15 min followed by 5 min O₂ anneal to 800 K. This treatment resulted in a slightly less uneven surface with larger domains (figure 6.14(c)). Again, row structure can be discerned and is shown in figure 6.14(d) (blue line profile), with an average row separation of 6.57 Å.

6.4 Discussion

6.4.1 The W(100)-(2×1)-O reconstructed surface

The W body-centred cubic (bcc) unit cell (a=3.16 Å) is shown in figure 6.15(a), with the (100) plane marked. The observed contrast of bright and dark rows in STM of TiO$_2$(110) has been shown to be due to topography rather than electronic effects [22]. Figure 6.15(b) shows the predicted ideal structure from a combination of LEED and low-energy ion scattering experiments of the W(100)-(2×1)-O reconstruction [20, 21, 27, 28].

STM of the W(100)-(2×1)-O reconstruction (figure 6.4) shows domains of rows, with a periodicity of 6.3 Å, similar to previous results [22]. Based on the predicted model for the (2×1) reconstruction [20], this separation marks the distance between missing rows (figure 6.15), and accounts for the (2×1) spots in LEED. The surface was observed to be smooth with large, flat terraces consisting of regions of both perpendicular domains, which accounts for the sharp (2×1) LEED pattern observed in figure 6.3(b). The resolution of STM images shown here is improved compared with images of the same surface reported in the literature [22].

6.4.2 W(100)-(2×1)-O/TiO$_2$(110) films

Ti on W(100)-(2×1)-O

At a low deposition level of Ti on W(100)-(2×1)-O, the Ti appears to cover the substrate surface fairly evenly. The tallest clusters appear within $\sim$50 Å of step edges. XPS results presented in chapter 5 suggest Ti deposited onto an oxidised W surface is largely metallic, with some broadening to Ti 2p peaks caused by reduced states. The presence of reduced states suggests some interaction between the Ti and

O on the substrate surface.

Following oxidation of sub-monolayer levels of Ti on W(100)-(2 × 1)-O, there is a high TiO_x island density, which indicates the mobility of the Ti atoms on the oxygen reconstructed surface is low.

Development of LEED pattern

The substrate preparation described in section 6.3.1 produced a sharp (2 × 1) LEED pattern indicating a (2 × 1) reconstruction of the surface. This demonstrates that it is possible to not completely remove all O from the W(100) substrate yet achieve a well-ordered starting substrate surface with close epitaxial match to TiO_2(110) films. As previously reported [18], the LEED pattern of films <5 MLE thickness is complicated due pinholes in the film, incomplete coverage of the substrate or competitive oxidation of the W substrate. Certainly in the case of the latter, some areas of further reconstructed W surfaces were observed in STM. LEED patterns for films <5 MLE presented here are faint and not particularly sharp indicating a large number of different domains and little long range order.

Thickness effects

Qualitatively, it can be observed that the morphology of films varies with thickness. In order to gauge this change quantitatively, the average number of domains per square nanometre was estimated from a minimum of three different 1000 × 1000 Å² STM images for each film. Here, a domain was considered to be an area on a level plane with rows in only one direction. The variation between film roughness and thickness is shown in figure 6.16(a). The trend shows the number of domains per nanometre square decreases with increasing film thickness. This is likely due to the reduction in strain, felt more strongly near the substrate/overlayer interface, and
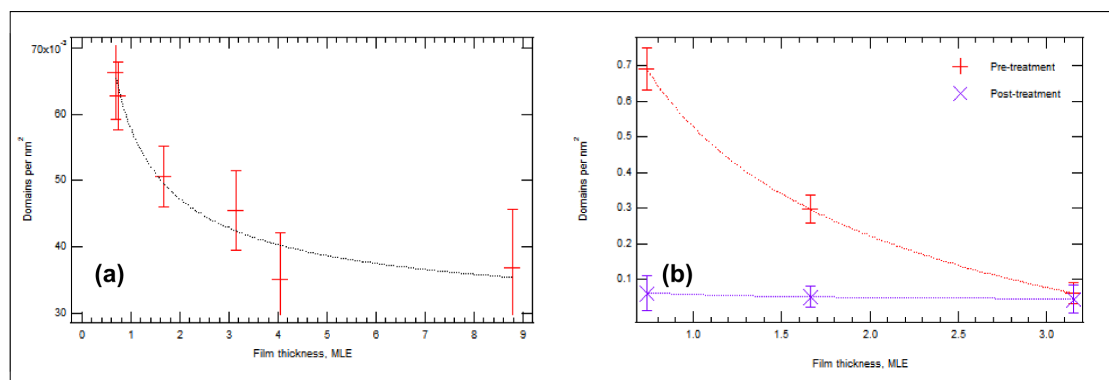
Figure 6.16: (a) Graph showing the variation in film roughness (as estimated from the number of domains per nm²) with film thickness. (b) Graph showing the change in domain density with a 15 min UHV anneal.

the development of more "bulk-like" structure.

The effect of post oxidation UHV annealing of three films for which data was available is shown in figure 6.16(b). In each case there is a reduction in the domain density per square nanometre, with bigger reductions for thinner films. This points to a decreasing mobility of ions with increasing thickness.

6.4.3 TiO₂(110) thin film surface features

The TiO₂(110) row structure can be discerned by STM for thicker films (figure 6.17). Whilst resolution of rows is good, it was not possible to clearly discern defect features such as O_{vac} sites. Density of these sites decreases with film thickness (chapter 5), and thus only a low concentration would be expected for the 8.79 MLE film. This film (the thickest presented) gave the best resolution images, however no defects were observed between rows. Conversely, resolution is poorer for thinner films where the expected defect concentration would be higher. Additionally, reduced Ti states observed by XPS could arise from step edge atoms or interfacial sites.

Comparing row separation in the 3.15 MLE and 8.79 MLE films, there is a contraction in the thinner film (figure 6.18). Row separation was accurately measured by
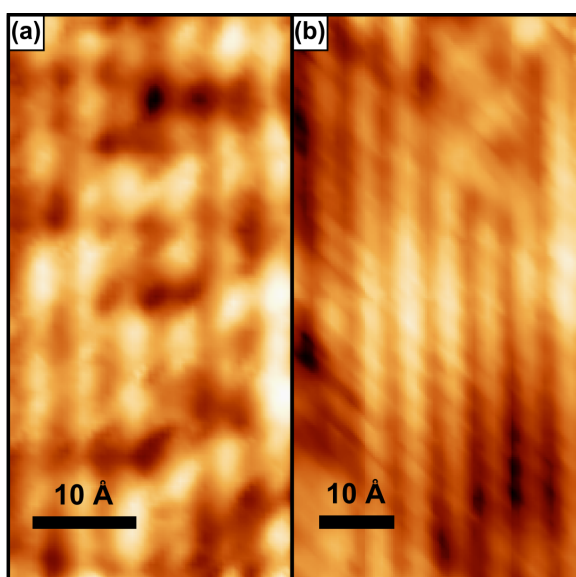
Figure 6.17: STM images showing $TiO_2(110)$ row structure of (a) a 3.15 MLE film (image size 60×30 Å², $V_{sample} = 0.7$ V, $I_F = 100$ pA), (b) a 8.79 MLE film (image size 90×45 Å², $V_{sample} = 0.7$ V, $I_F = 100$ pA).
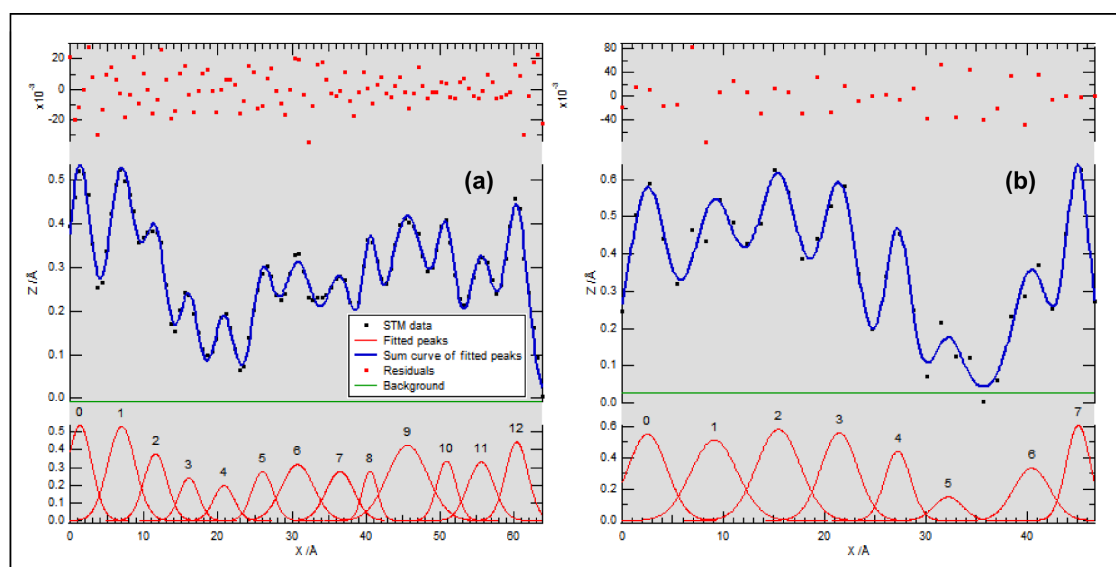
Figure 6.18: Cross section line profiles showing row corrugation and peak fitting to estimate average row separation for TiO_2 films of thickness (a) 3.15 MLE and (b) 8.79 MLE.

fitting rows with Gaussian curves and measuring the peak-to-peak difference. This contraction of the surface unit cell has been previously reported for films on Ni(110) substrates [11], and demonstrates the shift towards more bulk-like TiO$_2$ structure in thicker films.

6.5   Conclusions

Six TiO$_2$(110) ultrathin films between 0.5-9 MLE have been grown on a reconstructed surface of W(100)-(2 × 1)-O and characterised by LEED, AES and STM. Roughness of films, as gauged by the number of different domains per unit area, can be improved by annealing in UHV and the final roughness decreases with increasing thickness. TiO$_2$(110) row structure has been resolved although no defect features were observed. STM of low coverage Ti on W(100)-(2 × 1)-O shows Ti forms as small clusters and on oxidation forms linear, "nanowire" structures. These structures align with the rows of the underlying substrate.

A low-temperature method for preparing ultrathin TiO$_2$(110) films on W(100) has been presented, allowing growth using instruments with high temperature restrictions. The STM images presented here are the first *in situ* images of TiO$_2$(110) thin films on W(100). The ability to clearly resolve rows as shown for thicker films here is vital for imaging of adsorption of molecules (for example, of water or oxygen), which could lead to a greater understanding of surface processes on TiO$_2$. Whilst not perfect mimics of bulk surfaces, ultrathin films represent adequate analogues for the study of surface properties, particularly of otherwise insulating materials.

References

[1] Bonnell, D.A.; *Prog. Surf. Sci.*, **1998**, *57*, 187

[2] Rohrer, G.S., Henrich, V., Bonnell, D.A.; *Science*, **1991**, *250*, 1239

[3] Rohrer, G.S., Henrich, V., Bonnell, D.A.; *Surf. Sci.*, **1992**, *274*, 35

[4] Novak, D., Garfunkel, E., Gustafsson, T.; *Phys. Rev. B*, **1994**, *50*, 5000

[5] Fischer, S., Munz, A., Schierbaum, K-D., Göpel, W.; *Surf. Sci.*, **1995**, *337*, 17

[6] Diebold, U., Andersen, J.F., Ng, K.O., Vanderbielt, D.; *Phys. Rev. Lett.*, **1996**, *77*, 1322

[7] Diebold, U.; *Surf. Sci. Rep.*, **2003**, *48*, 53

[8] Nilius, N.; *Surf. Sci. Rep.*, **2009**, *64*, 595

[9] Oh, W.S., Xu, C., Kim, D.Y., Goodman, D.W.; *J. Vac. Sci. Technol. A*, **1997**, *15(3)*, 1710

[10] Chen, M.S., Wallace, W.T., Kumar, D., Yan, Z., Gath, K.K., Cai, Y., Kuroda, Y., Goodman, D.W.; *Surf. Sci. Lett.*, **2005**, *581*, L115

[11] Ashworth, T.V., Thornton, G.; *Thin Solid Films*, **2001**, *400*, 43

[12] Ashworth, T.V., Muryn, C.A., Thornton, G.; *Nanotechnology*, **2005**, *16*, 3041

[13] Papageorgiou, A.C., Cabailh, G., Chen, Q., Resta, A., Lundgren, E., Andersen, J.N., Thornton, G.; *J. Phys. Chem. C*, **2007**, *111*, 7704

[14] Männig, A., Zhao, Z., Rosenthal, D., Christmann, K., Hoster, H., Rauscher, H., Behm, R.J.; *Surf. Sci.*, **2005**, *576*, 29

[15] Sedona, F., Llabrés i Xamena, F.X., Rizzi, G.A., Granozzi, G., Ostermann, D., Schierbaum, K.D.; *J. Phys. Chem. B*, **2005**, *109(51)*, 24411

[16] Finetti, P., Caffio, M., Cortigiani, B., Atrei, A., Rovida, G.; *Surf. Sci.*, **2008**, *602*, 1101

[17] Bennett, R.A., McCavish, N.D.; *Topics in Catalysis*, **2005**, *36*, 11

[18] McCavish, N.D., Bennett, R.A.; *Surf. Sci.*, **2003**, *546*, 47

[19] Bennett, R.A., Mulley, J.S., Newton, M.A., Surman, M.; *J. Chem. Phys.*, **2007**, *127*, 084707

[20] Yamazaki, H., Kamisawa, T., Kokubun, T., Haga, T., Kamimizu, S., Sakamoto K.; *Surf. Sci.*, **2001**, *477*, 174

[21] Bauer, E., Poppa, H., Viswanth, Y.; *Surf. Sci.*, **1976**, *58*, 517

[22] Meyer, J.A., Kuk, Y., Estrup, P.J., Silverman, P.J.; *Phys. Rev. B*, **1991**, *41*, 9104

[23] Grunze, M., Ruppender, H, Elshazly, O.; *J. Vac. Sci. Technol. A*, **1988**, *6(3)*, 1266

[24] Larkins, F.P.; *Atomic and Nuclear Data Tables*, **1977**, *20*, 311

[25] Horcas, I., Fernandez, R., Gomez-Rodriguez, J.M., Colchero, J., Gomez-Herrero J., Baro, A. M.; *Rev. Sci. Instrum.*, **2007**, *78*, 013705

[26] Briggs, D., Seah, M.P., Eds.; *Practical Surface Analysis by Auger and X-ray Photoelectron Spectroscopy*, **1983**, John Wiley & Sons Ltd.

[27] Altman, M.S., Bauer, E.; *Surf. Sci.*, **1996**, *347*, 265

[28] Yamazaki, H., Kamimizu, S., Hara, K., Sakamoto, K.; *Surf. Sci. Lett.*, **2003**, *558*, L505

Chapter 7

Conclusions

Ultrathin films of metal oxides have been used as model systems for surface science studies in the context of catalysis. The chemistry and physical structure of films have been probed using photoemission spectroscopy (PES) and scanning tunnelling microscopy (STM). Results show that thin films exhibit comparative behaviour to bulk counterparts and could provide a better understanding of single crystal surfaces.

The interaction between Pd and ceria was examined by X-ray photoelectron spectroscopy (XPS) and resonance photoemission spectroscopy (RESPES) using CeO_{2-x} thin films grown on Pt(111). Evidence to support theoretical calculations of a model of charge transfer from Pd to ceria was found using the % Ce^{3+} (calculated from both techniques) as a measure of reduction.

Understanding the role of ceria, its oxygen storage capacity (OSC) and interaction with precious metal additives is crucial to the enhancement of three-way catalysts (TWCs) used to control automobile emissions. To further the spectroscopic information reported in this thesis, the next step is to provide topographic information regarding the nature of metal additives and defect states in the ceria surface. Atomic

force microscopy (AFM) and STM would be ideal imaging tools to study these aspects. Recently, STM of ceria films grown on Pt(111) and details of defect structure have been reported[*]. The next step is to provide a more comprehensive view of the nature of metal nanoparticles on ceria surfaces. This could be achieved by using STM to map electronic distribution around Pd nanoparticles on the ceria surface.

TiO_2 ultrathin films were grown on W(100), and the physical structure and reactivity of them were investigated by low-energy electron diffraction (LEED), XPS and STM.

XPS results show that films are non-stoichiometric. Due to lessening substrate interactions, thicker films have less non-stoichiometry - films around 1 MLE thick have around 5% Ti^{3+} states whilst films thicker than 5 MLE have 1% Ti^{3+}. Films are shown to be reactive with both H_2O and O_2. The analysis of the O $1s$ spectrum showed two satellite peaks additional to the main O $1s$ peak arising from O in the bulk. These satellite peaks were identified as arising from bridging hydroxyl groups and molecular water adsorbed to exposed W(100).

STM was used to examine the physical structure of TiO_2(110) films grown on W-(2×1)-O and how properties are affected by increasing film thickness. Thicker films were found to be smoother, with larger domains. It was also found that annealing films could further improve surface smoothness. The STM images presented are the first detailed *in situ* images of TiO_2(110) grown on W(100). Row structure can be discerned although no surface defects were observed. However, these results offer a promising platform from which the adsorption of H_2O and O_2 on TiO_2 can be imaged using thin films. A suggested experiment would be to use STM on TiO_2 films grown in accordance to the method in chapter 6 to grow films of medium thickness (3-5 MLE), dose incremental amounts of H_2O and O_2 and monitor each stage with STM. A particularly interesting experiment, although one requiring sophisticated use of

---

[*]Grinter, D.C., Ithnin, R., Pang, C.L., Thornton, G.; *J. Phys. Chem. C*, **2010**, *114*, 17036

the STM would be to dose adsorbates *in situ* whilst scanning.

TiO_2 is a widely studied material, and particularly the defect structure is of great interest due to its importance with respect to the surface chemistry. Using thin films of TiO_2 grown on W(100) has been shown to be a suitable system for study using surface science probes. The STM work described in this thesis could be expanded to provide a clearer picture of the structure and reactivity of defects. An important consideration in the selection of W(100) as a substrate is that it is a paramagnet. Thus $W(100)/TiO_2(110)$ thin films - and specifically defect structure - could be studied using electron paramagnetic resonance (EPR), providing a definitive EPR signature of defects for subsequent use in the study of powdered samples.

Appendix A

Calculating thin film thicknesses

In this appendix, the methods used to estimate thin film thicknesses from XPS and AES are discussed.

A.1 Estimating thin-film thickness from XPS

To a first approximation, the intensity of XPS peaks is proportional to the surface concentration of a specific chemical species and the photoionisation cross-section. Electrons travelling through a solid are attenuated exponentially, and therefore the further an electron must travel through a solid, the lower the chance of it being detected [1–3].

Two-phase systems   Two phase systems (figure A.1(a)) arise from an overlayer material, O adsorbed on a substrate, S. The attenuation of electrons from the substrate is a function of overlayer thickness, d_O, atomic cross-section, σ, and the inelastic mean free path (IMFP), λ, such that:
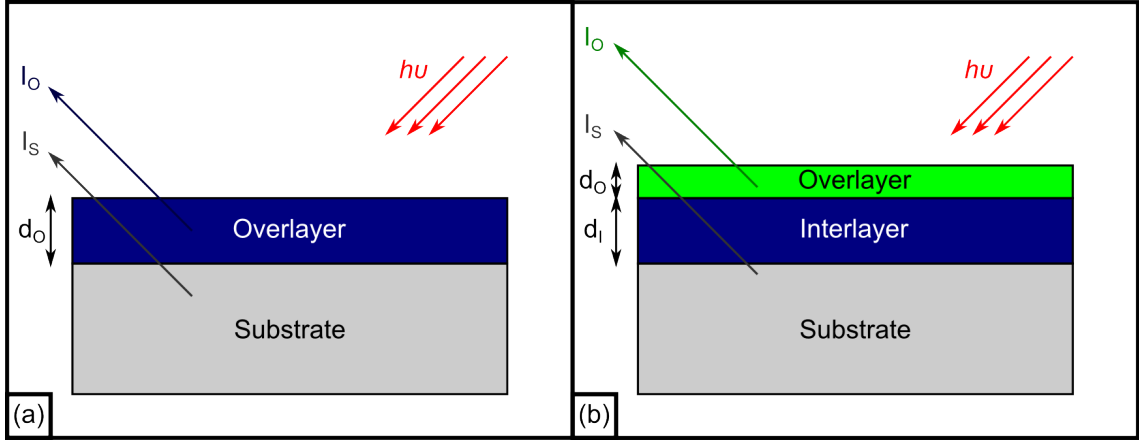
Figure A.1: Schematic diagrams of (a) a two-phase system, (b) a three-phase system.

$$I_S = E_{K(S)}^{-x} \cdot \sigma_S \cdot \lambda_S \cdot \exp^{\left(\frac{-d_O}{\lambda_S}\right)} \cdot \exp^{\left(\frac{-d_O}{\lambda_{S/O}}\right)} \tag{A.1}$$

where $E_{K(S)}$ is the kinetic energy of an electron from the substrate detected, λ_S is the IMFP of an emitted substrate electron in the substrate material S for a kinetic energy $E_{K(S)}$, and $\lambda_{S/O}$ the IMFP of a substrate electon in the overlayer material, O. The kinetic energy terms, E_K arise due to the transmission function of the analyser [4]. The power in this term, x is specific to the energy analyser used.

Similarly, an expression can be written for the intensity of an overlayer, O peak:

$$I_O = E_{k(O)}^{-x} \cdot \sigma_O \cdot \lambda_O \cdot \left(1 - \exp^{\left(\frac{-d_O}{\lambda_O}\right)}\right) \tag{A.2}$$

Dividing equation A.2 by equation A.1 and rearranging gives an expression in terms of the intensity ratio, I_O/I_S:

$$\frac{E_{k(S)}^{-x}}{E_{k(O)}^{-x}} \cdot \frac{I_O}{I_S} \cdot \frac{\sigma_S}{\sigma_O} \cdot \frac{\lambda_S}{\lambda_O} \cdot \exp^{\left(\frac{-d_O}{\lambda_S}\right)} \cdot \exp^{\left(\frac{-d_O}{\lambda_{S/O}}\right)} + \exp^{\left(\frac{-d_O}{\lambda_O}\right)} -1 = 0 \tag{A.3}$$

The intensity ratio, I_O/I_S can be determined experimentally from prominent XPS peaks, and equation A.3 can be solved for the thickness of the overlayer, d_O.

Three-phase systems In a three-phase system (figure A.1(b)), an intermediate interlayer phase, I, of known thickness d_I lies between the substrate, S and the overlayer, O'. This complicates the procedure as now there is attenuation due to both the intermediate layer, I and the overlayer, C. This is accounted for by adding an extra term to equation A.1:

$$I_S = E_{k(S)}^{-x} \cdot \sigma_S \cdot \lambda_S \cdot \exp^{\left(\frac{-d_{O'}+d_I}{\lambda_S}\right)} \cdot \exp^{\left(\frac{-d_I}{\lambda_{S/I}}\right)} \cdot \exp^{\left(\frac{-d_{O'}}{\lambda_{S/O'}}\right)} \tag{A.4}$$

where $\lambda_{S/O'}$ is the IMFP of an emitted substrate electron in the overlayer, O' with a kinetic energy $E_{k(S)}$. The equation for the intensity of overlayer peak, $I_{O'}$ is similar to equation A.2:

$$I_{O'} = E_{k(O')}^{-x} \cdot \sigma_{O'} \cdot \lambda_{O'} \cdot \left(1 - \exp^{\left(\frac{-d_{O'}}{\lambda_{O'}}\right)}\right) \tag{A.5}$$

Dividing equation A.5 by equation A.4, and rearranging gives:

$$\frac{E_{k(S)}^{-x}}{E_{k(O')}^{-x}} \cdot \frac{I_{O'}}{I_S} \cdot \frac{\sigma_S}{\sigma_{O'}} \cdot \frac{\lambda_S}{\lambda_{O'}} \cdot \exp^{\left(\frac{-d_{O'}+d_I}{\lambda_S}\right)} \cdot \exp^{\left(\frac{-d_I}{\lambda_{S/I}}\right)} \cdot \exp^{\left(\frac{-d_{O'}}{\lambda_{O'}}\right)} + \exp^{\left(\frac{-d_I}{\lambda_I}\right)} - 1 = 0 \tag{A.6}$$

$I_{O'}/I_S$ can be determined experimentally from XPS spectra, and equation A.6 can be solved for $d_{O'}$.

A.2 Estimating thin-film thickness from AES

Overlayer thickness can be quantified from AES by monitoring the change in intensity of a substrate peak before, I_S^∞ and after, I_S overlayer material has been added.

These values are related via a form of the Beer-Lambert law [1]:

$$I_S = I_S^\infty \exp(\frac{-d_O}{\lambda_O})$$

(A.7)

where d_O is the overlayer thickness and λ_O is the IMFP of an electron from the overlayer. When I_S^∞ and I_S have been determined experimentally, equation A.7 can be rearranged in terms of d:

$$d = \lambda_O \ln \frac{I_S^\infty}{I_S}$$

(A.8)

References

[1] Briggs, D., Seah, M.P., Eds.; *Practical Surface Analysis by Auger and X-ray Photoelectron Spectroscopy*, **1983**, John Wiley & Sons Ltd.

[2] Dreiling, M.J.; *Surf. Sci.*, **1978**, *71*, 231

[3] `http://www.specs.de/cms/front_content.php?idart=417&idcat=231&fid=1339`, "TNote-OverlayerThickness.pdf", Retrieved February 2010.

[4] Cross, Y.M., Castle, J.E.; *J. Elect. Spectr. Rel. Phenom.*, **1981**, *22*, 53